

COMPUTATIONAL STUDIES OF COMPLEX
SYSTEMS IN CONDENSED
MATTER PHYSICS

By

MICHAEL MOHR CLARK

Bachelor of Arts

Hendrix College

Conway, Arkansas

1990

Submitted to the Faculty of the
Graduate College of the
Oklahoma State University
in partial fulfillment of
the requirements for
the Degree of
DOCTOR OF PHILOSOPHY
December, 1996

COPYRIGHT

By

Michael Mohr Clark

December, 1996

COMPUTATIONAL STUDIES OF COMPLEX
SYSTEMS IN CONDENSED
MATTER PHYSICS

Thesis Approved:

Avy I Salt

Thesis Advisor

Paul W. Leisner

Benjamin Taylor

William Hanna

Thomas C. Collins

Dean of the Graduate College

ACKNOWLEDGMENTS

The completion of a Ph.D. thesis is a personal endeavor. However, it requires a community of instruction, mentorship and support. This thesis is no exception, and I would now like to recognize people who have especially contributed to this work.

First of all, thanks go to Dr. Larry Scott, my thesis advisor. His broad research interests afforded me the opportunity to perform the studies that are reported in this thesis; his guidance and encouragement ensured that the opportunity was realized. Thanks are also due to the rest of my thesis committee: Dr. Penger Tong, Dr. Paul Westhaus, and Dr. Jim Harmon. Dr. Westhaus deserves particular recognition. The excellence of his courses is unmatched as is his devotion to the department and its students.

The first part of the thesis was made possible by the collaboration with Dr. Eric Jakobsson at the University of Illinois, Urbana-Champaign. He generously provided computational facilities and insight into biomembrane physics (and even room and board for two extended visits to Urbana-Champaign). Similarly, the second part of the thesis was made possible with the expertise of Dr. Lionel Raff of the Department of Chemistry. Funding for the research contained in the second part of the thesis was given by the National Science Foundation (Grant No. DMR-9321139). Expert advice regarding programming, unix system administration, and kids was provided by Terry Klarich, formerly with Computer and Information Services.

No less important than academic mentorship is the support of family and friends. Several current and former graduate students have toiled beside me in the trenches of graduate study. Their camaraderie has provided invaluable support.

My graduate education would not have been possible without the love and support of my parents, Mary Sue Clark and Robert L. Clark. Finally, I thank my wife, Linda, and my daughter Shelby for their love, encouragement and patience. It is the context of their love that my accomplishments have meaning.

TABLE OF CONTENTS

1	Introduction and Organization of Thesis	1
I	Simulation Studies of Lipid Bilayers	3
2	Introduction	4
2.1	Lipids and Lipid Bilayers	5
2.2	Experimental Knowledge	13
2.2.1	Acyl Chain Structure	14
2.2.2	Atom Distributions	18
2.3	Theoretical (Non-Simulation) Approaches	19
2.4	Simulations	23
2.4.1	Molecular Dynamics Simulations	23
2.4.2	Monte Carlo Simulations	26
2.4.3	Brownian Dynamics Simulations	27
3	Molecular Dynamics Simulation Method	29
3.1	General Principles	29
3.1.1	The Verlet Algorithm	30
3.1.2	Periodic Boundary Conditions	32
3.1.3	Potential Truncation and Neighbor Lists	34
3.1.4	Application of Constraints	35
3.1.5	Constant Temperature and Pressure	37
3.1.6	Electrostatic Interactions	39
3.2	Specifics Related to Lipid Bilayers	40
3.2.1	Equilibration in Lipid Bilayer Simulations	40
3.2.2	Constant Pressure	41
3.3	Summary of Simulation Method	42
4	Analysis and Results	46
4.1	Order Parameters	46
4.2	C-C Dihedral Bond Analysis	49
4.3	Atom Distributions and Electron Density	53
4.4	Water Dynamics	55

5	Lipid Ripple Phase	58
5.1	Introduction	58
5.1.1	Experimental Knowledge	59
5.1.2	Theoretical Approaches	59
5.2	Model	63
5.2.1	Calculation of State Energies	63
5.3	Configurational-Bias Monte Carlo	67
5.4	Results & Discussion	71
II	Hybrid Monte Carlo Method Applied to Diamond	74
6	Introduction	75
7	Hybrid Monte Carlo Method	78
7.1	Equilibrium Monte Carlo Method	78
7.2	Kinetic Monte Carlo Method	80
7.3	Hybrid Monte Carlo Method	82
8	Diamond Film Growth	84
8.1	Chemical Vapor Deposition of Diamond	84
8.1.1	Experimental Knowledge	84
8.1.2	Theoretical Model	85
8.2	Diamond Simulation Method	89
9	Results & Discussion	93
	Bibliography	99

LIST OF TABLES

4.1	<i>Trans-gauche</i> conformers per chain	53
5.1	Ripple model states	64

LIST OF FIGURES

2.1	Molecular models of dimyristoyl phosphatidylcholine	6
2.2	<i>Trans</i> and <i>gauche</i> dihedral states.	8
2.3	Ryckaert-Bellemans dihedral potential	9
2.4	Initial bilayer configuration	11
2.5	Bilayer phases	13
3.1	Periodic boundary conditions	32
3.2	Charge distribution dimyristoyl phosphatidylcholine	43
3.3	Final bilayer configuration	45
4.1	Method of determining order parameters	47
4.2	Order parameter results	49
4.3	Method of determining dihedral angle	50
4.4	Dihedral bond distribution and <i>trans/gauche</i> fractions as a function of time	52
4.5	Atom distributions along the bilayer normal	54
4.6	Electron density along bilayer normal	55
4.7	Mean square displacement of water along bilayer normal	57
4.8	Diffusion constant of water along bilayer normal	57
5.1	Block models for lipids used in microscopic ripple phase model	61
5.2	Stacking of the L-block shapes for the gel and ripple phases	62

5.3	Hard wall surrounding lipid pairs	65
5.4	Typical disordered lipid pair configuration.	73
5.5	Energy of ripple model states	73
8.1	Initial Diamond Surface	88
9.1	Early formation of surface bonds	94
9.2	Early formation of surface chains and rings	95
9.3	Early formation of diamond nuclei	96
9.4	Growth of surface clusters	97

Chapter 1

Introduction and Organization of Thesis

With the invention of the computer a new branch of physics was born—computational physics. The very first electronic computer, the ENIAC, built in 1945, was used to solve physical, albeit military, problems such as the determination of artillery trajectories and (still classified) quandaries in nuclear physics [1]. In June of 1953, the first computer simulation of interacting particles was reported [2,3]. Since then, computer simulation has grown to become one of the most powerful techniques available to the physicist. To a large degree, this dramatic increase in use is due to the huge increase in computational power since the 1950's and, just as important, the huge decrease in price for these powerful computers. However, even low-cost, fast computers would be of no use if simulation methods did not give some insight into physics. Indeed, tremendous insight and information has been delivered to physics through the use of computer simulation.

Given the widespread use of computer simulation in physics, one should not be surprised that many different simulation methods have been devised. When designing a simulation of a particular model, many factors must be considered. Foremost is the quantity that is to be calculated. Then, the computational expense of the various simulation methods must be determined and compared with the available

resources. In this comparison of computational cost, not all currency is equivalent. A particular facility may have a super-computer containing a very fast processor while another may have a massively parallel computer containing many slower processors. Simulation methods that work very well on a parallel system may be very inefficient on a single processor system, and *vice versa*. So, each problem needs a simulation method tailored to the model and to the computational resources at hand. This situation has led to the creation of a large number of methods. In this thesis, two physical systems, lipid bilayers and diamond films, are studied using three computation techniques: molecular dynamics, configurational-bias Monte Carlo, and kinetic/equilibrium Monte Carlo. Since the two physical systems are quite different, it seems reasonable to divide the thesis itself into two distinct parts.

The first part details the study of dimyristoyl phosphatidylcholine (DMPC) lipid bilayers in the fluid-like liquid crystal phase and the modulated ripple phase. The liquid crystal phase is studied via molecular dynamics (MD) simulation. This work was performed in collaboration with S.-W. Chiu, V. Balaji, S. Subramaniam and E. Jakobsson at the University of Illinois, Urbana-Champaign, and results of the study have been published [4]. My role in this project involved primarily interpretation of data calculated by Chiu and Jakobsson. The ripple phase was modeled with a fifteen state lattice model that was determined using configurational-bias Monte Carlo (CBMC).

Part II of the thesis focuses on my work in the simulation of chemical vapor deposition (CVD) of diamond film. Development and implementation of a hybrid kinetic/equilibrium Monte Carlo method is presented as a method of incorporating events that occur on widely varying time scales into a single simulation. This work has also been published [5,6].

Part I

**Simulation Studies of Lipid
Bilayers**

Chapter 2

Introduction

Lipids are members of a large class of molecules known as amphipathic molecules. These species have two types of molecular groups or moieties. One moiety is polar and thus dissolves readily in polar solvents such as water but is insoluble in non-polar solvents such as oils. This type of molecular group is termed hydrophilic (literally, water loving). The other moiety is non-polar and thus does not readily dissolve in water although it does dissolve in oils. It is called hydrophobic (water fearing). When amphipathic molecules are dispersed in water, oil or both, a wide variety of structures can form as the two moieties are dissolved into their favored solvents and repelled by their unpreferred solvents. Lipids dispersed in water under proper conditions can form a membrane or bilayer structure. This structure consists of two adjacent sheets of lipids with their hydrophobic regions forming the interior of the membrane and their hydrophilic regions forming the exterior boundary (the water-lipid interface) of the membrane. Since 1925, when Gorter and Grendel speculated that erythrocyte lipid membranes formed a “bimolecular leaflet” from their experiments [7], the study of lipid bilayers has become a major topic of research in biology, chemistry, and physics. The notion that the lipid bilayer forms the underlying matrix of all biological membranes has produced several successful models of biomembranes which culminate in the now well established Singer-Nicolson Fluid Mosaic Model [7,8].

Although there is a wealth of general knowledge regarding biomembranes [7,9,10],

the study of natural biomembranes is complicated by the large variety of protein and lipid species that occur in them. These membranes perform many specialized biological functions, and general characterization is quite difficult. For this reason, most experimental and theoretical studies of the generic properties of biomembranes are performed on model membranes. These are bilayers constructed from purified species of lipid molecules. However, the properties of even the simplified model membranes are so complex, they have eluded complete experimental or theoretical description.

To further the knowledge of model membranes, many researchers have turned to computer simulation. Computer simulation provides insights into membranes that are not currently possible by either experiment or other theoretical methods. Specifically, computer simulation can access the details of the membrane at atomic resolutions. The resulting data can be used to further both the interpretation of experimental data and the construction of new theoretical models.

This chapter introduces a presentation of work based on a molecular dynamics (MD) simulation of a hydrated DMPC bilayer. The MD trajectory was calculated by Chiu and Jakobsson and results of the simulation have been reported [4]. In the next section, a brief discussion of the structure of a DMPC molecule and a hydrated DMPC bilayer is presented. Relevant experimental studies follow in the next section. The last sections of this chapter will consist of a discussion of relevant theoretical work, which will be divided into non-simulation and simulation sections. This separation is performed because of the practical differences between the two approaches and because computer simulations, particularly MD simulations, are currently the primary theoretical method for studying lipid bilayers.

2.1 Lipids and Lipid Bilayers

Figure 2.1 shows two molecular models of DMPC. Lipids in the phosphatidylcholine

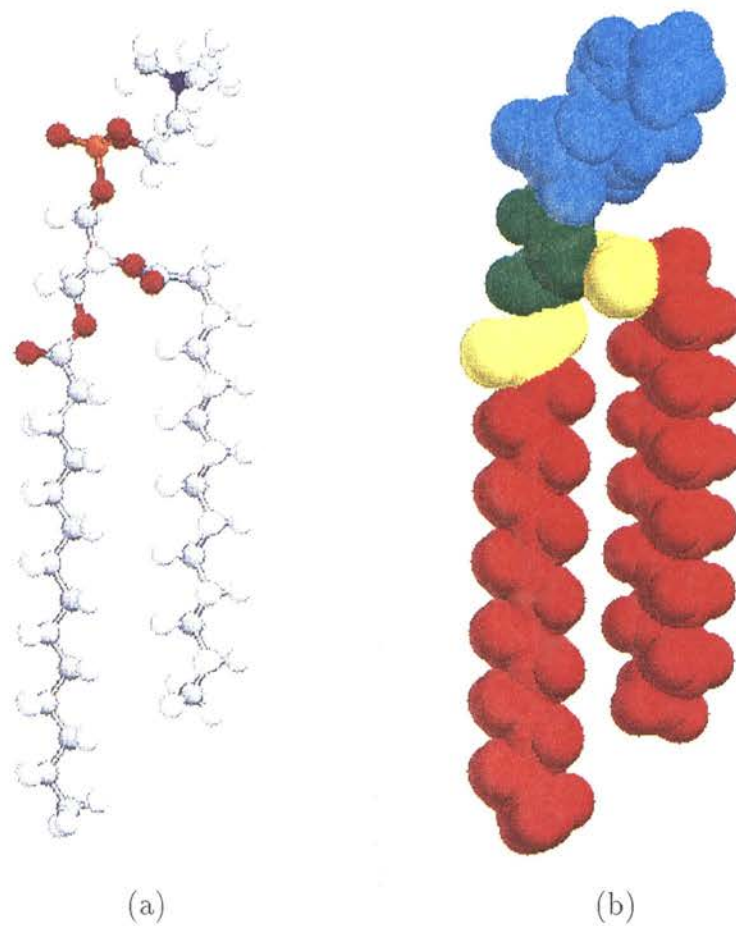


Figure 2.1: Molecular models of dimyristoyl phosphatidylcholine (DMPC). (a) A ball and stick model of DMPC identifying all atoms. The white atoms are H, the grey atoms are C, the red atoms are O, the blue atom is N, and the orange atom is P. (b) A space filling model of DMPC showing molecular moieties. The cyan colored atoms form the phosphatidylcholine headgroup. It is connected to the rest of the molecule by the glycerol 'backbone' shown in green. Ester linkages, shown in yellow, connect the glycerol to the two acyl chains, shown in red.

(PC or lecithin) class have this basic structure and differ only in the length and saturation of the acyl chains. In Figure 2.1(a), the molecule is shown using a ball and stick representation so that the molecule's structure can be easily seen. The various atoms are colored by their standard colors: hydrogen is white, carbon is grey, nitrogen is blue, phosphorus is orange, and oxygen is red.

Figure 2.1(b) shows the molecule using a space filling model so that the shape of the molecule is seen. The colors divide the molecule into the polar (hydrophilic) headgroup region, shown in cyan, and the acyl (hydrophobic) chain region, shown in red. Shown in green is the glycerol 'backbone' that holds the hydrophobic and hydrophilic moieties together. The ester linkages or carbonyl groups that connect the acyl chains to the glycerol are polar and indicated by yellow.

The headgroup is multi-polar, with every atom from the headgroup down to the chain carbonyls effectively having a non-zero charge [4]. However, the choline group ($\text{N}^+(\text{CH}_3)_3$) has an excess charge of $+e$ centered near the nitrogen atom. The phosphate group (PO_4^-) possesses an excess charge of $-e$ centered near the phosphorus atom [4]. Thus, there is a electric dipole going approximately from the phosphorus atom to the nitrogen atom which is often referred to as the headgroup dipole.

Of primary importance in the discussion of lipid structure and bilayer properties is the conformational structure of the lipid chains. The usual method of describing the rotameric structure of the chains is by specifying the dihedral (torsional) angles of each C-C bond in the chain. The definitions of the dihedral angle and representative dihedral states are shown in Figure 2.2. A dihedral angle is described by four atoms. Figure 2.2(a) shows four carbon atoms with sticks indicating the tetrahedral bonding sites of the sp^3 atoms. If all these sites were to contain hydrogen, Figure 2.2(a) would depict a model of *n*-butane. In Figure 2.2(b), the same set of four atoms are oriented such that the bond between the inner two carbons lies normal to the page, obscuring

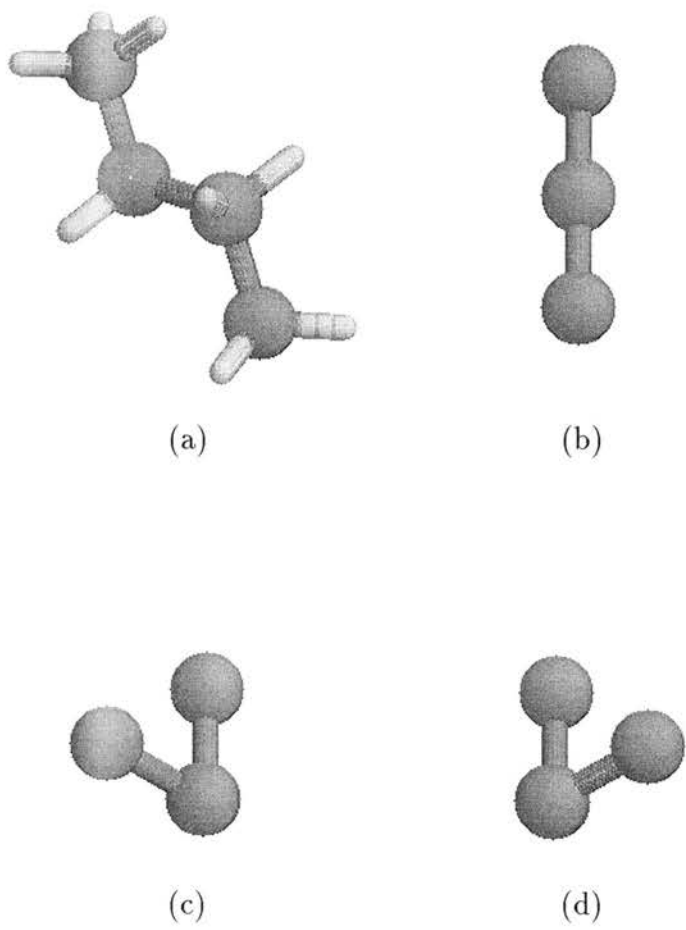


Figure 2.2: *Trans* and *gauche* dihedral states. (a) Four C atoms shown in the *trans* configuration with tetrahedral structure depicted by protruding sticks. The dihedral angle indicates rotations about the central C-C bond. (b) Atoms arranged in the *trans* position as viewed with the central C-C bond normal to the page. (c,d) Atoms arranged in the two *gauche* states also oriented with the central C-C bond normal to the page.

one of the atoms. The atoms of Figures 2.2(a,b) are in the *trans* (straight chain) configuration. Figures 2.2(c,d) show the atoms in the two *gauche* positions. These positions represent consecutive 120° dihedral rotations about the hidden, inner bond. The use of the *trans* and *gauche* states is useful in describing chain conformations because the dihedral angle potential energy for alkane chains has three distinct minima at the *trans* and *gauche* positions. This can be seen in Figure 2.3. This figure shows

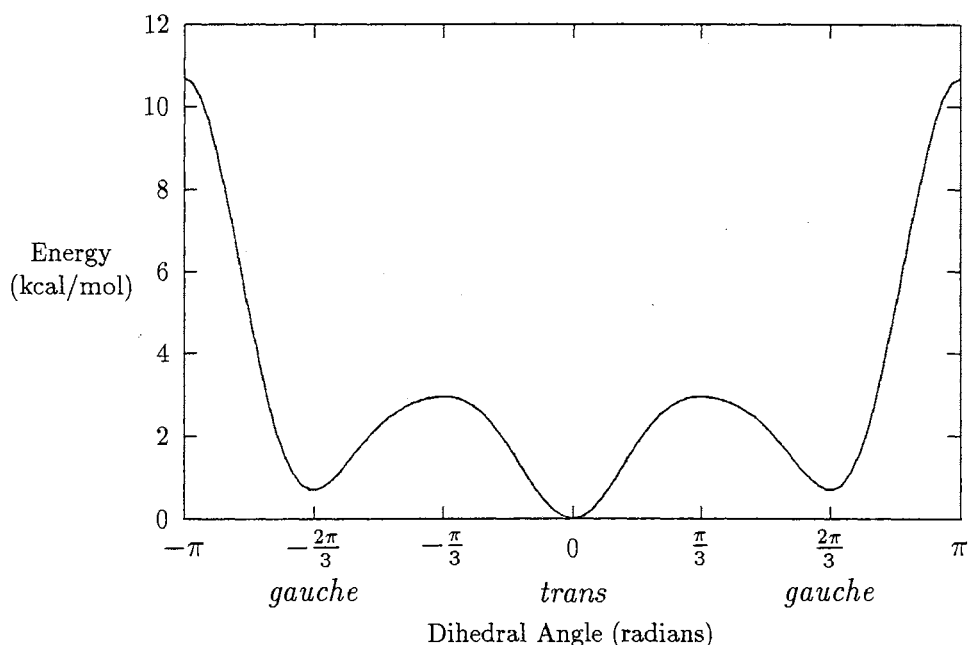


Figure 2.3: Ryckaert-Bellemans dihedral potential [11]. The minimum are designated as *trans* or *gauche* as indicated. The potential is of the form $\sum_{i=0}^5 a_i \cos^i \phi$ with ϕ representing the dihedral angle. The constants a_i were determined for *n*-butane by fitting to experimental data. In units of kcal/mol, they are $a_0 = 2.217$, $a_1 = 2.905$, $a_2 = -3.135$, $a_3 = -0.731$, $a_4 = 6.270$ and $a_5 = -7.526$.

a plot of the torsional potential determined by Ryckaert and Bellemans [11] for *n*-butane. Thus, the dihedral angles of an isolated alkane chain prefer to take on three distinct values corresponding to the potential minima of the *trans* and *gauche* states. Note in Figure 2.3 that global minimum lies at the *trans* position, and the *gauche* minima are equal (as they must be from symmetry).

When DMPC is dispersed in water, the hydrophobic chains are attracted to each other and are repelled by the water. The polar headgroups and carbonyls, on the other hand, dissolve into the water. This behavior can lead to the self-assembly of a large variety of water lipid structures—a phenomena know as lipid polymorphism [7]. The type and phase of a lipid-water mixture is determined by several factors such as species of lipids and their relative proportions, temperature, and water concentration or level of hydration. The structures that form can be divided into three categories: micelles, and hexagonal structures and lamellar structures.

Micelles are globular aggregates of lipids. They are balls of lipid whose interiors hold the non-polar chains while the exterior surface, exposed to water, is covered with the polar headgroups. The size and shape of micelles can vary. Microscopic and mesoscopic sizes can be formed and they can take on regular shapes such as spheres or rods.

Hexagonal phases consist of cylindrical structures which are packed in a hexagonal lattice (as viewed down the cylinder axes). There are two types of hexagonal phases. At high water concentration, the cylinders are surrounded by water, the outer surfaces formed by the hydrophobic moieties, and the inner cores containing the hydrophobic chains. At low concentrations, the cylinders become inverted with the headgroups and water forming the cylinder cores and the chains forming the cylinder surfaces.

The last type of structure is the lamellar bilayer. Here, the lipids form large (in many cases macroscopic) sheets. The dissolved headgroups make up the outer surface of the bilayer and the acyl chains form the bilayer interior as shown in Figure 2.4. The lipid chains are shown as green sticks while the headgroup atoms are shown as red balls. The water molecules are shown in blue and white indicating O and H, respectively.

Lamellar structures can form larger structures. Multi-lamellar bilayers are struc-

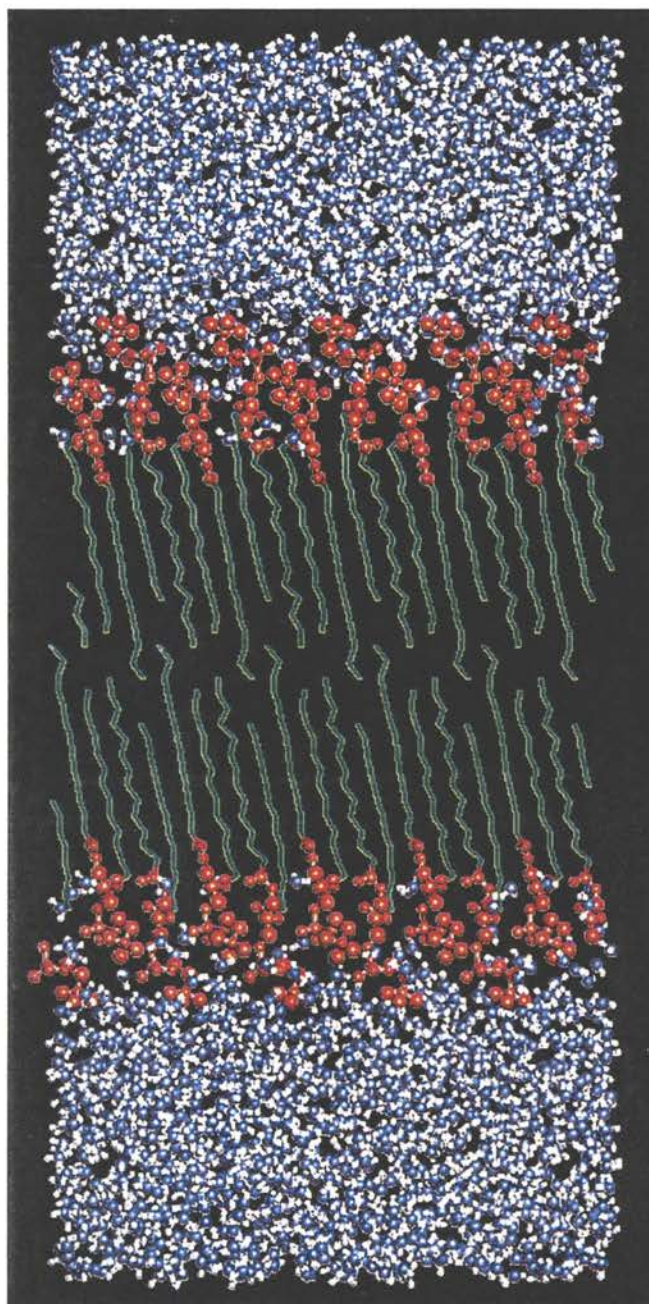


Figure 2.4: Hydrated bilayer of dimyristoyl phosphatidylcholine (DMPC) molecules. The DMPC alkane chains are depicted as green sticks while the headgroup atoms are depicted as red balls. Water oxygen is colored blue and water hydrogen is colored white.

tures of many bilayers stacked on top of each other. These systems can exist with many randomly oriented multi-lamellar domains ('powder' samples), or they can be formed on a solid substrate such that all bilayers are parallel (oriented bilayers).

The bilayer membrane can also be formed to enclose a volume like a balloon. These bilayer balloons are called liposomes or vesicles and come in various forms. If the vesicle membrane is a single bilayer, it is known as a unilamellar vesicle. These come in three sizes, small unilamellar vesicles (SUV's) which have diameters $\sim 250 \text{ \AA}$, large unilamellar vesicles (LUV's) which have diameters $\sim 500\text{--}2,000 \text{ \AA}$, and cell-sized unilamellar vesicles which have diameters as large as $\sim 300 \mu\text{m}$ [7]. If the vesicle is made up of multi-lamellar bilayers it is called a multi-lamellar vesicle (MLV).

More variety in these systems is seen by the phases individual bilayers can take on. Examples of bilayer phases are shown in Figure 2.5. Again, the particular phases that a bilayer takes on depends on the types and mix of lipids, hydration, temperature, *etc.*. At lower temperatures, the bilayer chains become elongated as they drop to their lowest conformational state, the straight chain or all-*trans* conformation. This produces rigid molecules that pack in specific manners depending upon the type of lipids involved. This phase is known as the gel (L_β) phase and is shown in Figure 2.5(a). (Figure 2.4 is also an example of a gel phase bilayer.) As the temperature is increased, some lipids undergo a transition to a ripple ($P_{\beta'}$) phase, shown in Figure 2.5(b). This phase is similar to the gel phase since the chains are still primarily rigid, but instead of a planar structure, the ripple phase exhibits a corrugated surface. Finally, at higher temperatures, the bilayer chains become disordered as high energy conformations become thermally activated. The bilayer is once again locally planar and is much more flexible. In addition, the lipids can readily diffuse in the plane of the bilayer. This fluid-like phase, shown in Figure 2.5(c), is known as the liquid crystalline (L_α) phase. It is the biologically relevant phase; the diffusion of proteins and membrane flexibility

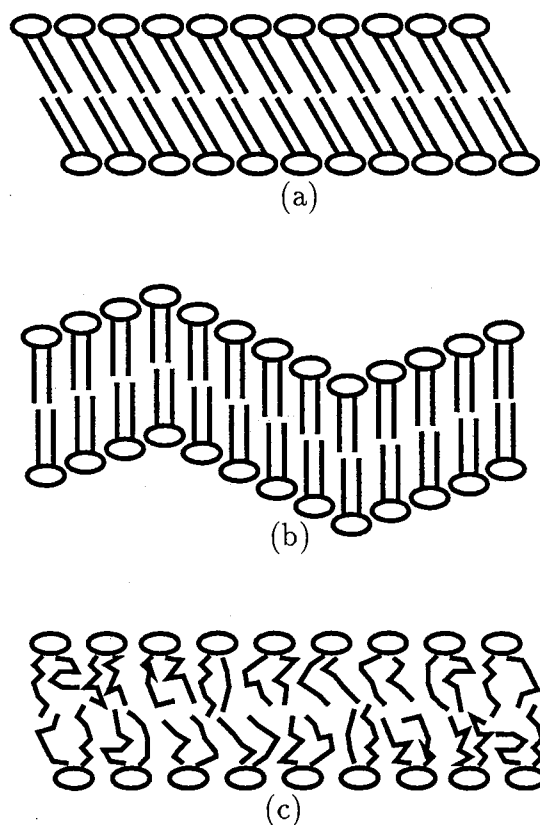


Figure 2.5: Three possible phases of a lipid bilayer. (a) The gel phase has tilted, densely packed all-*trans* chains. (b) The ripple phase also has *trans* chains but possesses a periodic undulation of the bilayer surface. (c) The liquid crystal phase has disordered chains and is less dense than the gel or ripple phases.

required for life require the fluid nature of the liquid crystalline phase bilayer.

Liquid crystal bilayers are the subject of the present discussion (the ripple phase is the focus of Chapter 5). So, we now turn our attention to the experimental data gathered on liquid crystal bilayers.

2.2 Experimental Knowledge

Since simulations provide detailed information about the atomic structure and dynamics of a bilayer on very short time scales, experimental results of primary interest to this discussion are those that produce information about atomic structure and measure average properties of fast processes. So, for example, nuclear magnetic res-

onance (NMR) studies and X-ray diffraction studies are useful in this context since both depend only on atomic structure and processes fast enough to be adequately averaged in a simulation. On the other hand, data on processes such lipid flip-flop between bilayer leaves, thermodynamic phases, or membrane flexing/splaying motions are not very useful since they involve processes that take times much longer than can be simulated or, in the case of flexing/splaying motions, would require the simulation of many more lipid molecules and water than is currently possible.

In this section, we shall explore the experimental results obtained from studies of model liquid crystal phase phospholipid bilayers. We will concentrate on empirical data that is useful in the study of such bilayers via simulation or that can be better interpreted using simulations.

2.2.1 Acyl Chain Structure

The best experimental measure of the acyl chain order in liquid crystal phase lipid bilayers is the S_{CD} order parameter determined by deuterium nuclear magnetic resonance ($^2\text{H-NMR}$). These NMR experiments are performed on lipid bilayers in which some or all of the hydrogen of the acyl chains has been substituted with deuterium. The orientational order parameters measured by $^2\text{H-NMR}$ are defined by

$$S_{CD} = \left\langle \frac{3}{2} \cos^2 \theta - \frac{1}{2} \right\rangle. \quad (2.1)$$

Here, θ is the angle made between the bilayer normal and a vector which runs from the deuterated carbon to the deuteron. The angled brackets indicate averaging.

There are several reasons why $^2\text{H-NMR}$ is an important tool for measuring acyl chain order. First of all, by using selectively deuterated samples, the order parameter can be measured as a function of carbon position along the chains. The $^2\text{H-NMR}$ spectra produced by such samples are extremely simple; for each deuterated position, a well resolved doublet appears [12-14]. Furthermore, interpretation of this doublet is

straightforward, requiring few *a priori* or *ad hoc* assumptions regarding the structure of the bilayer [12,13]. Finally, the substitution of a deuteron in place of a hydrogen does not significantly perturb the conformations of the chain being studied [12,15].

The theoretical basis of ^2H -NMR rests in the fact that deuterium possesses a electric quadrupole moment and this quadrupole moment dominates all other interactions except for the Zeeman term [13]. In the high-field approximation, the quadrupolar interaction is taken as a perturbation to the Zeeman splitting, and if the lipids are axially symmetric about the bilayer normal, the average quadrupolar splitting is proportional to S_{CD} [12,13]:

$$\langle \Delta\nu_Q \rangle = \frac{3}{4} \left(\frac{e^2 q Q}{h} \right) (3 \cos^2 \beta - 1) S_{\text{CD}}. \quad (2.2)$$

In this expression, e is the charge of the proton, q is the dominant electric field gradient reduced by e , Q is the quadrupole moment of deuterium, and h is Planck's constant. Finally, β is the angle made by the bilayer normal and the externally applied magnetic field. So, S_{CD} is easily taken from ^2H -NMR for oriented bilayers, for which β is known [16].

In unoriented or 'powder' samples, the signal is a superposition of splittings due to a collection of bilayers whose normal directions are uniformly distributed over a sphere [12]. This averaging removes β from the Equation 2.2. If the line broadening effects are ignored, the resulting spectra produce a feature known as a Pake doublet [14] which has an average difference in frequency given by [12]

$$\langle \Delta\nu_Q \rangle = \frac{3}{4} \left(\frac{e^2 q Q}{h} \right) S_{\text{CD}}. \quad (2.3)$$

Corrections for the line broadening can be made for a known or assumed lineshape.

Despite the straightforward interpretation of ^2H -NMR spectra, there are some sources of error such as line broadening and spectral distortion. However, these sources produce only small errors in S_{CD} and are well understood; they should not

cause problems in the interpretation of the results [12,13]. Thus, ^2H -NMR experiments are an ideal method for determining average orientational order of the acyl region of liquid crystal bilayers. One must be cautious, however. Even though the interpretation of the data is a simple matter, interpretation of their meaning is not so straightforward. There are many possible structures and dynamics that can give rise to a particular value of S_{CD} . Simulation order parameters can be compared with experimentally measured parameters to help establish the validity of the simulation. Conversely, the atomic level detail of the simulations can be used to determine the structure and dynamics that produce measured order parameters.

Infrared (IR) spectroscopy provides another method of determining chain structure in liquid phase lipid bilayers. These studies complement the average orientation measurements from ^2H -NMR by providing data on specific chain conformations. IR absorption measurements identify vibrational modes of molecules. As such, they measure phenomena that occur on a much faster time scale than ^2H -NMR measurements; ^2H -NMR measurements represent averages over times $\sim 3 \times 10^{-6}$ s [14] while IR measurements typically measure motions with characteristic times $< 10^{-12}$ s [17]. For this reason, the lipid rotamer motions occurring on these faster times will not be averaged over as in the ^2H -NMR studies. Such motions as *trans-gauche* isomerization will appear ‘frozen’ on this time scale [18]. The practical use of these measurements applied to acyl chain structures comes from the ability to assign particular frequencies to particular rotameric conformers. Detailed information about chain conformations can be found from CD_2 rocking modes and CH_2 wagging modes.¹ The information these two modes provide are complementary. The CD_2 rocking modes can be used to identify the ratio of *trans* (*t*) rotations to *gauche* (*g*) rotations at a particular chain

¹The CD_2 rocking mode consists of the movement of the C-D bonds, in unison, parallel to the plane defined by the C-D bonds. The CH_2 wagging mode consists of the movement of the C-H bonds, in unison, perpendicular to the plane defined by C-H bonds.

segment, and the CH₂ wagging modes indicate the number of kink (*g'tg*, where the prime indicates the two *gauche* rotations are in opposite directions) rotations and end *gauche* (*eg*) rotations present.

For selectively deuterated chains, the CD₂ rocking mode depends upon the local conformation of the chain. From a careful analysis of the normal modes of *n*-alkanes, Snyder and Poore determined the frequencies associated with the conformations of an isotopically isolated CD₂ group [19,17]. Specifically, they determined the CD₂ adsorption bands associated with two-dihedral (CH₂-CD₂-CH₂) conformations: *tt*, *tg*, and *gg* [17]. In addition, CD₂ rocking bands have been identified with three four-dihedral (CH₂-CH₂-CD₂-CH₂-CH₂) conformations: *gtgt*, *g'tgt*, and *ttgt* [17]. The fraction of *trans-gauche* isomerizations can thus be calculated by the intensity ratio of frequencies indicating *gauche* rotations to frequencies indicating *trans* rotations, taking into account the relative absorptivity of these modes [20]. However, the relative absorptivity of these modes are not known *a priori*. The most accurate method of calculating them is to use a combination of spectra from *n*-alkanes and Flory's rotational isometric state (RIS) model [21]. The RIS model assumes ideal chains (i.e., chains which do not interact with each other) for which rotations are limited to a set of discrete values (the *trans* and *gauche* minima) [22]. Using this model, the concentration ratios of the rotameric states can be calculated for *n*-alkanes. These concentration ratios can be divided into intensity ratios taken from *n*-alkane spectra to estimate the relative absorptivity of the the *gauche* and *trans* CD₂ rocking modes.

CH₂ wagging modes allow measurement of *gtg*, kink and terminating *eg* rotations for which the CD₂ rocking modes cannot differentiate [23]. These conformations exhibit specific IR absorption bands due to the CH₂ wagging [17]. Again, to calculate absolute numbers, say percentages of kinks, the relative absorptivities are necessary. These are also calculated using the RIS model coupled with the analysis of *n*-alkanes

[20].

There is much room for error in these IR measurements and subsequent interpretations. In the first place, the relative absorptivities are not unambiguously known. Use of the RIS model requires the input of the energy difference between the *trans* and *gauche* states. The absorptivities vary significantly with this energy change—by a factor of two over a range of 400 cal/mole. Also, they depend on chain length. For longer chains, larger values of the relative absorptivities are found. Snyder and Poore [19] point out these dependencies as well as other discrepancies which may be due to the RIS model underestimating the ratio of *tt* pairs to *tg* pairs. Also, one must consider that absorptivities are calculated using spectra from *n*-alkanes and may differ from the absorptivities of the more ordered alkane chains in lipid bilayers [20]. Along technical lines, it is reported that cholesterol and gramicidin D, common components of membranes, as well as H₂O and D₂O all absorb in this same region, so careful subtraction of this background is necessary [20,17]. Aside from these extraneous components, there are similar types of complications in pure membranes [21]. For example, there is an overlap of the CD₂ rocking band and the intense CH₂ rocking bands; the CH₂ rocking band does not possess a simple shape, so subtraction of its contribution is problematic. Finally, isotopic impurities lead to CHD rocking modes which obscure the CD₂ band.

2.2.2 Atom Distributions

The average distribution of particular lipid atoms and water are very difficult to determine experimentally. Conversely, computer simulations can provide very detailed atomic distribution data. So, this is a case where simulations can potentially enhance interpretation of experimental data. A good example of this is electron density data generated by X-ray diffraction [24,25]. In these experiments, low-angle X-ray

diffraction patterns can be utilized to determine the electron density profile perpendicular to the bilayer [24]. Since the lipid headgroup contains heavy atoms relative to the chains, the electron density can be used to roughly locate headgroup and chain atoms. But, the resolution does not allow the location of specific atom positions. Nonetheless, the electron density can be easily calculated in a computer simulation, and, thus, electron density experiments should be used to test the validity of a simulation. Recently, atom distributions and electron density profiles calculated from simulations have been used to test methods of determining the membrane area per lipid molecule from X-ray diffraction data [25].

2.3 Theoretical (Non-Simulation) Approaches

Another area of interest to the current discussion are analytical theoretical endeavors that provide insight into the structure and dynamics of the liquid crystal phase bilayer. There are relatively few such analytical studies outside direct simulation, owing to the complexity of liquid crystal bilayers. We provide a brief overview of analytic methods in this section before concentrating on simulations in the next.

When modeling a lipid bilayer system, the theoretician must take into account several interactions that are quite difficult to study analytically [26,14], such as the chain dihedral interaction, the van der Waals interactions, and the electrostatic interaction. The dihedral interaction is problematic because of the very large number of possible rotameric states a chain may assume, many of which may be restricted by van der Waals repulsion (excluded volume interactions). The van der Waals interactions are problematic because of the anisotropic nature of the lipid chains. Even though the van der Waals interaction between individual particles is radially symmetric, the restriction of the particle positions by the chemical bonds of the acyl chains imposes a distinct anisotropy. This anisotropy is acute in the restriction of chain conformations

by excluded volume interactions. For this reason, the repulsive van der Waals interaction is usually incorporated separately from the attractive van der Waals interaction [26,27,14]. The electrostatic interaction is difficult to model because of the complex nature of the charge distribution in the lipid headgroup and the complex interactions with the electric dipoles of the surrounding water. Additionally, the electrostatic interactions are long range in nature requiring special techniques to properly account for long range correlations.

The complexity of the system requires theorists build abstract models, simplifying the interactions until only the most important contributions are left. There have been many such attempts, and there are several reviews of the various approaches [26,14,28]. Each theory has its own advantages and disadvantages, and each taken alone would not serve as a very complete understanding of a lipid bilayer. However, the various approaches taken together do help create an understanding of the vast array of issues involved in describing a bilayer. With this in mind, it seems more useful to discuss the common features of the various models to produce an understanding of the general theoretical concepts used to describe membranes than to describe each model in detail.

A critically important feature of all the models is the rotameric degrees of freedom. This is because the most important contribution to the gel to liquid crystal phase transition is the disordering of the the hydrocarbon chains through *trans-gauche* isomerization. This is evident from comparisons of X-ray diffraction spectra of bilayers and long chain alkanes whose only significant degree of freedom is rotameric [26,27]. Furthermore, calorimetry studies have shown that the transition enthalpy is large, ~ 9 kcal/mole for the palmitoyl (C_{16} chain) phospholipids, which indicates a large change in entropy, equivalent to over twenty two-state spins. This large change in entropy can only be explained via activation of rotameric degrees of freedom [27]. The

fundamental difference between gel and liquid membranes rests in the disordering of rotameric states.

Another critical feature that is universally included in some fashion is the excluded volume and the intrinsic anisotropy of the chains. The chains must, of course, be anchored to the headgroup, hence the anisotropy. Then, the neighboring chains prevent individual chains from disordering independently. Due to the steric repulsion, the chains can disorder only through cooperative movement [26].

Finally, an attractive term is needed as well. The van der Waals interaction between the chains is usually included in statistical models. Although the water/headgroup interaction is critical in the formation of the bilayer, the chain/chain attraction coupled with the steric repulsion is the primary determining factor of molecular packing detail [26].

Just as insightful into the current state of lipid bilayer theory as the features almost universally incorporated are the features that are almost universally ignored. The interactions between polar headgroups and the two leaves of the bilayer are often neglected, and the fact that the two chains are bonded to a single headgroup is ignored in many cases [26,28]. These approximations are actually quite reasonable. The headgroup interactions, particularly the interactions with water, are necessary for the formation and stability of the bilayer structure. However, this is their primary effect, and the bilayer structure is *a priori* included in all models [26]. The interaction between the two bilayer leaves are considered to be small due to the agreement between monolayer and bilayer studies [27]. Specifically, both monolayer and bilayer systems exhibit a phase transition at similar temperatures and surface pressures [26]. Finally, with headgroup interactions neglected, the two chains of a particular lipid can be thought of as independent. In fact, since the chains are attached to the limber glycerol moiety, to rigidly pair the chains may be a more erroneous approximation

than no pairing altogether [26].

These general features of bilayer modeling have been applied by several researchers and all have had varying degrees of success using quite different methods and approximations [14,26,28,29]. Thus, they serve to indicate that the ideas behind the common features of the models are correct. A few of the more notable studies are due to Nagel, Marčelja, Scott and Pink. Nagel constructed two simple, exactly solvable order-disorder models of a lipid membrane [30]. These models, while two-dimensional and having infinite chains, showed that a model can explain the main gel to liquid crystal phase transition using energy contributions from van der Waals attraction, isomeric rotation and steric repulsion. Marčelja took a mean field approach, utilizing a pressure term to model the steric repulsion and a mean field expression for the attractive van der Waals energy [31,32]. The mean field method reproduces the ^2H -NMR order parameters and has subsequently been adopted into some molecular dynamics boundary conditions discussed below. Scott has utilized hard core modeling techniques. One method utilized an approximation (the Flory approximation) to determine the sterically limited conformations of a two-dimensional lattice model [33]. Another, more versatile, model describes lipids as two-dimensional rods, representing the area in the plane of the bilayer required for the lipid in various conformations [29,34,35]. The hard core models show, again, that steric repulsion coupled with chain disordering are primary factors in the lipid gel to liquid phase transition. Finally, Pink utilized a lattice model incorporating specific enumeration of conformational states considered ‘intermediate’ between the gel (all-*trans*) state and a high energy ‘melted’ state [28]. The attractive van der Waals interaction was incorporated using a mean field approximation and the steric repulsion was incorporated in the selection of the intermediate states—states were selected that could be expected to form with little steric hindrance from neighboring molecules. This modeling effort also resulted in

many qualitative agreements with experiment [28].

2.4 Simulations

The theoretical treatments discussed above have explained various aspects of the gel to liquid crystal phase transition. In general, however, they do not bring out detailed structural information about the liquid crystal phase itself. Moreover, none of the studies provide dynamical information. The system is simply too complex to model with lattice models and mean field theories and, at the same time, provide this information. The approximations made to focus on the most important processes can only provide information about those select processes. Still lacking in both the experimental and theoretical approaches discussed so far is a description of liquid phase bilayers at atomic resolutions. Computer simulations can provide this. Lipid membrane simulations have been reviewed recently by Pastor [36] and by Damodaran and Mertz [37].

2.4.1 Molecular Dynamics Simulations

As with the simulation of most physical systems, atomic scale computer simulations of lipid monolayers and bilayers began utilizing simple models and progressed to very complicated ‘realistic’ models. Thus, the first bilayer MD simulations carried out were similar to the other theoretical treatments in that they concentrated primarily on the acyl chain region while grossly simplifying the headgroup structure and interaction. For example, the early work of van der Ploeg and Berendsen consisted of MD simulations of decane chains whose ‘headgroups’ (i.e., one of the terminal CH_3 groups) were anchored to the bilayer plane by a harmonic potential in the direction of the bilayer normal [38,39]. However, the simulation was termed ‘realistic’ by the authors since a continuous and realistic dihedral potential, full van der Waals interactions (although,

CH_2 and CH_3 groups were modeled as ‘unified atoms’ (or single Lennard-Jones particles) and harmonic bond angle potentials were explicitly included. Even though the headgroup interactions were ignored, the simulation produced a wealth of data that could not be determined from the other theoretical treatments such as chain tilting information, radial distributions of headgroups, density profiles, and components of the pressure tensor.

Subsequent MD simulations have grown increasingly realistic, with more detailed descriptions of headgroups, electrostatic interactions and interaction parameters. For instance, Egberts and Berendsen expanded on the early simulations of van der Ploeg and Berendsen by adding in charged headgroups and water using constant pressure MD methods [40]. Detailed water/phospholipid studies were performed by Berkowitz, although lipid chains were held rigid [41,42]. Since then, there have been many simulations of phospholipid bilayers including full headgroups and water [43-55]. Some of these simulations were primarily focused on structural aspects of bilayers such as headgroup/water interactions [44,46,51,55] and lipid packing [50]. Several others were aimed at testing simulation methods themselves. Shinoda and co-workers investigated the Nosé-Parinello-Rahman NPT ensemble [53], Tu and co-workers show that a NPT simulation with isotropic pressure can produce stable bilayers [54], and the application of various simulation methods proposed by Zhang [56] were carried out in the simulations performed by Feller and co-workers [52].

The most recent simulations are similar in that they include atomic detail and complex, ‘realistic’ potentials. However, they are not equivalent. They utilize different potential parameters and differ in system size and length of time simulated. But, more important, they differ in the types of ensembles simulated and the type of boundary conditions applied. Many of the early simulations were performed in the constant particle number, volume and temperature (NVT) ensemble [41-45,48,51].

This ensemble requires the *a priori* input of the bilayer density. In particular, the value of the bilayer surface area per lipid is not easily obtained from experiments [57,25]. Several others simulated bilayers using constant pressure in favor of constant volume (the *NPT* ensemble) [46,49,50,52-55]. This ensemble removes the need to know the area per lipid in advance; however, it suffers from needing to know the pressure, and thus the surface tension, in advance.

Since the patch of membrane that can be simulated is minuscule compared to a real membrane, the treatment of boundaries is an important aspect of a simulation. Generally, the researcher wants to create an environment as close as possible to an infinite membrane. The vast majority of bilayer simulations use periodic boundary conditions. Most of the recent simulations utilize periodic boundaries in three dimensions [41,42,44,46,48-55], although Stouch performed a simulation with periodic boundary conditions only in the plane of the bilayer while using repulsive walls to contain water in the direction normal to the bilayer [47]. An alternative to periodic boundary conditions is mean field stochastic boundary conditions used in a few simulations [43,45]. In these simulations, the molecules on the edge of the simulation cell are subjected to an external force comprised of stochastic noise and a mean field potential based on Marčelja's model. Although computationally more efficient than periodic boundary conditions, this method introduces uncontrolled errors into the boundary lipids.

The details of force calculations and equilibration of the systems vary for each simulation and will not be addressed here. However, a few novel technical details deserve note. In order to more fully equilibrate their bilayer, Venable *et al.* simulated individual lipid molecules in a Marčelja mean field to 'randomize' the molecules before placing them in a bilayer configuration [48]. Shinoda and co-workers tested the use of the Nosé-Parinello-Rahman *NPT* ensemble featuring periodic boxes that can change

shape (the cell angles can vary) [53]. They found that utilization of this ensemble lead to less dependence on initial conditions and the elimination of artifacts such as collective chain tilt.

A wealth of atomic resolution data has been generated by the simulations discussed above. S_{CD} order parameters were calculated in most of the studies [38-40,43-45,47-55]. The distribution of atoms across the bilayer were also commonly reported [38-47,49,50,53,55] as were radial correlations between various atoms or groups [38-42,44,47,49,54,55]. Electron density was calculated in many studies [40,44,47,49-51,54,55] as were statistics regarding chain structure such as chain tilt and chain *trans* or *gauche* isomerization [38-40,47,49-51,53]. Several also reported data on chain dynamics such as *trans-gauche* reorientational correlations [38-40,43,47-49,51,55]. Detailed data on headgroup/water interactions such as orientational statistics of water and headgroups, mean squared displacement of water, and diffusion coefficients of water were frequently reported [41,42,44-47,49,51,52]. The surface dipole potential was calculated in two of the studies [46,55]. Finally, pressure or surface tension data was reported by a few of the *NVT* studies [43,45,52], while the area per lipid was reported by several of the *NPT* studies [46,50,52-54].

2.4.2 Monte Carlo Simulations

Although, MD simulations of lipid bilayers is the focus here, it is not the only simulation method that has been employed to study liquid bilayer systems. In fact, MC simulations of monolayers preceded MD simulations of monolayers by fourteen years [58,59]. Still, there are substantially fewer MC simulations of bilayers than MD simulations. Several studies based on Metropolis sampling [2] have been used to study monolayers and bilayers focusing primarily on chain order [58,60-68]. But, of these, only three directly simulate a bilayer [62,65,68]. The Metropolis based simulations

are of relatively simple systems, compared with MD simulations, but they offer the advantage of sampling structures that MD simulations are currently unable to sample because they occur on relatively long time scales. Most use lattice models; only the work of Scott [60,61,64,69,35,70-72] and Taga [68] do not fix the atoms on lattice points.

MC simulations of bilayers are simpler than MD simulations primarily because the Metropolis sampling is quite inefficient for bilayer systems; attempted MC moves are likely to lead to steric overlaps among the densely packed chains and thus be rejected. This is especially true of rotations about torsional bonds which often extend atoms below the torsional bond into the neighboring chains. For this reason, MC simulations of bilayers have been smaller in size and none have explicitly included water—to properly include water would greatly increase the system size and therefore the amount of MC moves required. However, soon MC simulations may rival MD in both size and realism. Configurational-bias Monte Carlo [73-77] (CBMC) has already proven to dramatically increase the efficiency of chain simulations [74,75,77-80]. This method was utilized in sampling disordered chain configurations in the ripple phase and is described in Chapter 5.

2.4.3 Brownian Dynamics Simulations

Another alternative to MD simulation is Brownian dynamics (BD) simulation (also referred to as Langevin or Stochastic dynamics) [36,37]. These studies are akin to MD studies except they add a random force term along with a mean field term to account for boundary and/or solvent interactions which are otherwise not explicitly included in the potential [81-83]. In a sense, they form a link between MC simulations and MD simulations. The advantage of BD is the reduction of computational cost; the disadvantage is that details of important interactions are lost, and, consequently,

many different models can produce the same results [36]. (This is not unlike the situation in the analytical theories of bilayers.) In addition, the errors of the mean field used will likely be transferred in an unknown manner into the particle trajectories. Finally, BD dynamics do not conserve energy and the trajectories are not reversible [37]. Thus, as Pastor notes in his review, BD simulations should be backed by more detailed simulations [36].

Chapter 3

Molecular Dynamics Simulation Method

We now turn to the details of the Molecular Dynamics (MD) method itself. This chapter begins with a general description of the MD method in Section 3.1 and narrows its scope to bilayer simulations in Section 3.2. Finally, specific details regarding our simulation are discussed in Section 3.3.

3.1 General Principles

Despite the simple nature of the MD concept, its application can be quite complicated. For excellent discussions of the application of MD methods to complex systems see the text by Allen and Tildesley [81] or Rapaport [84]. Much of the discussion in this section comes from these sources.

MD methods are used to solve the classical equations of motion of a system of particles. The task at hand is to determine an algorithm that can be programmed into a computer to solve these equations. There are several possible numerical procedures depending on the nature of the equations, but one of the most common is the Verlet method.

3.1.1 The Verlet Algorithm

The Verlet algorithm [85], like the majority of numerical solution methods, is a finite difference method. That is, a derivative is approximated by an expression of the form

$$\dot{x} \approx \frac{x(t+h) - x(t-h)}{2h}. \quad (3.1)$$

Here, the dot indicates differentiation with respect to time t and h , the time step size, is a small increment in time.

Consider the equations of motion as formulated by Newton:

$$m_i \ddot{\mathbf{r}}_i = \mathbf{f}_i, \quad (3.2)$$

the mass of the i th particle m_i multiplied by its acceleration $\ddot{\mathbf{r}}_i$ is equal to the total force acting on the particle \mathbf{f}_i . Vector quantities are indicated by the bold typeface.

Taylor expansions of the displacement \mathbf{r}_i give

$$\begin{aligned} \mathbf{r}_i(t+h) &= \mathbf{r}_i(t) + h \dot{\mathbf{r}}_i(t) + \frac{1}{2} h^2 \ddot{\mathbf{r}}_i(t) + \dots \\ \mathbf{r}_i(t-h) &= \mathbf{r}_i(t) - h \dot{\mathbf{r}}_i(t) + \frac{1}{2} h^2 \ddot{\mathbf{r}}_i(t) - \dots \end{aligned} \quad (3.3)$$

which can be added resulting in, neglecting $\mathcal{O}(h^4)$,

$$\begin{aligned} \mathbf{r}_i(t+h) &= 2\mathbf{r}_i(t) - \mathbf{r}_i(t-h) + h^2 \ddot{\mathbf{r}}_i(t) \\ &= 2\mathbf{r}_i(t) - \mathbf{r}_i(t-h) + h^2 \frac{\mathbf{f}_i(t)}{m_i} \end{aligned} \quad (3.4)$$

This expression is the starting point of the Verlet method. It allows the calculation of the position of a particle at time $t+h$ given the position of the particle at time t and $t-h$, and given the net force acting on the particle at time t . A particle's velocity is determined by the application of Equation 3.1 to the particle's displacement:

$$\mathbf{v}_i(t) = \frac{\mathbf{r}_i(t+h) - \mathbf{r}_i(t-h)}{2h}, \quad (3.5)$$

although this expression is accurate to only $\mathcal{O}(h^2)$.

The Verlet method has several advantages. It is very compact and easy to program, and it conserves energy well, even when long time steps are used [81]. It is also time-reversible; setting h to $-h$ leaves Equation 3.4 unchanged. However, in its original form, the Verlet algorithm contains the undesirable addition of a small term to a difference of two large terms. This problem is remedied by using the ‘leap-frog’ form of the Verlet algorithm.

In the leap-frog scheme, particle displacements play ‘leap-frog’ with particle velocities over half steps in time:

$$\mathbf{v}_i(t + \frac{1}{2}h) = \mathbf{v}_i(t - \frac{1}{2}h) + h \frac{\mathbf{f}_i(t)}{m_i} \quad (3.6)$$

$$\mathbf{r}_i(t + h) = \mathbf{r}_i(t) + h \mathbf{v}_i(t + \frac{1}{2}h). \quad (3.7)$$

That is, given the net force on a particle at time t and its velocity at time $t - \frac{1}{2}h$, the velocity at a half step in the future, $t + \frac{1}{2}h$, is determined using Equation 3.6. Thus, the velocity has skipped or ‘leap-frogged’ the evaluation at the current time t . Using this result and the displacement of the particle at time t , the displacement of the particle a full step in the future can be determined from Equation 3.7. Now the displacement has ‘leaped’ over the intermediate time $t + \frac{1}{2}h$. While both the future and past velocities are at hand, the velocity at time t can be calculated using

$$\mathbf{v}_i(t) = \frac{\mathbf{v}_i(t + \frac{1}{2}h) + \mathbf{v}_i(t - \frac{1}{2}h)}{2}. \quad (3.8)$$

It is clear that this method removes the subtraction of similar large quantities coupled with the addition of small quantities. The original Verlet algorithm can be recovered from this scheme by substituting Equation 3.6 into Equation 3.7 and eliminating $\mathbf{v}_i(t - \frac{1}{2}h)$ using

$$\mathbf{v}_i(t - \frac{1}{2}h) = \frac{\mathbf{r}_i(t) - \mathbf{r}_i(t - h)}{h}. \quad (3.9)$$

3.1.2 Periodic Boundary Conditions

Since the number of particles that can be actually simulated is limited by finite computational resources, the boundary of the simulated volume (the simulation cell) is of great importance. One boundary condition often used in particle simulations to more closely model a macroscopic system with a limited number of particles is the periodic boundary condition. The application of periodic boundary conditions is performed by replicating the simulation cell. This is shown in Figure 3.1. Particles

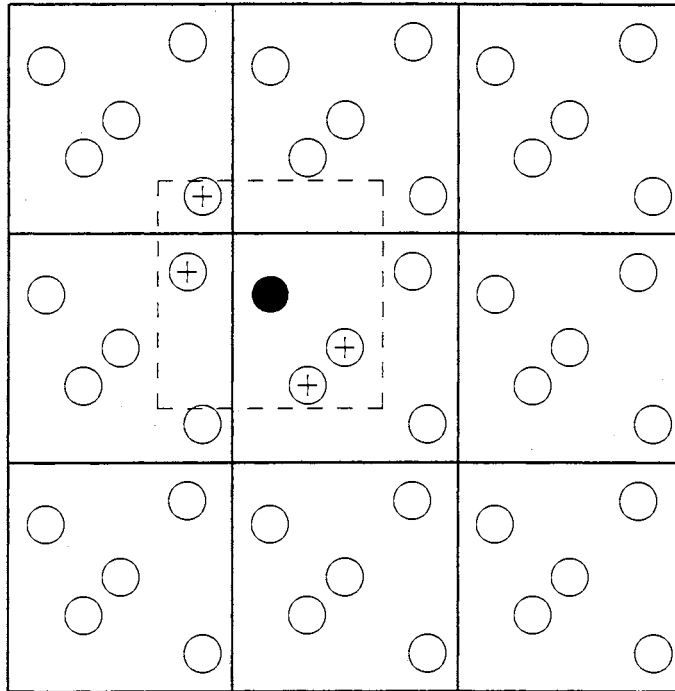


Figure 3.1: Periodic Boundary Conditions. The central cell is the simulation cell and the surrounding eight cells are the periodic images of this cell. When the minimum image convention is applied to darkened particle, only the particles marked with a '+' interact with it. The dashed box has the dimensions of the simulation cell and is centered on the darkened particle.

actually followed in the simulation are in the central cell, while the remaining cells are periodic reflections of the central cell. To avoid unwanted periodicities, the minimum image convention is applied whereby each particle interacts only with the closest images of the the other particles. This is shown in Figure 3.1 where the closest

particle images to the darkened particle are indicated with a '+'. The dashed box centered on this particle has the same dimensions as the simulation cell. Only particles within this box interact with the darkened particle. This technique is easily extended to three dimensions. For example, if a cubic cell is used, it will be surrounded by 26 identical copies: 6 covering the cube faces, 12 filling in the exposed edges and 8 closing off the corners.

Although squares and cubes have been used to illustrate periodic boundary conditions, there are many other choices, although they are not as simple to incorporate. Examples of other three dimensional cells are the truncated octahedron, the rhombic dodecahedron [81], and any parallelepiped. For the remaining discussion, we will assume a cubic simulation cell with cell edge length l . Generalization to other cell shapes is straightforward.

Clearly, the use of minimum image periodic boundary conditions is not equivalent to direct simulation of a macroscopic number of particles. The periodic boundary removes any non-periodic correlations longer than the cell edge (for a cubic cell) and replaces them with perfectly periodic correlations. Any motions or structures that may extend distances greater than the cell edge lengths will be suppressed. This will effect simulations near critical points and phase transitions where long wavelength fluctuations are important [81]. Periodic boundaries can also distort any statistic that depends on long range contributions such as the pair distribution function. In addition, the shape of the periodic cell can distort the dynamics for some systems. For example, a cubic lattice will not conserve angular momentum. This can be seen if one imagines a rotation of the particles about the center of the simulation cell in Figure 3.1. All the images will similarly rotate about their respective cell centers. If the rotation proceeds in a counter-clockwise manner, the relative distance between the solid particle and the image it interacts with in the cell to its left will increase

until this particle crosses the cell border. At this point, it will be reflected across the cell and the distance will decrease as the rotation continues. Thus, the Hamiltonian of the system is not invariant under a rotation of the coordinate system, and the angular momentum will not be conserved.

3.1.3 Potential Truncation and Neighbor Lists

The minimum image convention reduces the number of particle interactions that need to be evaluated by removing the interactions of a particles which fall outside a cell volume centered on either one of them. Thus, the interaction potential should be insignificant at ranges longer than $\frac{1}{2}l$ or else the long range part of the potential should be handled using special long range force techniques [81,86]. For a system of N particles, the number of force evaluations required to include all unique pair interactions is $\frac{1}{2}N(N - 1)$. This limits the number of particles that can be simulated. However, the limitation is mitigated by using truncated potentials and neighbor lists.

By truncating the potential to zero at a cutoff radius r_c , many interactions can be removed. Of course, the interaction must be considered small enough at distance greater than r_c that they can be neglected. Although the use of a cutoff radius reduces the number of interactions that need to be evaluated, the calculation of $\frac{1}{2}N(N - 1)$ distances remain. But, for particles that are separated by a large distance relative to r_c , it is wasteful to check their separation at every iteration since it would likely take many iterations for the particles to move within the cutoff distance of each other. Neighbor lists reduce this waste.

The simplest implementation of a neighbor list is the Verlet neighbor list [81]. This method consists of storing, for each particle, a list of all neighbors within a radius r_n . Then, when the time comes to determine the interactions of a particle, only particles in the list contribute. Of course, r_n must be greater than r_c . Indeed, for this scheme to

work, r_n must be large enough that any particle outside another's neighbor list cannot cross the space between the spheres of radius r_n and r_c before the list is updated. The period between revisions of the neighbor lists is determined by r_n . The larger r_n , the less frequently the lists need to be updated. But, as r_n increases, the number of particles in the lists grows, increasing the number of distance evaluations and the amount of memory necessary to hold the lists. The optimal value of r_n will depend on the system being studied since the number and computational cost of evaluations will vary. The update of the neighbor list can also be done automatically when any particle crosses a distance greater than $(r_n - r_c)$ [81].

Another neighbor list implementation that is more efficient than the Verlet method for large numbers of particles is the cell index method [81,84]. In this method, the simulation cell is divided into smaller sub-cells. Lists of particles in each sub-cell can be quickly determined. Then, interactions are evaluated for a particle with all particles within its sub-cell and particles within the 26 sub-shells which surround it. Since the sorting of particles can be done inexpensively, it is performed at each iteration. The cell index method can be executed easily and efficiently in a data structure called a linked list. Allen and Tildesley [81] and Rapaport [84] both provide example programs in FORTRAN and C, respectively, for implementing linked lists. However, the implementation can be performed in a much simpler manner by the use of structure type variables and variable pointers. (For example, see [87], pages 255–266.)

3.1.4 Application of Constraints

Often in a simulation, it is desirable to incorporate constraints on the system. For example, atomic bonds may be modeled as rigid, constraining bonded atoms to a fixed relative distance, or whole structures may be constrained to form a large rigid body.

Constraints that can be written in terms of the constrained particles' coordinates and time in a form

$$f(\mathbf{r}_1, \mathbf{r}_2, \dots, t) = 0 \quad (3.10)$$

are holonomic constraints [88].

Holonomic constraints may be imposed by several methods. The most elegant method is the use of generalized coordinates producing equations of motion that do not explicitly contain the constraints. However, in application, this method is quite unmanageable for a system of constraints needed to apply rigid bonds to a large flexible molecule such as a lipid. The next possibility is the application of Lagrange undetermined multipliers. This method incorporates the equations of constraint into the equation of motion through the use of new variables (the Lagrange multipliers) extending the system to $3N + N_c$ equations and unknowns where N_c is the number of holonomic constraints [88]. However, when this method is applied in a simulation, the Lagrange multipliers will accumulate integration errors leading to a divergence of bond lengths from their original values.

Ryckaert and co-workers devised a method of including constraints in a simulation that does not produce this accumulation of error [89]. Their method is to include constraints via corrections to the unconstrained equations of motion. For large molecules with many constraints, the SHAKE algorithm [89,81,86,84] is the most suitable application of this method.

The SHAKE algorithm is applied by first moving the particles in time without any constraints applied using Equations 3.6 and 3.7. Then, a correction is made to the unconstrained position. With $\mathbf{r}_{ij} \equiv \mathbf{r}_j - \mathbf{r}_i$, the corrected displacements, indicated with primes, is given by

$$\begin{aligned} \mathbf{r}'_i(t+h) &= \mathbf{r}_i(t+h) - \gamma \frac{\mathbf{r}_{ij}(t)}{m_i} \\ \mathbf{r}'_j(t+h) &= \mathbf{r}_j(t+h) + \gamma \frac{\mathbf{r}_{ij}(t)}{m_j}. \end{aligned} \quad (3.11)$$

The variable γ is determined by solving the holonomic constraint imposed on particles i and j ,

$$\mathbf{r}'_{ij}{}^2 - d_{ij}^2 = 0. \quad (3.12)$$

The result, neglecting $\mathcal{O}(\gamma^2)$ and smaller, is

$$\gamma = \frac{\mathbf{r}'_{ij}{}^2(t+h) - d_{ij}^2}{\left(\frac{1}{m_i} + \frac{1}{m_j}\right) \mathbf{r}_{ij}(t) \cdot \mathbf{r}_{ij}(t+h)}. \quad (3.13)$$

Now, when this correction is made, it may disturb other corrections previously applied to either particle i or j . So, the corrections are made iteratively, performing corrections for all bonded atoms in turn until all rigid bonds are within some given tolerance of the actual bond length.

3.1.5 Constant Temperature and Pressure

The MD algorithm in the previous section follows particle trajectories in the constant particle number, volume and energy (*NVE*) ensemble. (Although, the total energy of the system will fluctuate due to integration errors.) However, it is often desirable to perform the simulation with the temperature, pressure or both, held constant. Several methods have been developed to produce MD simulations in constant temperature and/or pressure ensembles [81,84]. The methods can be classified into four groups: stochastic methods, constraint methods, extended or feedback methods, and scaling methods. Stochastic methods are used to generate constant temperature MD simulations. Although they differ in practical application, they all consist of resetting the particle's velocity to a random value chosen from a Maxwell-Boltzmann distribution having the desired temperature. Constraint methods introduce nonholonomic constraints into the equations of motion that enforce the constancy of the temperature or pressure. Extended methods incorporate the addition of new variables and energy terms to the equations of motion resulting in equations of motion which are constant temperature and volume analogs of the original system.

Scaling methods were used in this study. Developed by Berendsen *et al.* [90], these methods utilize a (non-stochastic) proportional scaling of velocities and coordinates to respectively produce constant temperature and pressure. In the case of constant temperature, the velocities are scaled by a factor

$$\lambda_v = \left[1 + \frac{h}{\tau_T} \left(\frac{T_0}{T} - 1 \right) \right]^{\frac{1}{2}} \quad (3.14)$$

where h still represents the MD time step, τ_T is the temperature coupling constant, T_0 is the desired system temperature, and T is the current (instantaneous) system temperature. The current system temperature is calculated from the kinetic energy

$$T = \frac{2}{(3N - N_c - 3)k_B} \sum_{i=1}^N \frac{1}{2} m_i v_i^2. \quad (3.15)$$

Here, k_B is Boltzmann's constant, N is the number of particles, and N_c is the number of constraints. This scaling is equivalent to adding a temperature dependent friction term to the equations of motion,

$$m_i \ddot{\mathbf{r}}_i = \mathbf{f}_i + m_i \nu(T) \mathbf{v}_i, \quad (3.16)$$

where $\nu(T)$ is the frictional damping constant,

$$\nu(T) = \frac{1}{2\tau_T} \left(\frac{T_0}{T} - 1 \right). \quad (3.17)$$

The imposition of constant pressure is similar. The coordinates are all proportionally scaled by a factor

$$\lambda_x = \left[1 - \frac{h}{\tau_P} (P_0 - P) \right]^{\frac{1}{3}} \quad (3.18)$$

with P_0 representing the desired pressure, P the instantaneous pressure, and τ_P the pressure coupling constant. The instantaneous pressure is calculated from the internal virial,

$$\mathcal{W} = \frac{1}{3} \sum_{i=1}^N \mathbf{r}_i \cdot \mathbf{f}_i, \quad (3.19)$$

by

$$P = \rho k_B T + W/V, \quad (3.20)$$

where ρ is the system density and V is the system volume [81]. The coupling rate constants τ_P and τ_T are determined by trial and error.

This method of simulating systems under constant temperature and pressure has several advantages [90]. First, the coupling to the heat or pressure bath (τ_P and τ_T) is controlled by the researcher and there are no discontinuous changes in particle coordinates or velocities. Also, truncation errors will not accumulate to produce large deviations from the constant values desired. The major disadvantage is that ensemble generated is unknown.¹ Static average properties and dynamic properties of individual particles are not significantly altered, but the fluctuation of global properties, such as pressure, volume, kinetic energy and the velocity autocorrelation function are artificially influenced by this method if coupling constants are made too small [90].

3.1.6 Electrostatic Interactions

Electrostatic interactions must be treated with particular care because of their long range nature [91]. Since the use of periodic boundary conditions requires the use of a cutoff radius, the electrostatic interaction will be truncated. If, say, the oppositely charged atoms of a polar molecule are separated by the cutoff radius for a particular interaction, the net force calculated will be erroneous.

This problem is partially alleviated by using group-based electrostatic cutoffs. Instead of determining electrostatic interactions using a cutoff radius applied to individual atom pairs, the cutoff radius is applied to atom groups. For example, the three atoms of water can be considered a atom group. If any one of the water atoms

¹However, the limiting cases of $\tau_T \rightarrow \infty$ and $\tau_P \rightarrow \infty$ produce adiabatic and isochoric systems, respectively.

is within the electrostatic cutoff radius, all atoms of the molecule are included in the interaction. This procedure can be applied to whole molecules or parts of a molecule.

3.2 Specifics Related to Lipid Bilayers

We now turn our attention from general methods to particular considerations when MD simulations are applied to lipid bilayers. The primary methodological concerns in such systems relate to the handling of equilibration and the choice of ensembles.

3.2.1 Equilibration in Lipid Bilayer Simulations

The structure of lipid bilayers makes the process of equilibration important in a simulation. This is because the simulation averages must be calculated over configurations that are statistically independent of the original configuration. But, the density and anisotropy of bilayers may lead to configurational ‘bottlenecks’ that may require a long simulation to escape. For example, consider a starting configuration determined from X-ray studies of hydrated gel phase bilayers as shown in Figure 2.4 on page 11. These systems have all-*trans* chains which are interdigitated and collectively tilted. As the simulation progresses from this configuration, the disordering of the chains will begin at the chain ends since the middle and upper parts of the chains will be sterically confined to remain in the *trans* conformation. The disordering of the upper parts of these chains may require a significant amount of simulation time.

Of more importance, however, is the fact that different types of structure may require different amounts of equilibration time. Say the chains appear to have taken on the appropriate fraction of *trans-gauche* isomerizations. This does not necessarily indicate that the chain structure is near equilibrium. The original tilt of the chains may still have strong influence on the collective arrangement and packing of the chains. So, appropriate equilibration should be gauged by measuring many different

parameters: kinetic and potential energy, volume, chain order parameters, chain tilt, area per molecule, *etc.*.

3.2.2 Constant Pressure

The choice of ensemble is another important consideration in a lipid bilayer simulation [91]. A common and natural selection is the *NPT* ensemble. This is in part due to the fact that nearly all experimental data is observed at constant temperature and pressure. But, the primary reasons are that the total energy of a lipid bilayer is unknown and the bilayer density is uncertain [57,25].

Constant temperature methods are easily applied to lipid systems, but constant pressure methods require some consideration. A non-zero surface tension is likely to exist in a lipid bilayer producing a pressure tangential to the bilayer surface that is different to the pressure normal to the surface. Although the surface tension is defined as the free energy per surface area, it is not the only term in the differential of the surface free energy dF^σ [92]. This differential is given by,

$$dF^\sigma = -S^\sigma dT - P dV^\sigma + \gamma dA + \sum_i \mu_i^\sigma dn_i^\sigma, \quad (3.21)$$

where S^σ is the surface entropy, V^σ is the surface volume, γ is the surface tension, A is the surface area, μ_i^σ is the chemical potential of the surface's i th component and n_i^σ is the number of the surface's i th component. At equilibrium $dF^\sigma = 0$. But, clearly, this does not imply γ is zero. In particular, assuming that the bilayer volume doesn't change significantly at constant temperature Equation 3.21 becomes,

$$dF^\sigma = \gamma dA + \sum_i \mu_i^\sigma dn_i^\sigma. \quad (3.22)$$

Thus, γ can only be assured to vanish if the number of particles in the membrane do not change. In particular, there must be no transfer of water in or out of the membrane, $dn_w^\sigma = 0$.

Feller and Pastor [93] argue that membrane simulations utilizing periodic boundary conditions must have a change in n_w^σ . Periodic boundary conditions suppress membrane undulations since the edges of the bilayer must match up at the edge of the simulation cell. Because of this enforced ‘flatness’, the bilayer cannot undergo a change in the area without a change in n_w^σ . Water will either enter the bilayer when the area increases or will be squeezed out of the bilayer when the area decreases.

Feller and Pastor estimate γ for cholines by determining the surface tension required to remove undulations [93]. They calculate γ to be 20–50 dynes/cm. Chiu *et al.* estimate γ to be 56 dynes/cm from surface tension studies of lipid monolayers [4].

3.3 Summary of Simulation Method

Now that general aspects of MD methods applied to lipid bilayers has been discussed, we turn to the particular method employed in this simulation study. The material in this section represents primarily the work of See-Wing Chiu and Eric Jakobsson and can be found in [4].

The MD software package GROMOS by van Gunsteren and Berendsen [94] with some modification was used to perform the simulation. This package uses the Verlet Leap-Frog integration algorithm. The SHAKE algorithm was employed to constrain bond-lengths.

The initial system is depicted in Figure 2.4 (page 11) and consists of 100 dimyristoyl phosphatidylcholine (DMPC) molecules, 50 molecules per monolayer, hydrated by 2100 water molecules. There are 10,990 atoms in the system. Periodic boundary conditions in three dimensions were applied. The initial coordinates of the DMPC atoms were determined from X-ray studies of gel phase DMPC [95]. The extended simple point charge (SPC/E) model of water was used [96]. This model represents the water molecule as rigid with van der Waals spheres representing atoms. Point

charges are placed at the atom locations. The charges and van der Waals parameters are determined by fitting simulation data to the proper density and energy of water.

The charge distribution of the DMPC molecule was determined through *ab initio* calculations. The values used are shown in Figure 3.2. The charge indicated is in units of e and are taken to reside at the center of the atom for which the charge is

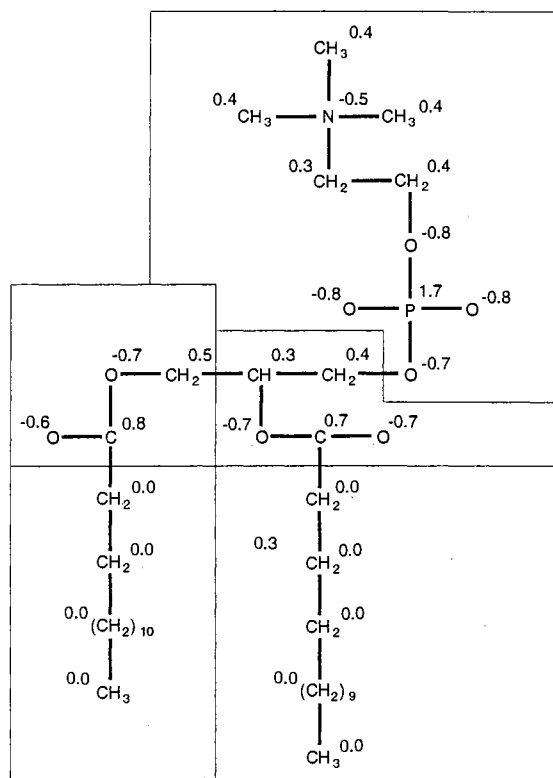


Figure 3.2: Charge distribution and charge groups used in the simulation. The numbers next to each atom indicate the charge, in units of e , used in the simulation. The boxes group the atoms into neutral charge groups.

associated. Group-based cutoffs were used with DMPC having five neutral groups. These groups are separated in Figure 3.2 by the thin lines. The alkane chain dihedral potential was that of Ryckaert and Bellemans [11] shown in Figure 2.3 (page 9). All other interaction parameters were those used by Egberts [97]. This parameter set utilizes the united atom model for CH_3 and CH_2 groups, treating the groups as single van der Waals particles.

Two cutoff radii were utilized. The first radius of 10 Å applied to van der Waals interactions and interactions within this radius were calculated every time step. The second radius of 20 Å applied to the group-based electrostatic interaction and interactions between 10 and 20 Å apart were calculated every 10 time steps. Verlet type neighbor lists were updated every 25 time steps. Each time step was 2 fs.

A constant anisotropic pressure was applied. The pressure normal to the bilayer surface P_{\perp} was set to 1 atm. The pressure tangent to the bilayer surface P_{\parallel} was determined using the definition [4]

$$\gamma = \int_{z_1}^{z_2} [P_{\perp}(z) - P_{\parallel}(z)] dz. \quad (3.23)$$

Here, γ is the surface tension of the bilayer, z indicates the direction normal to the membrane and the interval z_1 – z_2 covers the thickness of the bilayer. With $P_{\perp} = 1$ atm, $\gamma = 56$ dynes/cm and using a bilayer thickness of 55 Å, $P_{\parallel} \sim -100$ atm. The pressure was held constant using the scaling method of Berendsen as discussed in Section 3.1.5 with an initial coupling rate constant τ_P of 0.4 ps. Later, this was increased to 4 ps to reduce short-term fluctuations in volume.

The initial configuration, shown in Figure 2.4 was equilibrated by first gradually heating the initial configuration to 325 K. Then 350 ps of MD was performed. Analysis of the time intervals 80–140 ps and 300–350 ps showed them to quite similar and characteristic of a fluid phase membrane, indicating that the latter intervals were near equilibrium. The system dimensions were found to be changing very slowly over the entire 350 ps simulation, but continuing the simulation until the volume became constant was not feasible given the computational resources. The area change of 1.3 Å² over 210 ps is unlikely to alter the results significantly. The final configuration is shown in Figure 3.3.

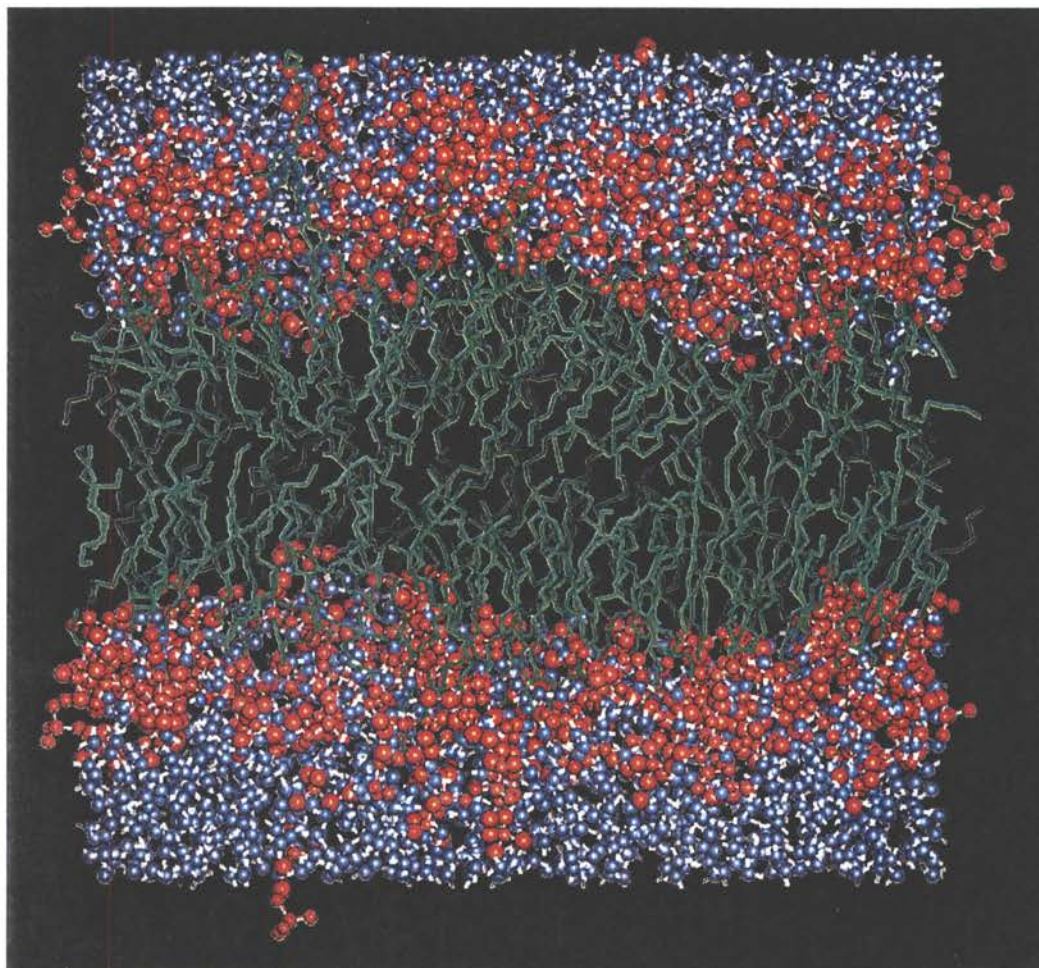


Figure 3.3: Bilayer of 100 dimyristoyl phosphatidylcholine (DMPC) molecules hydrated with 2100 water molecules after heating and 350 ps of molecular dynamics simulation. The DMPC alkane chains are depicted as green sticks while the head-group atoms are depicted as red balls. Water oxygen is colored blue and water hydrogen is colored white.

Chapter 4

Analysis and Results

The analysis discussed in this chapter was performed on trajectories generated utilizing the methods described in the preceding chapter. The method of analysis and results are presented in this chapter. These results are also available in [4]. Unless otherwise noted, the analysis was performed on atom coordinates at intervals of 0.05 ps over the 50 ps interval 300–350 ps (1000 configurations).

4.1 Order Parameters

The average order parameter S_{CD} as discussed in Section 2.2.1 (page 14) was calculated as a function of acyl chain carbon position. This parameter will now be designated S_i where i indicates the carbon position with $i = 1$ representing the chain carbon closest to the the glycerol backbone. Specifically, $i = 1$ indicates the carbonyl carbon (see Figure 2.1, page 6).

The order parameter was calculated from the average

$$S_i = \left\langle \frac{3}{2} \cos^2 \theta_i - \frac{1}{2} \right\rangle \quad (4.1)$$

with θ_i representing the angle made between the i th C-H bond and the bilayer normal. The two chains of the lipid molecule are not equivalent. In Figure 2.1 it is evident that the first C-C bond of the chain on the right is approximately horizontal. The

next bond is then oriented in the roughly vertical position of the rest of the the chain. Since the chains are not equivalent, average order parameter profiles were calculated separately for each. The chains are denoted by the standard nomenclature with $sn-1$ and $sn-2$ representing the chain on the left and right, respectively, in Figure 2.1. S_i was averaged over all atom configurations and over all C-H bonds at position i for of each chain.

Since the simulation utilized the unified atom model for the CH_2 group, the position of the methylene C-H bonds are not specified. They were calculated assuming that the CH_2 group retains its tetrahedral structure. The method used to calculate the $\cos \theta_i$ is described in Figure 4.1. The coordinates of the C atoms are known, so the

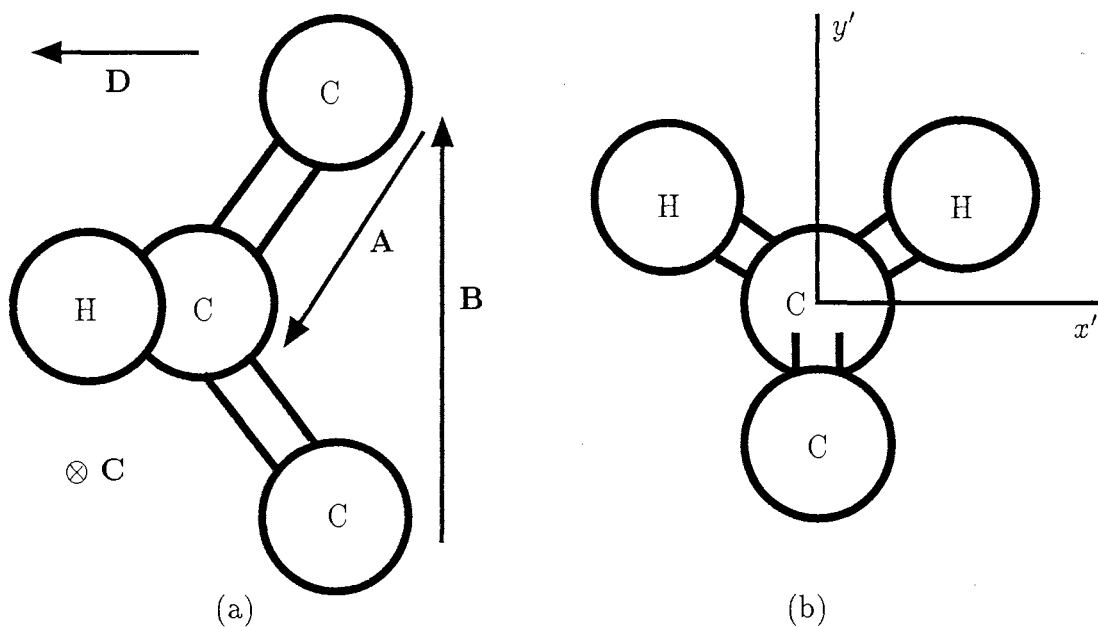


Figure 4.1: Vectors (a) and axes (b) utilized in determining S_i .

vectors **A** and **B** shown in Figure 4.1(a) can be easily calculated. The cross product of these vectors will produce a vector that points into the page and is indicated in Figure 4.1(a) as vector **C**:

$$\mathbf{C} = \mathbf{A} \times \mathbf{B}. \quad (4.2)$$

The vector \mathbf{D} is determined by another cross product,

$$\mathbf{D} = \mathbf{B} \times \mathbf{C}. \quad (4.3)$$

The three vectors \mathbf{C} , \mathbf{D} and \mathbf{B} are orthogonal, and unit vectors in directions parallel to them form an orthonormal basis set,

$$\begin{aligned} \mathbf{e}_{x'} &= \frac{\mathbf{C}}{|\mathbf{C}|}, \\ \mathbf{e}_{y'} &= \frac{\mathbf{D}}{|\mathbf{D}|}, \\ \mathbf{e}_{z'} &= \frac{\mathbf{A}}{|\mathbf{A}|}. \end{aligned} \quad (4.4)$$

The primed vectors form a basis fixed to the CH_2 group. Unprimed subscripts denote basis vectors fixed to the simulation cell. The vectors from the central C atom to the H atoms expressed in terms of the CH_2 basis vectors are known (see Figure 4.1(b)). The orientation of the C-H vectors in the simulation cell basis can be determined by a vector transformation of the C-H vector from the CH_2 basis to the simulation basis,

$$\mathbf{r}_H^{(\text{sim})} = [\mathbf{T}]\mathbf{r}_H^{(\text{CH}_2)} \quad (4.5)$$

where \mathbf{r}_H is a vector from the central C atom to one of the H atoms and the superscript indicates the basis in which the vector is expressed. The transformation matrix $[\mathbf{T}]$ is given by,

$$[\mathbf{T}] = \begin{pmatrix} \mathbf{e}_{x'} \cdot \mathbf{e}_x & \mathbf{e}_{y'} \cdot \mathbf{e}_x & \mathbf{e}_{z'} \cdot \mathbf{e}_x \\ \mathbf{e}_{x'} \cdot \mathbf{e}_y & \mathbf{e}_{y'} \cdot \mathbf{e}_y & \mathbf{e}_{z'} \cdot \mathbf{e}_y \\ \mathbf{e}_{x'} \cdot \mathbf{e}_z & \mathbf{e}_{y'} \cdot \mathbf{e}_z & \mathbf{e}_{z'} \cdot \mathbf{e}_z \end{pmatrix}. \quad (4.6)$$

Once the orientation of the the C-H vectors is known in the simulation cell basis, the order parameter S_i (Equation 4.1) is obtained.

The averaged S_i are shown in Figure 4.2 for the $sn-1$ (dotted line), and $sn-2$ (solid line) chains. The results are in good agreement with experimental data measured by

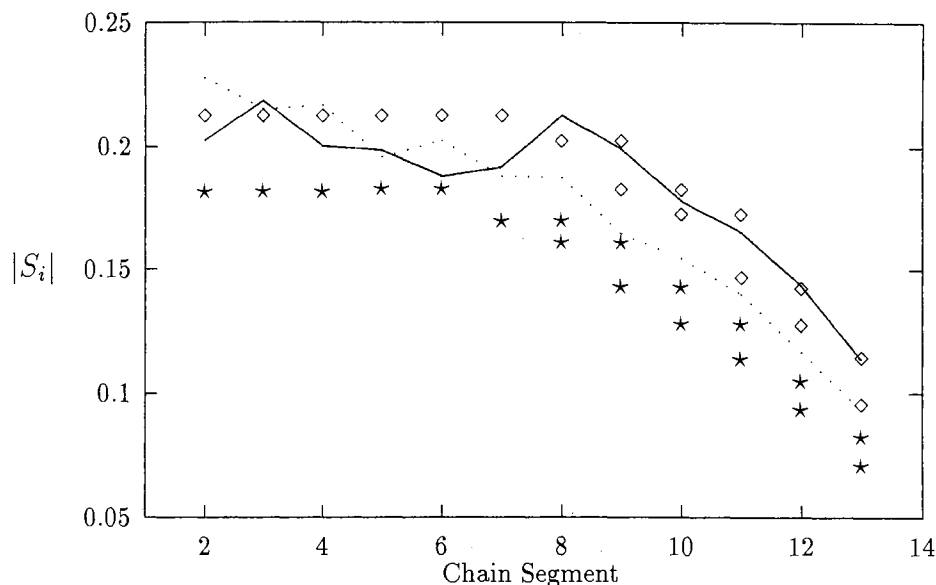


Figure 4.2: Order parameters as a function of carbon position. The dotted and solid lines depict the order parameter $|S_i|$ determined from the simulation for the $sn-1$ and $sn-2$ chains, respectively. The symbols indicate the experimental results of Dodd [98]. The diamonds (\diamond) denote data for DMPC at 303 K and the stars (\star) denote data for DMPC at 323 K.

Dodd [98]. The experimental data were determined from ^2H -NMR measurements on deuterated DMPC at 303 K (\diamond) and 323 K (\star).

The order parameter exhibits a plateau region at the smaller carbon numbers, toward the glycerol backbone, that rapidly falls off for the higher carbon numbers, toward the free ends of the alkane chains. In addition, as in the experimental data the $sn-2$ chain exhibits a slightly larger value of $|S_i|$ than the $sn-1$ chain [98] indicating that the $sn-2$ chain is slightly more ordered than the $sn-1$ chain.

4.2 C-C Dihedral Bond Analysis

The dihedral angle is easily determined from the positions of the four C-atoms which define the dihedral bond. Referring to Figure 4.3, vectors **A**, **B** and **C** are determined

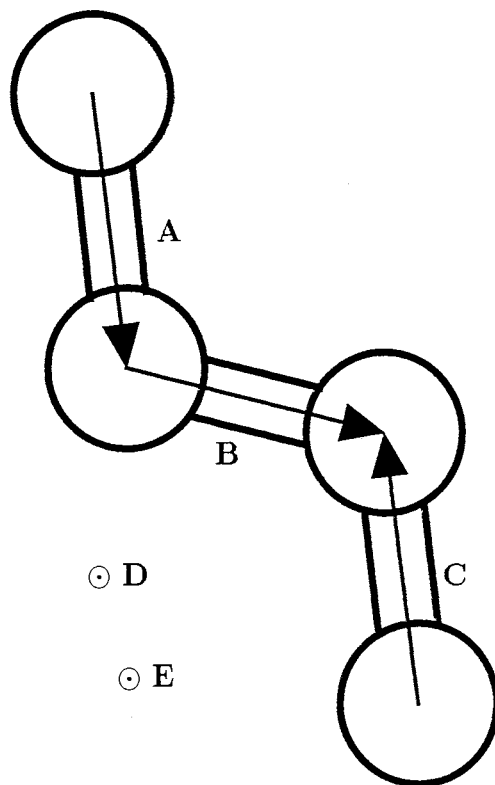


Figure 4.3: Vectors used to determine the angle of dihedral bond.

by the coordinates of the four atoms making up the dihedral. Then, vectors **D** and **E** (which both point out of the page for the bond orientation in Figure 4.3) are determined by taking cross products,

$$\begin{aligned}\mathbf{D} &= \mathbf{A} \times \mathbf{B}, \\ \mathbf{E} &= \mathbf{B} \times \mathbf{C}.\end{aligned}\tag{4.7}$$

The cosine of the dihedral angle ϕ is then found using a vector dot product,

$$\cos \phi = \frac{\mathbf{D} \cdot \mathbf{E}}{|\mathbf{D}| |\mathbf{E}|}.\tag{4.8}$$

The angle is then found by taking the inverse cosine and correcting the result to the proper quadrant (the returned angle from the inverse cosine function is always given in the range $0-\pi$ radians).

Using the method above, all the dihedral angles can be determined. Their prob-

ability density can be determined by forming a histogram of the resulting angles and normalizing the results. Furthermore, angles can be classified into *trans* (t) and *gauche* (g) states by

$$\phi \equiv \begin{cases} t & \text{if } -\frac{\pi}{3} \leq \phi \leq \frac{\pi}{3} \\ g^+ & \text{if } -\pi < \phi < -\frac{\pi}{3} \\ g^- & \text{if } \frac{\pi}{3} < \phi < \pi \end{cases} . \quad (4.9)$$

The probability distribution of chain dihedral angles is given in Figure 4.4(a). The solid line shows the distribution calculated from the averaging the dihedral angle over all chain dihedral bonds, and the dotted line shows the distribution of an isolated dihedral at the same temperature (325 K). Note that the simulated distribution has a larger number of *trans* bonds than the isolated distribution. This reduction in the number of *gauche* rotations is due to the excluded volume effects of neighboring lipid molecules.

Figure 4.4(b) shows the distribution of *gauche* and *trans* bonds as a function of time. The *trans* state (thin solid line) and the total fraction of *gauche* states (thin dotted line) are seen to be stable over the time interval with a t/g ratio of ~ 3 . However, there is a slight drift of the g^+/g^- ratio from ~ 1.2 toward unity.

Table 4.1 summarizes the averages of various chain conformers determined by experiment [23,20] and calculated from the simulation. The experimental data was taken from samples of dilauroyl phosphatidylcholine (DLPC, a 12-carbon chain lecithin) and dipalmitoyl phosphatidylcholine (DPPC, a 16-carbon chain lecithin) in the liquid crystal phases. The simulation and experimental results agree for the number of gg conformers per chain, although the number of end g conformers is underestimated by the simulation. The number of gtg' and $gtg' + gtg$ is more significantly underestimated by the simulation (primes indicate opposite *gauche* rotations relative to unprimed *gauche* states). However, the estimation of these three-bond conformers is experimentally problematic both in the determination of the adsorption band and

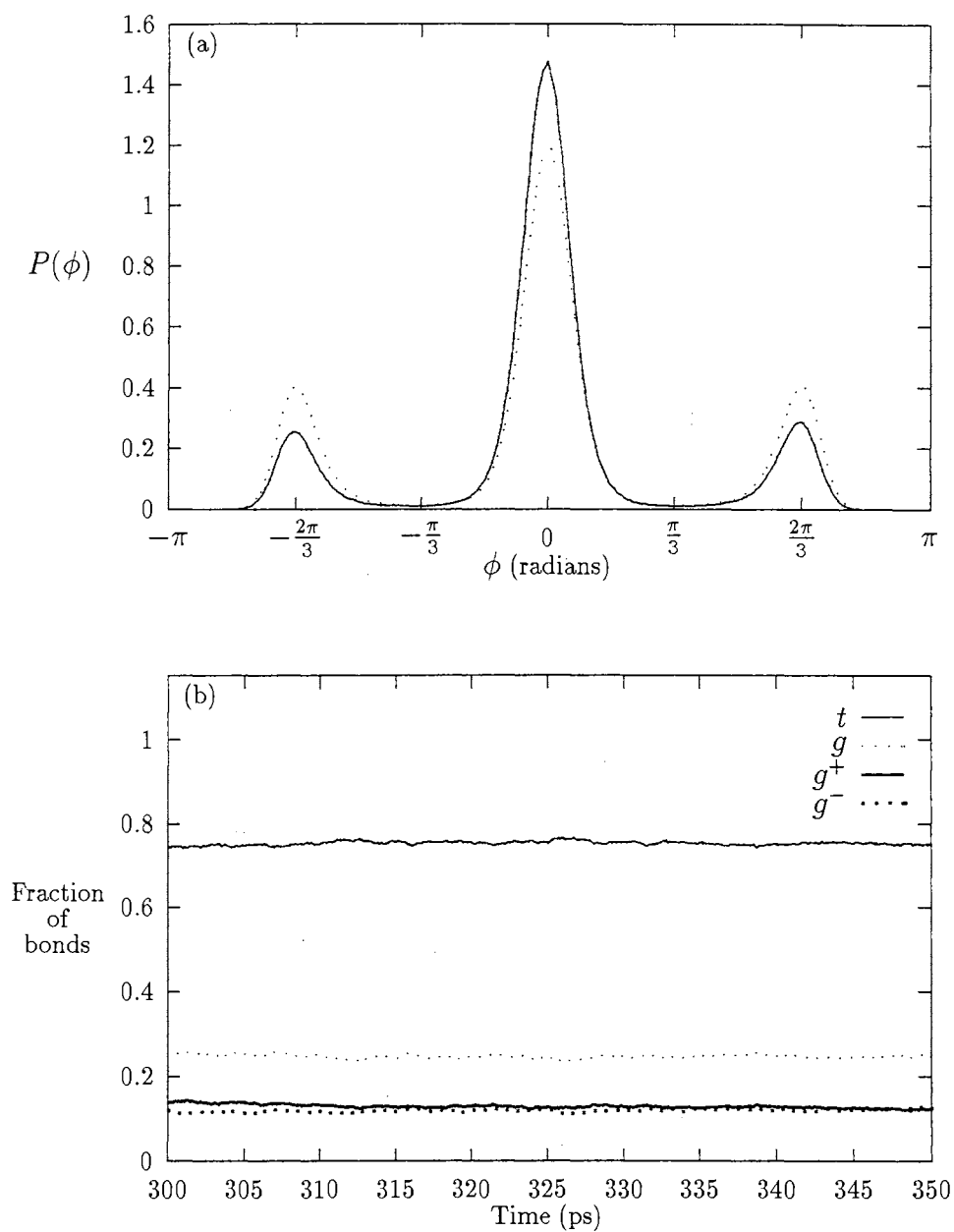


Figure 4.4: Dihedral bond distribution and *trans/gauche* fractions. (a) The probability density $P(\phi)$ of the dihedral bond angle ϕ is shown calculated from the simulation (solid line) and for a isolated dihedral (dotted line). (b) Fractions of *trans* and *gauche* bonds as functions of time.

Conformer	Experimental			Simulation
	DLPC	DPPC ¹	DPPC ²	DMPC
end g	0.45	0.54	0.40	0.31
gg	0.32	0.40	0.40	0.34
gtg'	0.88	1.19		0.39
$gtg' + gtg$			1.00	0.67

Table 4.1: *Trans-gauche* conformers per chain. *Trans* bonds are represented by t and *gauche* bonds are represented by g . A prime on a *gauche* bond indicates an opposite rotation to any unprimed *gauche* in the sequence. Experimental data for DLPC and DPPC¹ were taken from [23], and data for DPPC² were taken from [20]

in the comparison to liquid alkanes [17].

4.3 Atom Distributions and Electron Density

The atom distribution across the bilayer is calculated by making histograms of atom totals at positions along an axis normal to the bilayer surface for the various atom species for each set of atom configurations. These distributions are then averaged and normalized to unity. The resulting atom probability densities are shown in Figures 4.5.

The electron density is calculated in a similar manner to the atom distribution. Histograms are made of atom numbers along the bilayer normal for each atom configuration. However, in this case each atom is weighted by its atomic number. These distributions are averaged and normalized to unity resulting in the probability density shown in Figure 4.6.

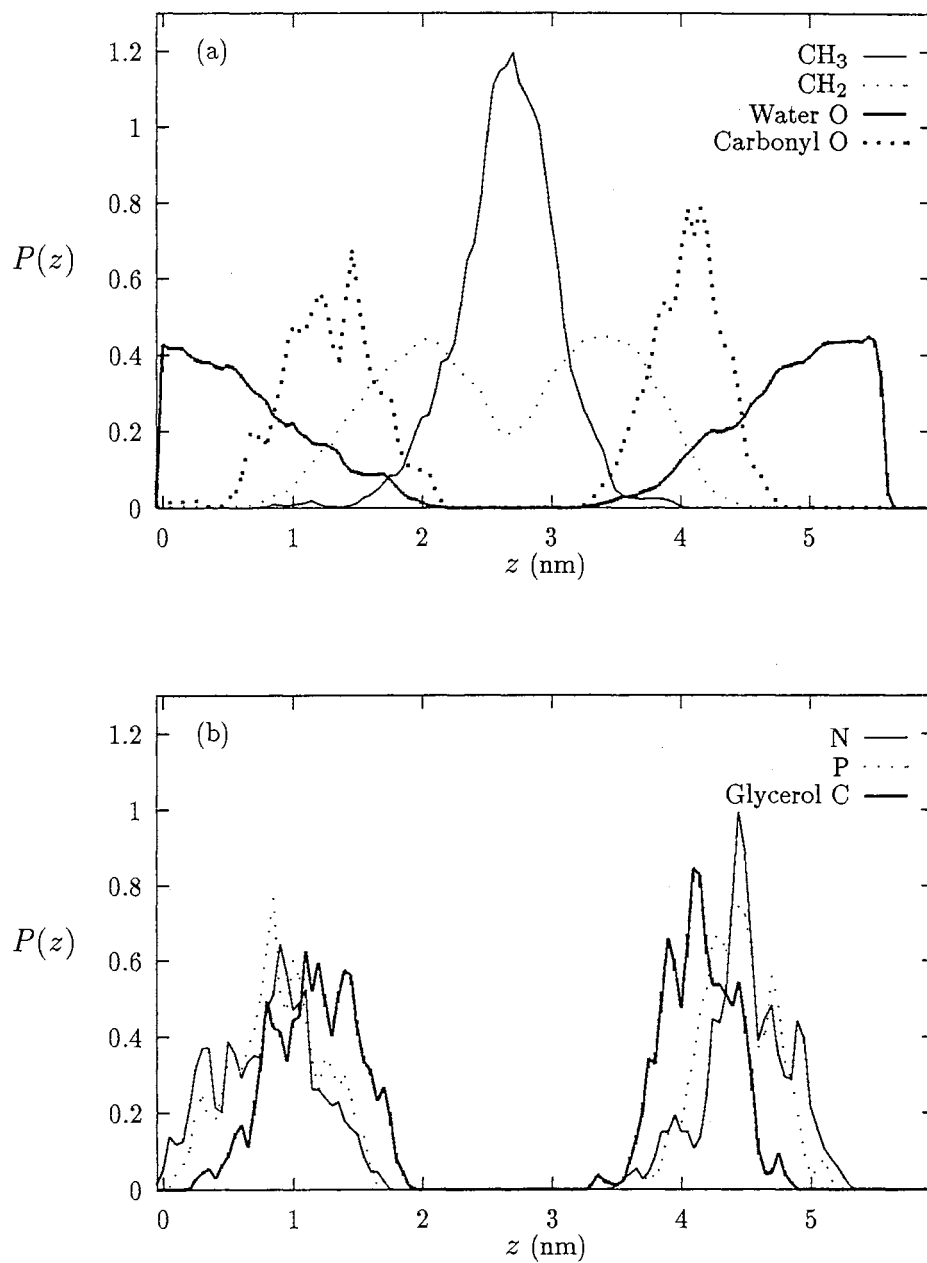


Figure 4.5: Various atom probability densities $P(z)$ as functions of position along the bilayer normal z .

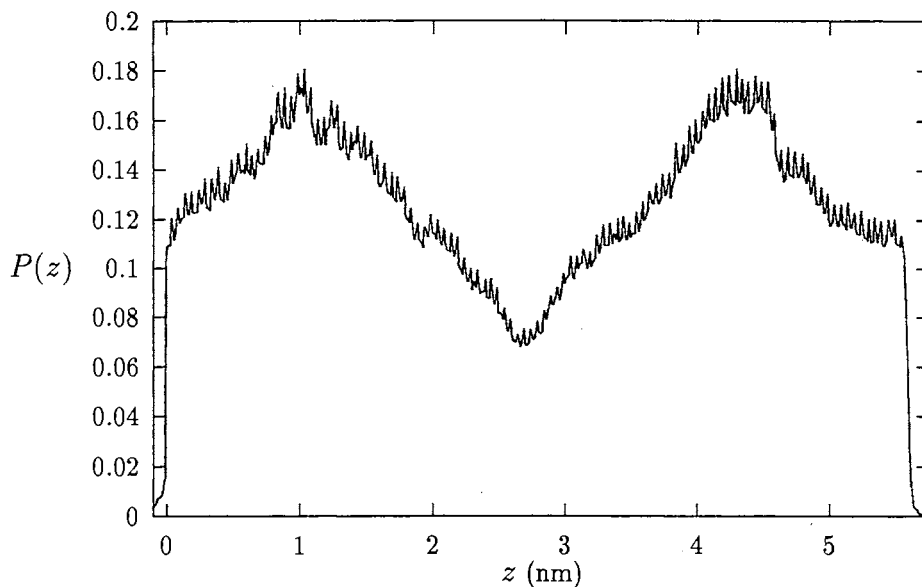


Figure 4.6: Electron probability density P as a function of position along the bilayer normal z .

4.4 Water Dynamics

The behavior of the water/lipid interface is of particular interest since there are few experimental methods of examining this interface at the atomic scale. To this end, we calculated the mean square displacement (MSD) and diffusion constant D of water as functions of position along the membrane normal z . In addition, the contributions to $D(z)$ from motion in each of the cartesian directions were determined as a function of position along the bilayer normal.

The MSD is defined as

$$\text{MSD}(\tau) = \langle |\mathbf{r}(t + \tau) - \mathbf{r}(t)|^2 \rangle, \quad (4.10)$$

with t representing time, τ representing the time interval in which the particle travels and \mathbf{r} indicating the particle's position. Selected results are shown in Figure 4.7. In this figure, the MSD is shown for five different positions along the bilayer normal at increments of 0.5 nm. The slope of each MSD curve is proportional to the diffusion constant, at that level in the bilayer. A linear least squares fit was made to the MSD

curves to calculate $D(z)$. Since the data for $\tau < 10$ ps was nonlinear and data for $\tau > 40$ ps was noisy due to poor sampling, the least squares fit was performed only on the interval ($10 \text{ ps} < \tau < 40 \text{ ps}$) shown in Figure 4.7. From the figure, it is clear that the slope (and thus D) decreases with increasing penetration into the bilayer.

The diffusion constant is determined by the relation

$$D(z) = \frac{1}{2\tau d} \text{MSD}(\tau, z) \quad (4.11)$$

where d indicates the dimensionality of the motion. The $\text{MSD}(\tau, z)$ was calculated for the total displacement ($d = 3$) and for each cartesian direction ($d = 1$) with the z -axis lying along the bilayer normal. Using a linear least squares fit, $D(z)$ was then determined for these four cases. The results are shown in Figure 4.8. Of particular note is the fact that water furthest from the interface is seen to diffuse anisotropically. Diffusion normal to the bilayer is suppressed while diffusion in the plane of the bilayer is enhanced. The diffusion constant for bulk water was calculated for the water model used in the simulation [4] and it is indicated by the horizontal line in Figure 4.8. The anisotropy of the water motion exterior to the bilayer indicates the the system is not fully hydrated. Within the bilayer, the diffusion constant drops rapidly and the anisotropy diminishes due to the reduction of the mean free path caused by the relatively immobile lipid molecules.

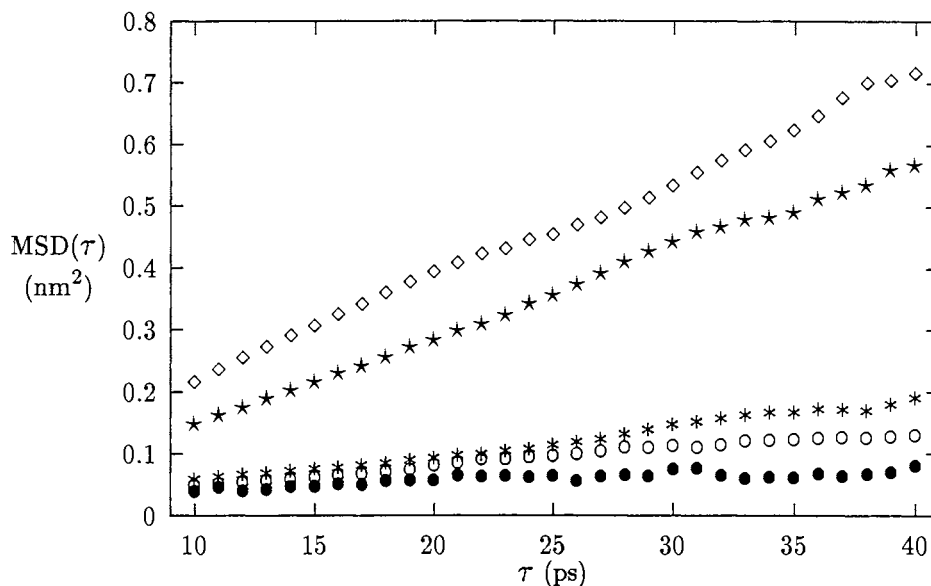


Figure 4.7: Mean square displacement $\text{MSD}(\tau, z)$ as a function of position along the bilayer normal z . Diamonds (\diamond) denote $z = 1.0$ nm, stars (\star) denote $z = 1.5$ nm, asterisks (\ast) denote $z = 2.0$ nm, open circles (\circ) denote $z = 2.5$ nm and solid circles (\bullet) denote $z = 3.0$ nm.

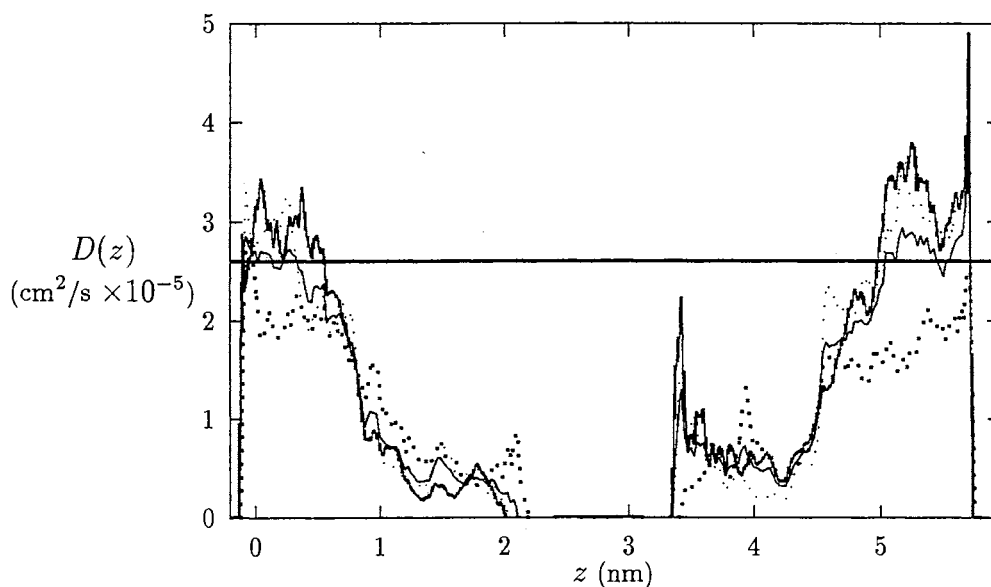


Figure 4.8: Diffusion constant $D(z)$ as a function of position along the bilayer normal z for water. The light solid line denotes the three-dimensional diffusion constant. The light dotted, heavy solid and heavy dotted lines denote the one-dimensional diffusion constant for motion in the x -, y - and z -directions, respectively. The heavy horizontal line displays the diffusion constant of bulk water calculated utilizing the same water model as used in the simulation [4].

Chapter 5

Lipid Ripple Phase

As discussed in Section 2, phosphatidylcholine (PC) bilayers exhibit a ripple phase in which the bilayer surface is uniaxially corrugated with a correlation length on the order of tenths of microns [99]. This chapter describes an effort to construct a lattice model that describes the ripple phase and gel→ripple→liquid crystal phase transitions. The effort utilized configurational-bias Monte Carlo (CBMC) methods to calculate a finite set of lattice site energy states. The results indicate that the energy states of the specified states exhibit large uncertainties relative to their differences, suggesting that the model requires expansion.

5.1 Introduction

The ripple phase has been studied experimentally most recently by X-ray spectroscopy [100-102] and scanning tunnelling microscopy[103,99]. In the following subsection these data will be reviewed. Several different theoretical approaches have attempted to elucidate the phenomena focusing primarily on determining the underlying cause of the undulating structure. These will be summarized in the second subsection. In Section 5.2 the proposed model for the gel→ripple→liquid crystal phases will be described. Section 5.3 describes the CBMC method used, and Section 5.4 gives the results.

5.1.1 Experimental Knowledge

The ripple phase is known to exist between the gel and liquid crystal phases for certain bilayer PC systems at sufficient water concentration. The threshold water concentration is $\sim 20\%$ by volume, at which point the ripple wavelength decreases with increasing water concentration until excess water concentration is reached at $\sim 35\%$ by volume [101]. Over this range of water concentrations, the ripple wavelength of dimyristoyl phosphatidylcholine (DMPC) bilayers decreases from 15.94 nm to 12.31 nm [101].

Although the ripple wavelength has been found to be invariant with temperature [99], the ripple amplitude has recently been seen to increase from near zero to 2.4 nm over the ripple phase temperature range of DMPC (14–24 °C) [99]. The ripple waveform is not a simple trigonometric or triangular function [104] and is likely to be asymmetric [102].

The chemical makeup of the lipid molecule is important to the formation of the ripple structure. The chains of the lipids are known to be mostly all-*trans* [101] although recently there is some suggestion that one side of the ripple is more liquid-like than the other [102]. The ripple wavelength and amplitude increase with chain length [104]. The headgroup composition is critically important. If a single CH₃ group is removed from the choline group (N⁺(CH₃)₃) (see Figure 2.1, page 6) and replaced with a single hydrogen atom, the ripple phase does not appear [104].

5.1.2 Theoretical Approaches

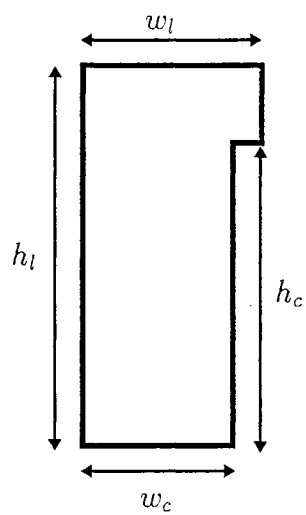
There are two general approaches to theoretical modeling of the ripple phase: phenomenological models and microscopic models. The phenomenological models begin with a postulated free energy functional depending on thermodynamic variables which define the transition and attempt to extract information using classical ther-

modynamic methods; microscopic models begin with a microscopic Hamiltonian and then apply methods of statistical mechanics to determine the system's thermodynamic properties. The summary of previous theoretical work given below is based primarily on the review by Scott and McCullough [104].

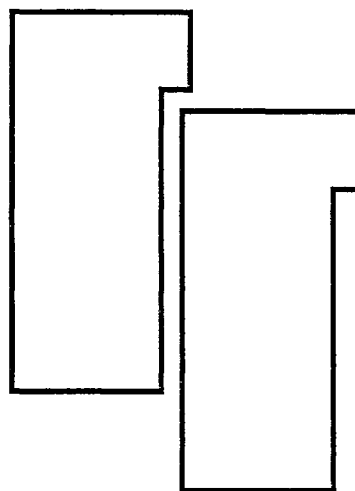
Phenomenological models for phase transitions are based on the original theory of Landau [105]. In this theory, a free energy functional is postulated that utilizes a reduced variable (the order parameter) whose value continually varies from unity to zero as the system undergoes a phase transition. This functional is then expanded in terms of the order parameter and minimized. In the case of ripple phase studies, the Landau approach has utilized order parameters based on bilayer thickness and local bilayer curvature [104]. In both cases the free energy minimization process produced modulated phases. There are difficulties, however. For example, there is no experimental evidence supporting the assumption that bilayer thickness is the driving variable in the ripple phase transition. The lipid chains are nearly all-*trans* as in the gel phase, and no clear mechanism for changes in bilayer thickness has been observed [104]. Generally, the phenomenological method suffers from the fact that a single order parameter is unlikely to describe the variety of processes that take place in the ripple phase transition [104].

The microscopic approach involves constructing a Hamiltonian that describes the microscopic interactions between lipid atoms or molecules. Such a Hamiltonian must be simple if it is to be tractable. Such a model was proposed by Pearce and Scott [106] and subsequently expanded and analyzed [107-110].

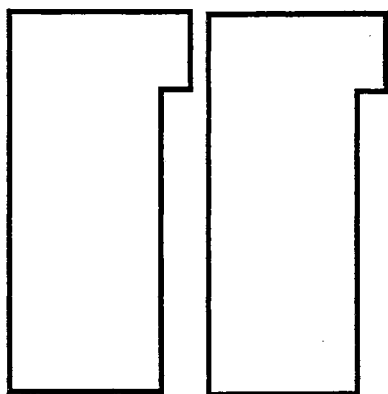
This model views DMPC as a rigid 'L' shaped block, as shown in Figure 5.1(a) [106]. The model Hamiltonian utilized two integer state variables denoting vertical displacement (in $\sim 5 \text{ \AA}$ intervals) and orientation (left or right) of the L-blocks [108]. Energy parameters were determined by calculating molecular interaction energies



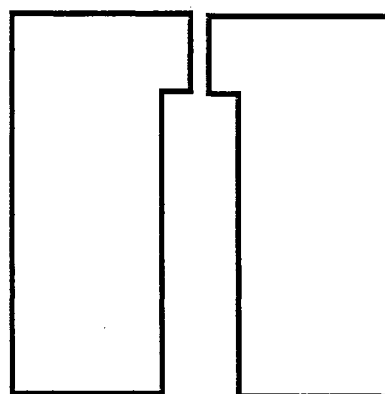
(a)



(b)



(c)



(d)

Figure 5.1: Block models used by Scott and co-workers [106]. (a) Dimensions of lipid block: $h_l \sim 25 \text{ \AA}$, $h_c \sim 20 \text{ \AA}$, $w_l \sim 12 \text{ \AA}$ and $w_c \sim 10 \text{ \AA}$. (b-d) Some possible two lipid orientations.

between two DMPC lipid molecules at various values of the state variables using optimized van der Waals potentials for the atom interactions [108]. This enabled a determination of energy values for various lipid-lipid configurations such as those shown in Figures 5.1(b-d).

Several variations of this model produced a gel phase ground state energy as shown in Figure 5.2(a) and a modulated phase phase at higher temperature as caricatured in Figure 5.2(b). In addition, the model was successful in reproducing observed behavior

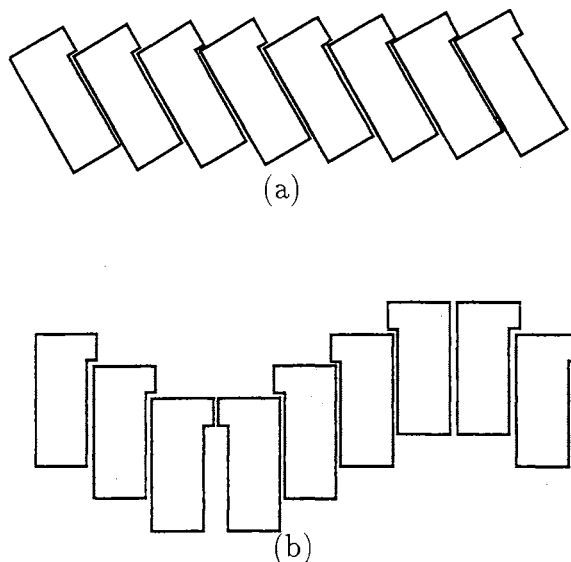


Figure 5.2: Ripple model profiles showing L-block representation of the gel (a) and ripple (b) phases.

when cholesterol is added to DMPC membranes [109]. However, the model cannot reproduce the asymmetric profiles observed by Sun *et al.* [102] or the combination of temperature invariant wavelengths and temperature dependent amplitudes observed by Woodward and Zasazinski [99]. Furthermore, the model cannot describe the ripple to liquid crystal phase transition since the rigid L-blocks do not allow for the melting of the lipid chains.

5.2 Model

The model of Scott and co-workers was expanded in this study in an attempt to include the ripple to liquid crystal phase transition. This section details the model.

As in the original model, the lipid molecules are thought of as block shaped objects. But here the chains have two possible states, rigid (ordered) or flexible (disordered). Molecules with rigid chains take on the shape of the original model as shown in Figure 5.1(a). Disordered chains take up more volume, so that molecules with disordered chains expand laterally to assume rectangular profiles.

Ideally, the Hamiltonian of the original model could be simply extended in this manner by adding another spin variable whose value (0 or 1, say) indicates whether the molecule has ordered or disordered chains. However, this leads to 40 unique pair energy states. This number is too large for practical use in a lattice model, so the model was simplified by only allowing lipid chains to be disordered if the chains are not confined by having another lipid “tucked under” it. Using this criterion and ignoring interactions perpendicular to the ripple axis, the number of pair energy states is reduced to fifteen. These energy states are shown in Table 5.1.

5.2.1 Calculation of State Energies

Energy values of the states shown in Table 5.1 were calculated using the same atom potentials as utilized in the molecular dynamics study discussed in the previous chapters including use of the Ryckaert-Belleman's dihedral potential shown in Figure 2.3 on page 9. The energy calculation includes interactions between each atom of one lipid matched with each atom of the other lipid and each chain atom with the all other atoms of the lipid to which it belongs.

For a pair of rigid molecules, this interaction energy is straightforward to calculate, but the calculation becomes complicated when one or both of the lipids are in

State Number	Lipid Orientation	Chains of Left Lipid	Chains of Right Lipid
1		disordered	disordered
2		disordered	ordered
3		disordered	disordered
4		disordered	disordered
5		ordered	disordered
6		ordered	ordered
7		ordered	disordered
8		ordered	ordered
9		disordered	disordered
10		disordered	ordered
11		ordered	disordered
12		disordered	disordered
13		ordered	ordered
14		ordered	disordered
15		disordered	ordered

Table 5.1: State identification numbers are shown for the fifteen ripple model states.

disordered states for two reasons. First, the number of possible chain conformations is huge requiring that a statistical sampling be made. But, second, the sampling of a chain's configurations is complicated by the volume restriction due to the other chains of the lipid pair and the surrounding molecules, modeled as shown in Figure 5.3.

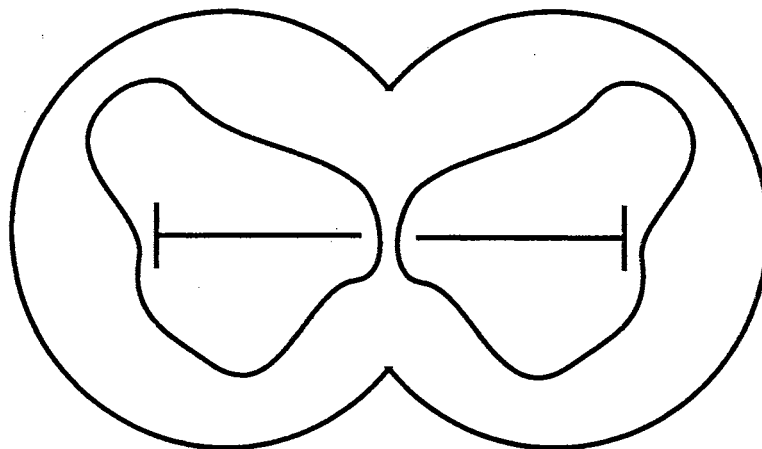


Figure 5.3: Top view of a pair of lipid molecules surrounded by a hard wall. The wall is located by placing a hard cylinder centered on each lipid and then removing the intersecting arcs. The 'T' shapes indicate the lipid orientation with the cross of the 'T' indicating the 'chain' side of an L-block model and the stem of the 'T' indicating the ripple axis.

Traditional Metropolis Monte Carlo methods [2] are very inefficient at sampling systems such as lipid molecules. When a trial dihedral rotation is made along a lipid chain, the segment of the chain below the rotated bond will be displaced greatly and will likely overlap atoms of another chain or the enclosing wall. This situation leads to very small acceptance rates for Metropolis methods applied to dense chain systems. However, a recent Monte Carlo method, known as configurational-bias Monte Carlo (CBMC) [73-77], has been developed that is particularly suited to the simulation of dense chain systems [74,75,77-80]. This method was used to sample the disordered chain configurations in this study and is described in the next section.

The calculation of the state energies followed these steps:

1. The minimum energy position near the appropriate lipid pair configuration was

determined using rigid molecules. The purpose in this step is to eliminate any large energies that may be due to poor placing of the molecules.

2. The energy contribution due to rigid atoms is calculated. Rigid atoms include all head group atoms and the chain atoms of any ordered lipid molecules. For a given displacement between molecules, this energy does not change.
3. The interaction energy of the flexible chains with all other atoms is calculated using CBMC methods. This step is iterated many times before the next step is taken.
4. For each state, entire molecules are displaced using Metropolis MC methods at zero temperature. As in step 1, this is to help ensure the lipid molecule pairs are at or near minimum energy states due to their relative displacement.
5. Steps 2–4 are repeated. Over a simulation, over twenty-thousand CBMC moves are performed on each flexible chain of each state.

The above modeling efforts were carried out for several different values of the temperature and the effective headgroup charges.

Since water was not explicitly included in the calculation, the dielectric effect of water was modeled by reducing the charge on the headgroup atoms. This is certainly an approximation for a calculation of atomic interactions since the water dipoles will not produce a continuous dielectric constant at this resolution. A charge reduction of one half was used in the final calculations.

Ideally, a microscopic model should not contain any temperature dependent terms. However, the CBMC sampling of the disordered chain configurations in step 3 is temperature dependent. Several values of temperature were used providing a set of state energies as a function of temperature.

The results of these calculations are presented in Section 5.4, but first we digress to discuss the CBMC method.

5.3 Configurational-Bias Monte Carlo

As its name implies, the CBMC method samples a system with a sampling bias based on the system configuration. The biased sampling procedure generates configurations that are energetically more favorable than those generated by methods such as those due to Metropolis. The description of the method that follows is taken from several sources [73-76]. References [75] and [76] contain particularly lucid discussions of the method and a notation similar to that of reference [76] will be used.

The sampling procedure consists of regrowing a selected chain of atoms, picking the position of each atom based on that atom's environment. The chain of atoms need not be an actual bonded chain, rather, the 'chain' is a collection of sequentially redistributed atoms. However, the method is particularly well suited to bonded molecular chains, and the discussion below will be in terms of the application to chains.

Consider the addition of the i th chain segment (attachment of the i th atom) to a chain producing a conformation of the chain $\mathbf{\Gamma}$. The potential energy of the attachment can be separated into two contributions. The first contribution $\mathcal{V}_{\text{int}}^{(i)}(\mathbf{\Gamma})$ is the 'internal' potential energy. This is the potential due to the bond itself. For the hydrocarbon chains of a lipid molecule, this contribution is the dihedral potential of Figure 2.3 on page 9. The second energy contribution $\mathcal{V}_{\text{ext}}^{(i)}(\mathbf{\Gamma})$ is the 'external' contribution. It represents the potential due to nonbonded interactions experienced by the segment. Note, both $\mathcal{V}_{\text{int}}^{(i)}(\mathbf{\Gamma})$ and $\mathcal{V}_{\text{ext}}^{(i)}(\mathbf{\Gamma})$ include the contribution of energy due to the previously grown $i - 1$ atoms of the chain but not the $i + 1$ to ℓ atoms yet to be added where ℓ is the total number of segments in the chain. That is, the total

potential energy of a chain segment in conformation Γ is given by

$$\mathcal{V}_{\Gamma} = \sum_{i=1}^{\ell} \left(\mathcal{V}_{\text{int}}^{(i)}(\Gamma) + \mathcal{V}_{\text{ext}}^{(i)}(\Gamma) \right). \quad (5.1)$$

With the separation of potentials into internal and external contributions, the i th segment is attached in two steps. First, b trial positions are generated for the i th segment. These orientations are selected based a Boltzmann distribution of the internal energy of the segment. For example, in our case, the internal potential is the dihedral potential, $\mathcal{V}_{\text{int}}^{(i)}(\Gamma) = \mathcal{V}_{\text{dihedral}}(\theta_i)$. Thus, b angles are randomly generated from the distribution

$$P_{\text{int}}(\theta) = \frac{\exp(-\beta \mathcal{V}_{\text{dihedral}}(\theta))}{\int_0^{2\pi} \exp(-\beta \mathcal{V}_{\text{dihedral}}(\theta)) d\theta}, \quad (5.2)$$

where $\beta = 1/(k_B T)$ with k_B representing the Boltzmann constant and T representing the temperature of the system. Next, one of the b trial orientations is randomly selected based on the Boltzmann weighting of it's external potential energy. That is, segment orientation j is selected with probability

$$P_{\text{ext}}(j) = \frac{\exp(-\beta \mathcal{V}_{\text{ext}}^{(i)}(j))}{Z_i}, \quad (5.3)$$

where

$$Z_i = \sum_{k=1}^b \exp(-\beta \mathcal{V}_{\text{ext}}^{(i)}(k)). \quad (5.4)$$

Segment i is added to the chain with the chosen orientation, and the process is repeated for the remaining segments.

This biased growth algorithm can be incorporated into a Monte Carlo selection scheme to generate unbiased equilibrium configurations from the constant particle, volume, and temperature (NVT) ensemble. This scheme proceeds as follows:

1. Randomly pick a chain and regrow it using the method described above. Its configuration before the regrowth (the 'old' configuration) is denoted Γ_o , and the new trial configuration is denoted Γ_t .

2. For each growth step, calculate the Rosenbluth weight of the selection,

$$w_i^{(t)} = Z_i/b. \quad (5.5)$$

This is a weight reflecting the bias of the selection of segment i and is named in honor of Rosenbluth and Rosenbluth who developed an early precursor to the CBMC method [111].

3. For each growth step, calculate the ‘old’ Rosenbluth weight. That is, determine the bias required to select the original conformation j' of the i th segment. To satisfy detailed balance, this weight must be based on the same set of b segments used in step 1. The ‘old’ weight $w_i^{(o)}$ is determined in the same manner as $w_i^{(t)}$ except the contributions of the b trial conformations to $w_i^{(o)}$ are evaluated in the environment seen by the i th segment of the original chain, and conformation j' is substituted for j :

$$w_i^{(o)} = \frac{\exp(-\beta\mathcal{V}_{\text{ext}}^{(o)}(j')) + \sum_{k \neq j'}^b \exp(-\beta\mathcal{V}_{\text{ext}}^{(o)}(k))}{b}. \quad (5.6)$$

4. The trial chain is accepted with probability $\min(w_t/w_o, 1)$ where $w_t = \prod_{k=1}^{\ell} w_k^{(t)}$ and $w_o = \prod_{k=1}^{\ell} w_k^{(o)}$. If accepted, the trial chain replaces the old chain, if rejected, the old chain is taken as the selected chain.

The last step ensures that microscopic reversibility is maintained. That is, the probability of a transition $\Gamma_o \rightarrow \Gamma_t$ is equal to the reverse transition $\Gamma_t \rightarrow \Gamma_o$. Microscopic reversibility (detailed balance) is a sufficient condition to ensure that the sampling scheme produces configurations from the NVT ensemble of states [81]. To see that microscopic reversibility is indeed maintained, consider the probability density to select a particular trial conformation j , from a specific set of b orientations,

at location i along the chain,

$$P_i(j) = P_{\text{int}}(j) \left[\prod_{k \neq j}^b P_{\text{int}}(k) \right] P_{\text{ext}}(j). \quad (5.7)$$

Here, the prefactor is the probability density that conformation j is selected as one of the b orientations. The second factor (the product series) is the probability that the particular set of $b - 1$ other trial conformations are chosen, and the last factor is the probability that conformation j is chosen out of the b possible conformations. The probability to generate the original chain, is identical except in the set of b trial conformations, the original conformation j' of segment i , is substituted for the chosen trial orientation j . The probability to generate a whole chain is given by a product of the segment probabilities,

$$P_{\Gamma} = \prod_{i=1}^{\ell} P_i(j_i). \quad (5.8)$$

Detailed balance requires the transition probability from state j to j' should be equal to the transition probability from state j' to j ,

$$K_{jj'} = K_{j'j}. \quad (5.9)$$

But, there may be a very large number of sets of b configurations containing j or j' . For this reason, a 'super-detailed balance' condition is applied such that for any specific set of b orientations, detailed balance holds [75,76].

We assume, without loss of generality, that $w_i^{(t)} < w_i^{(o)}$. This means that the probability to accept the transition $j' \rightarrow j$ is $w_i^{(t)}/w_i^{(o)}$ (for the whole chain, w_t/w_o is used) while the probability to accept the transition $j \rightarrow j'$ is 1. Then,

$$\begin{aligned} K_{j'j} &= N_{j'} P_i(j) \left(w_i^{(t)}/w_i^{(o)} \right), \\ K_{jj'} &= N_j P_i(j'), \end{aligned} \quad (5.10)$$

with N_j indicating the number of segments in configuration j . Using Equations 5.4–

5.7, we have

$$\begin{aligned}
 P_i(j)w_i^{(t)} &= cN_j \prod_{k \neq j}^b P_{\text{int}}(k), \\
 P_i(j')w_i^{(o)} &= cN_{j'} \prod_{k \neq j}^b P_{\text{int}}(k),
 \end{aligned}
 \tag{5.11}$$

where c is a constant. Substituting into Equation 5.10 produces the desired equality,

$$K_{jj'} = K_{j'j} = \frac{cN_j N_{j'}}{w_i^{(o)}} \prod_{k \neq j}^b P_{\text{int}}(k).
 \tag{5.12}$$

The CBMC method, thus generates chain conformations appropriately sampled from the NVT ensemble but chosen using a bias to make ‘acceptable’ configurations more likely to be generated. This increases the efficiency of the sampling tremendously since overlapping of chains is unlikely under the CBMC scheme. In addition, the method makes relatively large steps through configuration space as it samples the chain configurations since each accepted trial chain is a complete rearrangement of the original chain.

5.4 Results & Discussion

Calculations were performed for all states using temperature values of 200, 240, 280, 300 and 340 degrees Kelvin. During these runs, the CBMC acceptance rates varied widely from state to state lying in a range of 0.18–16%. The average value ranged from 5.2% to 7.9% for the lowest and highest temperatures, respectively. These acceptance rates, while lower than the usual 50% desired, are substantially higher than traditional Monte Carlo methods produce for dense chain systems. A typical disordered configuration is shown in Figures 5.4.

Although the CBMC method worked quite well in the calculation of the energy states, the resulting energy values maintained rather large fluctuations in the CBMC calculations. The result was that the difference in energy between many of the average

energies determined for different states was smaller than the standard deviations. For example, Figure 5.5 shows the values of the energy determined at 340 K with error bars indicating a standard deviation above and below the value. Clearly, many of the states overlap. This situation also occurred for the calculations at the other temperatures studied. The standard deviation was calculated over an extended calculation for each temperature and found not to vary indicating the standard deviation calculated was not due to a lack of proper equilibration. Since ordering of the energies was to be resolved, the current model cannot be used to study phase transitions.

The inclusion of additional states is not likely to improve the model. An increase in the number of pair states will not remove the large standard deviations of the the states already selected. Use of three- or four-lipid states might narrow the standard deviation, but would increase the number of states beyond practical use.

One possible remedy for the large standard deviations in the calculated energy states is a refining of the boundary enclosing the two lipids. The hard wall may allow more widely varying energy states than would exist if a more realistic boundary were imposed. For example, one could surround the chain region of the lipid pair with lipid chains which also undergo CBMC rearrangement. This may narrow the energy range sampled by the CBMC rearrangement of the lipid pair. This is especially likely if the pair interaction includes the interaction energy with the bounding chains, in which case, conformations which produce large energy contributions between the lipid pair may be offset by low energy contributions from the boundary chains.

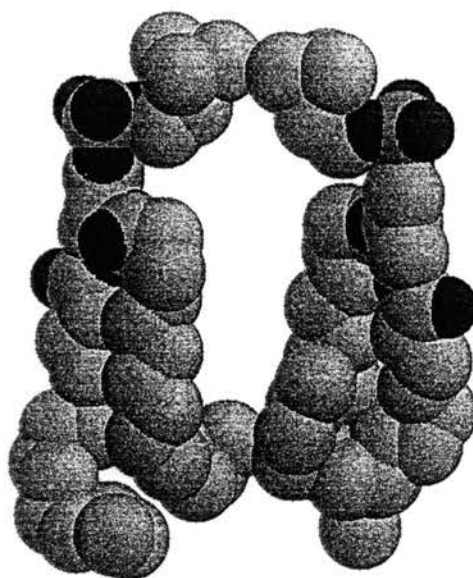


Figure 5.4: Typical disordered lipid pair configuration. The figure corresponds to state 3 in Table 5.1 at 340 K.

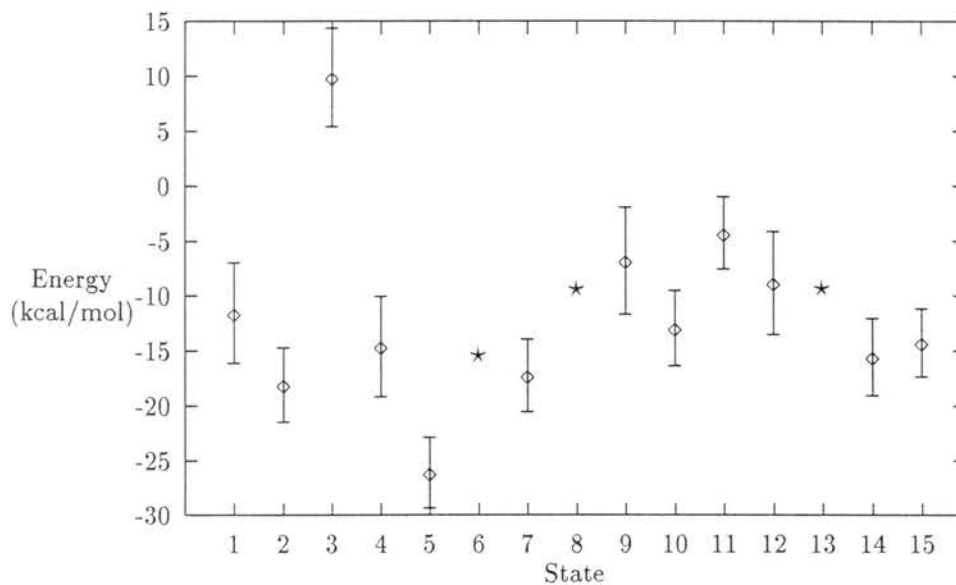


Figure 5.5: Energy of ripple model states at 340 K. Error bars indicate \pm one standard deviation for states requiring CBMC simulation for determination. These state are indicated with diamonds (\diamond). The stars (\star) indicate energy states that consist of two rigid molecules, and thus do not require CBMC simulation to determine.

Part II

Hybrid Monte Carlo Method Applied to Diamond

Chapter 6

Introduction

The molecular dynamics (MD) simulation described in Chapters 3–4 cover a duration of a few hundred picoseconds. In some applications, this is too short to obtain meaningful results. In the remaining chapters of this thesis, a method is described by which simulations of longer time scales may be achieved.

Finite computational resources limit the system size and the real time through which a simulation may be propagated. As systems under investigation become more complex, these limitations become more acute. Gas-surface and condensed phase systems are examples. In such systems, the interaction potential is often a complex function containing many-body, highly directional terms. The computation time required for the repeated evaluation of such a potential and its derivatives currently precludes (MD) simulations over periods of time on the order of nanoseconds or greater.

Kinetic Monte Carlo procedures (KMC) provide an alternative methodology [112–117]. In a KMC simulation, derivatives of the potential energy need not be calculated providing an immediate advantage over MD methods. In addition, KMC methods may utilize simpler models to generate motion as a function of time. For example, most KMC simulations to date have been based on models in which the underlying crystalline symmetry of the solid to be grown is ‘built-in’ [116,117]. In these cases, the use of a simple set of growth rules and/or a grid to restrict atom moves or

hops greatly reduces the computational cost of the simulation. The adequacy of the built-in growth rules and underlying grid are tested by comparing the results of the simulations with experimental data, which is possible since the simulations can produce large-scale film growth. However in these simulations, the pre-existence of an underlying grid precludes obtaining any fundamental insights into the microscopic mechanisms by which a given interatomic potential leads to growth of a crystalline phase. In order to obtain insights at this level, alternative simulations are required which are not lattice based (off-lattice), and which employ realistic (and often very complex) intermolecular potential surfaces. Yet, these simulations must run for at least milliseconds of real time in order to allow surface clusters to form and interact.

An important consideration for any dynamical simulation is the time scale of the events to be studied. If the events in question occur on vastly different time scales, it is generally impossible to simulate the process using the standard KMC and MD methods. For MD simulations, high-frequency motions will determine the integration time step that must be employed. If this time step is extremely small, it will be impossible to adequately sample the low-frequency events in an acceptable amount of computational time. In KMC calculations, the events with the largest rates will completely dominate the simulation, and events with small occurrence probabilities will be rare. In some cases, this problem can be solved by ignoring the fastest motions. In an MD simulation, this may be done by the use of a restraint. For example, the high frequency motion of atomic bonds are often removed by constraining the atoms to a rigid bond. Also, if the high frequency motions can be integrated analytically, Tuckerman *et al.* [118] have shown that an MD simulation can utilize the exact solution as part of a longer time-step algorithm. This allows for inclusion of both long and short time scales in an MD simulation. However, its use is presently limited to systems where the high frequency motions are sufficiently simple to allow for analytic

solution of these motions [118]. In a KMC simulation, the high frequency events can often be removed from the model altogether so that all events in a KMC study will have probabilities that are of the same order of magnitude.

For some systems, it is important to include explicit consideration of both fast and slow processes. Surface growth in a chemical vapor deposition (CVD) experiment may involve fast surface equilibration dynamics between deposition events which often occur on time scales several orders of magnitude longer than the equilibration steps. Yet, both of these events must be accurately treated in the simulation if the results are to be useful in the interpretation of experimental data.

A hybrid MC method designed to handle problems created by critical processes occurring on vastly different time scales is presented in this part of the thesis. This method uses KMC techniques to handle the dynamics for the rate determining steps and equilibrium MC methods for the fast relaxation steps. The method allows the computation of trajectories up to hundredths of a second in length, extremely long for a dynamic simulation. In the next chapter, the hybrid MC method is presented in more detail. In Chapter 8, the hybrid method is applied to an off-lattice simulation of diamond growth by CVD. Chapter 9 presents and discusses the results of the simulations. The material in this part is also reported in references [5] and [6].

Chapter 7

Hybrid Monte Carlo Method

The need to simulate the growth of diamond film over large times has led to the use of a hybrid Monte Carlo method that uses Kinetic Monte Carlo (KMC) to perform the long time motions while Metropolis Monte Carlo (MMC) methods are used to simulate the fast time motions. This chapter describes this hybrid simulation method.

7.1 Equilibrium Monte Carlo Method

The Monte Carlo method devised by Metropolis *et al.* [2] is one of the most commonly used simulation methods. In its original form, it generates states in the constant particle number, volume and temperature (*NVT*) ensemble.

The practical implementation of the MMC method is as follows:

1. Choose a particle (or cluster of particles) and randomly displace it, producing a trial position. This displacement can be performed by nearly any means, but the simplest is a small linear displacement of the particle such that

$$\begin{aligned}x_t &= x_o + \alpha\xi_x \\y_t &= y_o + \alpha\xi_y \\z_t &= z_o + \alpha\xi_z\end{aligned}\tag{7.1}$$

where x , y and z are the cartesian coordinates of the particle with the subscripts

indicating trial (t) and original (o) values, α is a constant defining the maximum displacement of the particle and ξ_x , ξ_y and ξ_z are random numbers uniformly distributed between -1 and 1 .

2. Calculate the potential energy change $\Delta\mathcal{V} = \mathcal{V}_t - \mathcal{V}_o$ between the initial configuration and this new trial configuration.
3. If $\Delta\mathcal{V} < 0$, accept the move. If $\Delta\mathcal{V} \geq 0$, accept the move with probability $\exp(-\beta \Delta\mathcal{V})$ with $\beta = 1/(k_B T)$, k_B being the Boltzmann constant. Accepting a move means to take the next configuration in our ensemble sampling to be the trial configuration generated by step 1; rejecting a move means to take the original configuration (before the particle was displaced) as the next configuration.

This algorithm satisfies detailed balance and will thus generate ensembles from the NVT ensemble [81]. That is, the MMC method satisfies

$$K_{ij} = K_{ji} \tag{7.2}$$

where K_{ij} is the probability of transition from state i to state j . This is shown in a manner similar to that used in Section 5.3 (page 67). Assuming that $\Delta\mathcal{V} > 0$, the transition probabilities generated by the method are

$$\begin{aligned} K_{ij} &= N_i P_j \exp(-\beta \Delta\mathcal{V}) \\ K_{ji} &= N_j P_i. \end{aligned} \tag{7.3}$$

Here, N_i is the number of systems in state i , and P_i is the probability that state i is generated. Now,

$$\begin{aligned} P_i \exp(-\beta \mathcal{V}_i) &= c N_i \\ P_j \exp(-\beta \mathcal{V}_j) &= c N_j, \end{aligned} \tag{7.4}$$

where c is a constant. Using these two expressions, it follows that the MMC method satisfies detailed balance and is thus assured to generate states from the NVT ensemble,

$$K_{ij} = K_{ji} = \frac{cN_iN_j}{\exp(-\beta\mathcal{V}_i)}. \quad (7.5)$$

7.2 Kinetic Monte Carlo Method

Unlike molecular dynamics (MD) simulations, Monte Carlo (MC) methods do not explicitly propagate the system through time. The motion of the particles in MC studies is quasi-random rather than deterministic. However, the states generated by traditional MC methods [2,119-121] are correlated in that they are generated sequentially from similar configurations. At present, there is no known sampling method that does not give correlated configurations that is computationally practical [112]. However, if the correlations can be interpreted as dynamical correlations in a stochastic description of the system, they work to our advantage [122]. That is, a kinetic interpretation of MC methods implies that the states simulate the real motion of the system rather than being just a sampling of ensemble states. Expectation values can then be calculated as time averages.

The probability density $\rho(\mathbf{x}_m, t)$ that a certain configuration \mathbf{x}_m occurs at a time t is described by the Markovian master equation [113]:

$$\frac{d\rho(\mathbf{x}_m, t)}{dt} = \sum_n W_{nm}\rho(\mathbf{x}_n, t) - \sum_n W_{mn}\rho(\mathbf{x}_m, t), \quad (7.6)$$

where W_{mn} is the transition rate from state m to state n and \mathbf{x}_m is a $3N$ -dimensional vector representing the total configuration of a system of N particles. KMC methods are viewed as algorithms which numerically solve Equation 7.6 by properly choosing from the various transitions and accepting or rejecting the move with the appropriate probability [115]. The time scale is incorporated in the calculations through the

transition rates. These rates must be determined *a priori* (by phenomenological arguments, experiment, and/or MD simulations, for example). However the rates are determined, care must be exercised to ensure that Equation 7.6 gives a zero time rate of change of $\rho(\mathbf{x}_m)$ when \mathbf{x}_m is in an equilibrium state, or the simulation will not generate equilibrium behavior. This is most easily and commonly done by choosing transition rates such that detailed balance is satisfied [115].

For very simple potentials, MC steps can be viewed as being proportional to time, but for even modestly complex potentials, Kang and Weinberg have shown by direct simulations that this is not the case [114]. Fichthorn and Weinberg have shown that time can be formally linked to a particular KMC event when the event is a Poisson process [115]. In this case, the interevent time can be randomly determined from an exponential distribution. Since it is the key to the hybrid method employed, the Fichthorn and Weinberg argument is summarized below.

Let r_i be the transition rate for event i . An example might be the adsorption of a particle on a surface. If this transition can be cast as a Poisson process, then the probability that k independent events will occur in time t is given by

$$P(k) = \frac{(r_i t)^k}{k!} e^{-r_i t}. \quad (7.7)$$

The expectation value of k for this distribution is

$$\langle k \rangle = r_i t. \quad (7.8)$$

Thus, r_i is the average occurrence rate of the process. If there are different types of events with rates r_a and r_b , then the total number of events that occur in time t (of both kinds) is also described by a Poisson distribution with a total rate $r_T = r_a + r_b$ [115,123]. It therefore follows that

$$P(k = k_a + k_b) = \frac{(r_a + r_b)^k}{k!} e^{-(r_a + r_b)}. \quad (7.9)$$

In general, the total rate for the entire system to change is given by

$$R = \sum_i r_i. \quad (7.10)$$

If events are governed by a Poisson distribution with rate R , the probability density of the interevent time is given by [115,123]

$$P(t) = Re^{-Rt}. \quad (7.11)$$

Thus, if the system under study can be cast as a set of independent events with known rates, the time between events has an exponential distribution which can be sampled to determine the time taken for an event to occur.

Fichthorn and Weinberg [115] have provided an excellent example of the utilization of this method for the case of atom adsorption and desorption on a surface and Binder [112] lists several additional algorithms, although he does not explicitly cast them in terms of Poisson processes. Fichthorn and Weinberg have also pointed out that utilization of Poisson processes is valid for non-equilibrium MC simulations as long as the rates that have been chosen satisfy a “dynamical hierarchy” [115]. That is, every possible event must have a specific rate depending upon the transition process itself. Since the Metropolis algorithm [2] accepts all moves to lower energy states regardless of the transition process, it does not provide this hierarchy. Consequently a Metropolis MC move cannot be interpreted dynamically as a process that simulates random motion in time.

7.3 Hybrid Monte Carlo Method

KMC methods can be used to simulate a system of particles interacting by a set of physical processes as a function of time if the rates of the processes are known. However, if these rates vary greatly, the KMC method is very impractical. This can

be seen from Equation 7.9. If $r_a \gg r_b$, then $P(k_a + k_b)$ approaches $P(k_a)$. That is, essentially all events will be of type a . Furthermore, the time scale for sampled events will be very small since r_a is large. The conclusion is clear—widely varying events cannot be performed in a KMC simulation because the fast processes will completely dominate the simulation. However, if the difference in event rates is large enough, both fast and slow processes can be incorporated into a hybrid equilibrium/kinetic Monte Carlo method.

If the high frequency processes are fast enough to equilibrate over the time required for a low frequency processes to occur, then the fast events can be simulated using the traditional equilibrium Monte Carlo methods while the slow motions are carried out using KMC. Thus for systems consisting of events that occur on widely varying time scales, a single iteration of the hybrid method consists of two steps:

1. Equilibrate the high frequency processes. Any method of equilibration suited to the system may be used in this step.
2. Perform a KMC step based on the low frequency processes. This is the time determining step and may be carried out using any number of low frequency events as long as their rates are comparable. There are several different algorithms available for performing this step [115,112,117].

The specific implementation of these steps will vary according to the system being studied. In the following chapter, the hybrid Monte Carlo method will be applied to a study of diamond film growth via chemical vapor deposition.

Chapter 8

Diamond Film Growth

The hybrid simulation method presented in the previous chapter was applied to a model of diamond film production by chemical vapor deposition (CVD) of methyl radical, CH_3 . The kinetic Monte Carlo (KMC) method was used to propagate the system in time based on the (relatively) low frequency adsorption of CH_3 , and the Metropolis Monte Carlo (MMC) method was used to equilibrate the high frequency lattice relaxation processes.

8.1 Chemical Vapor Deposition of Diamond

8.1.1 Experimental Knowledge

There is currently a large number of experimental methods for growing diamond and diamond-like films of widely varying quality by CVD methods [124-126]. In all of these methods, a hydrocarbon gas is directed onto a substrate subsequent to having been energized in some fashion. If the surface temperature is properly controlled, the result is the formation of diamond film on the substrate. Growth rates up to $150 \mu\text{m}/\text{h}$ using a C_2H_2 flame have been reported [127-130]. High quality diamond particles about $10 \mu\text{m}$ in size have been grown in 20 h of deposition of CH_3 and atomic hydrogen [131]. Nuclear magnetic resonance [132] and electron paramagnetic resonance [133]

experiments have provided new quantitative insights into the internal crystallinity of diamond films grown from filament-assisted CH_3 and H bombardment of a substrate. These data indicate that there is relatively little atomic hydrogen or trapped CH_3 in the film. The majority of the defects appear to be dangling bonds. Direct observation of films by scanning microscopy [134,135] and atomic force microscopy [136] show that the film surface is rough on an atomic scale, while on a larger scale, planar structures 25–50 Å in size and with $\{111\}$ orientation are visible in some cases [134,136]. This suggests a surface correlation length on the order of a few angstroms.

8.1.2 Theoretical Model

Despite the large amount of experimental knowledge regarding diamond CVD, theoretical understanding of the mechanisms underlying the growth process is incomplete. Several elementary-reaction mechanisms have been proposed [137-143]. Of interest to us is the suggestion that CH_3 is the primary growth species on a $\{111\}$ surface [131,144-147]. For our initial simulations, we have chosen to concentrate on the basic elements of diamond CVD that are required to describe the physical system—the chemical constituents of the gas phase, CH_3 and H, and the substrate surface, the $\{111\}$ diamond plane.

The choice of the interaction potential is critical in any simulation. A many-body, semi-empirical potential developed by Brenner [148] is used here. This potential is an extension of Tersoff’s covalent-bonding potential [149] parameterized to fit a very large set of hydrocarbon interactions. It has been successfully employed in a variety of hydrocarbon molecular dynamics (MD) and Monte Carlo (MC) simulations [117,150-156]. The corrections to Tersoff’s potential introduce many-body terms which involve up to third neighbor interactions. Consequently, the Brenner potential is very demanding of computational time making long-term, large scale MD

calculations impractical. Such a system therefore must be studied using the hybrid method.

A KMC calculation requires that the time scales for the events to be considered be obtained from experiment or from a separate theoretical study. Rate coefficients for CH_3 adsorption, hydrogen adsorption and hydrogen abstraction have been computed by Raff and co-workers [157,158] using MD and variational transition-state methods with the Brenner potential and parameter set #1 [148]. Using gas flow rates reported by Goodwin [145] we calculate the following overall event rates at $T = 1250$ K:

- hydrogen abstraction [158]: $2.0 \times 10^8 \text{ s}^{-1}$,
- hydrogen adsorption [157]: $3.7 \times 10^9 \text{ s}^{-1}$,
- CH_3 adsorption on a ledge [157]: $5.5 \times 10^4 \text{ s}^{-1}$, and
- CH_3 adsorption on a terrace [158]: $1.25 \times 10^4 \text{ s}^{-1}$.

The term ‘terrace’ indicates a site at which the dangling bond is oriented in the $\{111\}$ direction of the lattice (normal to the growth surface). All other sites are designated as ‘ledge’ sites.

The most important feature of the above rates is that the CH_3 adsorption rate is four to five orders of magnitude slower than the hydrogen adsorption or abstraction rates. Thus, if both H and CH_3 events were utilized in a KMC method, on average, 10^4 H events would take place between each CH_3 adsorption. This fact makes the inclusion of the hydrogen adsorption and desorption events in a KMC simulation of film growth impractical.

Nevertheless, the hydrogen processes must be included in the simulation since the distribution of radical sites and, therefore, the possible adsorption sites for CH_3 are determined by these events. A similar but more extreme example of this problem is that of off-lattice surface relaxation, including desorption and surface diffusion. The

CH_3 adsorption rate and the hydrogen rates are both orders of magnitude slower than the local atomic motions which occur on time scales of picoseconds. Since we are describing off-lattice simulations, structural rearrangements via local atomic translational motion and rotation about C-C bonds are required to form diamond on the surface. But this type of relaxation cannot be simply incorporated into the KMC method by utilizing the rates of various relaxation events, even if they were explicitly known, because such moves would completely dominate any calculation to the exclusion of actual film deposition moves.

In practice, the large difference in event rates allows us to circumvent the problems described above by the application of the hybrid MC method. Since the surface relaxation and hydrogen adsorption/desorption are much faster than CH_3 chemisorption, the system will reach equilibrium with respect to surface off-lattice relaxation and chemisorption/desorption of hydrogen between CH_3 events. Therefore, the KMC calculations can proceed based solely on CH_3 events while surface relaxation and hydrogen processes can be simulated using any convenient method.

The model system to which we have applied our KMC procedure consists initially of a diamond $\{111\}$ substrate. The substrate is three layers thick with hydrogen capping the vertical dangling carbon bonds at the interface. Figure 8.1 shows an initially bare diamond $\{111\}$ surface measuring after a single CH_3 adsorption. Hydrogen atoms fill all non-radical sites. Radical sites are marked in yellow, carbon of the original bare substrate is grey, and adsorbed carbon is red. Only the first substrate layer is shown for clarity. In an actual diamond film growth experiment, radical sites are created when a hydrogen atom is abstracted from the surface by gaseous hydrogen. Each radical site is a possible location for chemisorption of CH_3 . As more CH_3 is deposited, the number of radical sites also grows. The appropriate equilibrium distribution of radical sites is determined by the ratio of hydrogen atom adsorption to

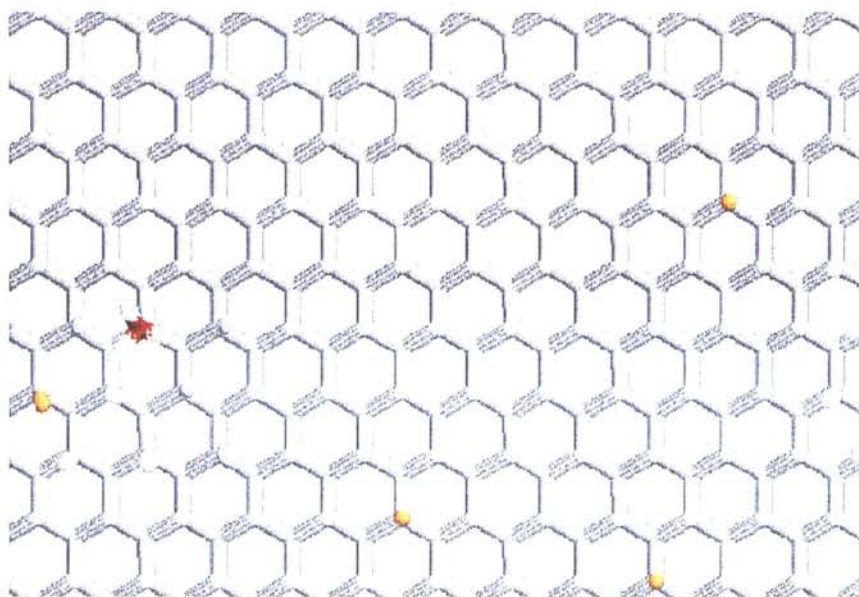


Figure 8.1: The topmost diamond $\{111\}$ surface after the deposition of a single methyl radical. Radical sites are colored yellow, hydrogens are white, substrate carbons are grey and adsorbed carbons are red.

abstraction rates, given above. In our case, $r_{abs}/(r_{abs} + r_{ads}) \approx 0.057$. Thus, about 5.7% of the available C-H bonds will be vacant radical sites. This is a dynamic equilibrium state, as hydrogen atoms in the gas phase continually abstract hydrogen from C-H pairs to form radical sites, or fill radical sites to make C-H pairs, all on a very fast time scale relative to the time between CH_3 chemisorption events. The radical sites are continually redistributed randomly over the set of C-H bonds.

As the simulation evolves in time, some C-H pairs become unavailable as possible deposition sites by two possible mechanisms, steric shadowing or dendritic tree formation. As more CH_3 are chemisorbed to the initial surface some C-H pairs become inaccessible to hydrogen in the gas phase due to the steric presence of one or more nearby chemisorbed CH_3 molecules. This ‘shadowing’ effect must be taken into consideration. We consider a hydrogen or a radical site to be ‘unavailable’ due to shadowing if there is another carbon or hydrogen atom within 1.5 \AA in the direction perpendicular to the interface. Dendritic ‘tree’ formation occurs when a CH_3

chemisorbs to a radical site on a previously chemisorbed CH_3 which is connected to the surface by only one C-C bond. This process, which leads to the formation of alkane-like chains on the surface, is strongly suppressed by the high kinetic energy of the gas phase hydrogen atoms and (to a lesser extent) CH_3 molecules which impact the surface. In the simulation reported here, formation of such trees beyond a critical height of three C-C bonds is forbidden.

8.2 Diamond Simulation Method

The overall outline for the hybrid algorithm tailored to the specific model of methyl radical CVD contains eight steps in each iteration.

1. Randomly rearrange the chemisorbed hydrogen atoms and radical sites on the surface while maintaining the appropriate equilibrium distribution which is determined by the ratio of the hydrogen absorption to abstraction rates, ≈ 0.057 .
2. Scan possible event sites to determine available adsorption sites and calculate the total event rate R . The criteria for availability are, as stated above, that the radical site not be ‘shadowed’ from above by other atoms, and that deposition at the radical site will not produce a ‘tree’ larger than three C-C bonds.
3. Select a random propagation time Δt from the distribution given by Equation 7.11. This is accomplished by selection of a random number ξ from a uniform distribution on the interval (0,1) and taking $\Delta t = -\frac{1}{R} \ln(\xi)$ [81]. The total time of the simulation is the sum of propagation times for all steps.
4. Randomly choose an event site from the site list. This is accomplished by first producing another random number ξ , and then picking the lowest value of n

which satisfies the inequality

$$\sum_{i=1}^n r_i \geq \xi \quad (8.1)$$

Here r_i is the rate for the event which can occur at site i (this depends on the type of atom or radical site which might be located at site i). The sum runs over the site list, which is continually updated as sites are added by deposition and removed by shadowing or the formation of C-C bonds.

5. Perform the chosen event—attach a CH_3 radical to the n th adsorption site.
6. Perform off-lattice MMC rotation moves about the C-C bond between the newly chemisorbed CH_3 and the surface carbon to which bonding has occurred. This step allows the chemisorbed CH_3 to relax into an energetically more favorable state, if possible. If, after this relaxation, the energy of the chemisorbed CH_3 is still greater than a cutoff (set at 1.5 eV in the simulation reported here), the deposition move is rejected. Otherwise, the deposition move is accepted.
7. Equilibrate the area around each site by off-lattice MMC displacement moves with hydrogens removed. This is the “bond formation” step. After the MC moves, the bonding status of all affected carbons is updated. Two carbons are considered to be bonded if the distance between them is less than a bonding cutoff. The value used for this cutoff in the current simulations is 1.73 Å. The equilibrium C-C bond length in diamond is 1.54 Å.
8. Randomly reattach H atoms at 94.3% of the surface carbon sites. Relax the surface by considering random displacements of all surface adatoms, and random rotations about C-C bonds which support chemisorbed CH_3 . Off-lattice MMC displacements and rotations are employed along with simulated annealing. That is, a set of MMC rotations and translations of chemisorbed atoms and their neighbors are performed at a temperature of 2500 K, roughly twice the

experimental gas phase temperature. Upon completion of these moves, hydrogen atoms and radical sites are redistributed over the set of all dangling carbon bonds, maintaining the equilibrium ratio of 5.7% radical sites. Then another set of MMC moves are performed using a temperature of half the temperature used in the previous set of MC moves. The process is repeated N_{anneal} times using a temperature of $1/N_{\text{anneal}}$ of the original temperature in each successive step. This relaxation procedure works well, but it is not unique. Since the relaxation is very fast, any method can, in principle, be used to simulate the relaxation process so long as it converges toward an equilibrium state.

Surface relaxation is the most critical step for the formation of diamond-like carbon structures. It is at this point in the simulation that crystalline symmetry begins to appear in a continuum simulation. In large, off-lattice simulations such as the present example, the relaxation steps are also the most computationally intense part of the study.

Since the practical problem of computation time reduction in large simulations is central to this study, it is appropriate to mention some of the programming considerations that bear on this problem. The use of most many-body potentials requires the development of an efficient method for determining neighbors and next-nearest neighbors. The cell method (see Section 3.1.3, page 34) is more efficient than standard neighbor lists for simulations such as the present example which involves between 1000 to 4000 atoms. The use of the cell method provides an added advantage. Distortions to the diamond lattice due to local structural differences are quite localized [159]. Consequently, when an event takes place, surface relaxation moves need only be performed on the atoms in cells near the location of the event.

Since particles are added and deleted throughout the course of the simulation, linked lists [87] are used to store atom information. Actually, several lists are used.

Linked lists are employed to hold members of a particular cell, to hold the possible locations of event sites and to hold the total collection of atoms in the system. The C programming language is used to allow simple implementation of data structures and to provide pointers to reference these structures. Pointers permit ‘fluid’ movement of atoms among several categories without any repetition of atom information. That is, throughout the simulation, only one data structure is needed to hold all information for a particular atom. This programming mode is convenient, beneficial to debugging the code, and more efficient since movement of a data structure among linked lists involves changing only a few pointer variables rather than the entire data structure as would be necessary if traditional arrays were used to store information.

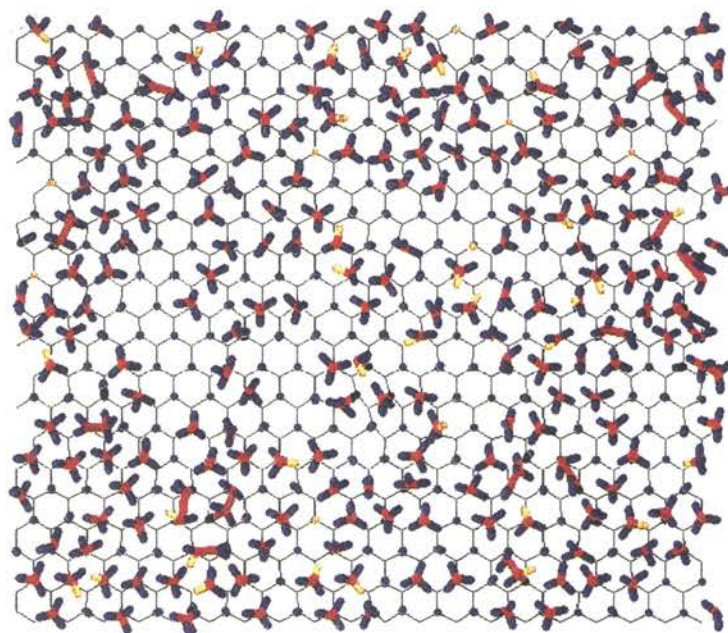
When determining the bonding of atoms in Step 7 of the algorithm, a method is required for dealing with hydrogen abstraction. During the period between CH_3 events, there will be a great deal of rearrangement of hydrogen atoms on the surface. This rearrangement will provide radical sites to which added structures can form chemical bonds. Given that each site experiences about 10^4 hydrogen desorption/adsorption events per CH_3 adsorption, added structures will have the opportunity to bond to any nearby carbon atom at multiple moments between CH_3 events. To simulate this situation, we simply remove all hydrogen atoms near added structures for one set of off-lattice MC moves, at the gas phase temperature (1250 K). This allows any carbons which are sufficiently close to bond. Bonds are updated after this set of moves, and hydrogens are added randomly to 94.3% of the sites. Subsequently, the simulated annealing relaxation moves are carried out. Finally, we have arbitrarily limited the size of tree-like structures on the surface. Such structures will be unstable during film deposition and will therefore tend to vanish during the extended time scales of the experiment.

Chapter 9

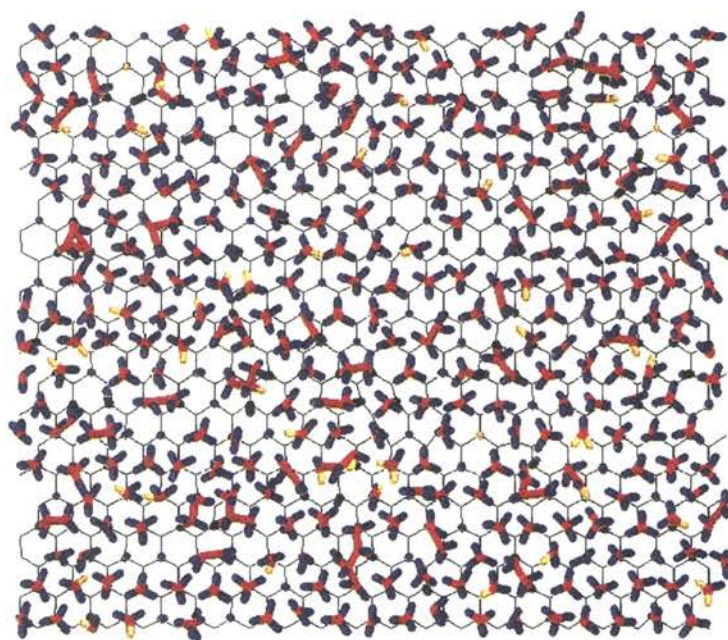
Results & Discussion

Figures 9.1–9.3 show the same surface as Figure 8.1 at various times during the simulation. In Figure 9.1(a) one can see the surface at $t = 1.288$ ms covered with CH_3 but with few bonds between chemisorbed methyls. Figure 9.1(b) shows the surface at $t = 3.278$ ms where pair bonding has begun on a large scale. Figure 9.2(a) shows the surface at $t = 8.959$ ms with hydrogens removed. This surface is shown at an oblique angle to enhance the visualization of the vertical growth and to note several desorbed molecules. One elongated, linear bonded chain is colored green for easy visualization. Figure 9.2(b) shows the surface at $t = 9.801$ ms, when smaller surface clusters are beginning to coalesce into larger structures. This configuration contains several ringed clusters, most notably the 5-membered ring at the upper left, shown in green. These rings tend to break up easily during relaxation, but some are precursors for diamond $\{111\}$ surface clusters. Figure 9.3 shows a snapshot of a portion of the surface at $t = 19.9$ ms. In this snapshot only substrate carbon and chemisorbed carbon which has become fully 4-coordinated (although not necessarily tetrahedral) are shown. In three locations (just below center at the left, just above center at the right, and near the bottom, left of center) are small nuclei of carbon atoms which are in nearly the correct diamond $\{111\}$ geometry.

Figure 9.4 is a plot showing counts of various types of clusters to depict surface morphology versus time which reflects the bonding behavior seen in Figures 9.1–9.3.

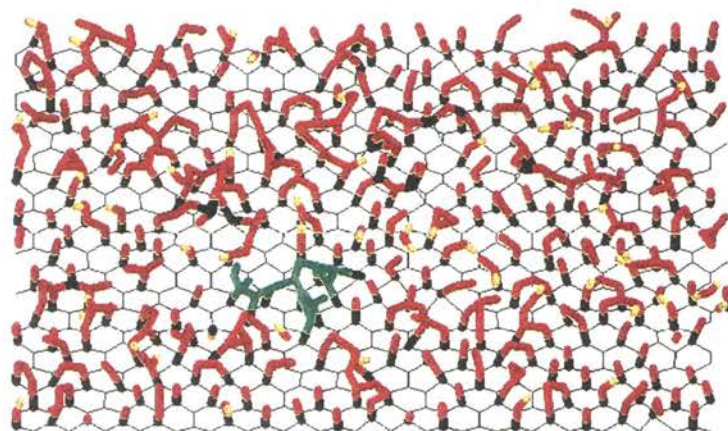


(a)

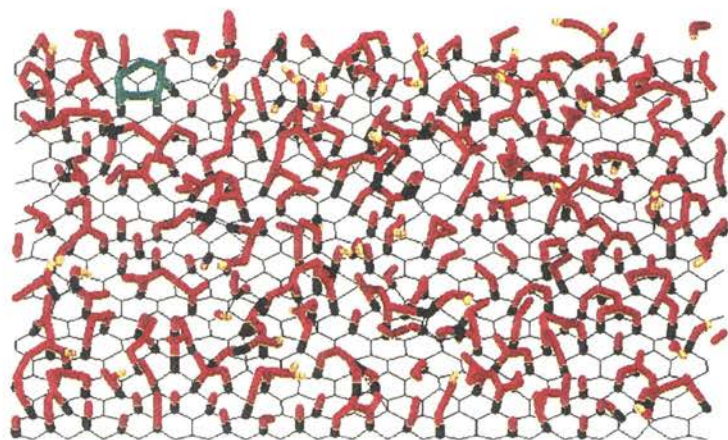


(b)

Figure 9.1: Two snapshots of the simulated diamond surface at times (a) $t = 1.288$ ms and (b) $t = 3.278$ ms. Blue atoms are H, black atoms are substrate C, red atoms are adsorbed C, and yellow 'atoms' indicate radical sites.



(a)



(b)

Figure 9.2: Two snapshots of the simulated diamond surface at times (a) $t = 8.959$ ms and (b) $t = 9.801$ ms. Hydrogens are not shown, black atoms are substrate C, red atoms are adsorbed C, and yellow 'atoms' indicate radical sites. The green atoms are C atoms highlighted to show the chains and rings forming on the surface.

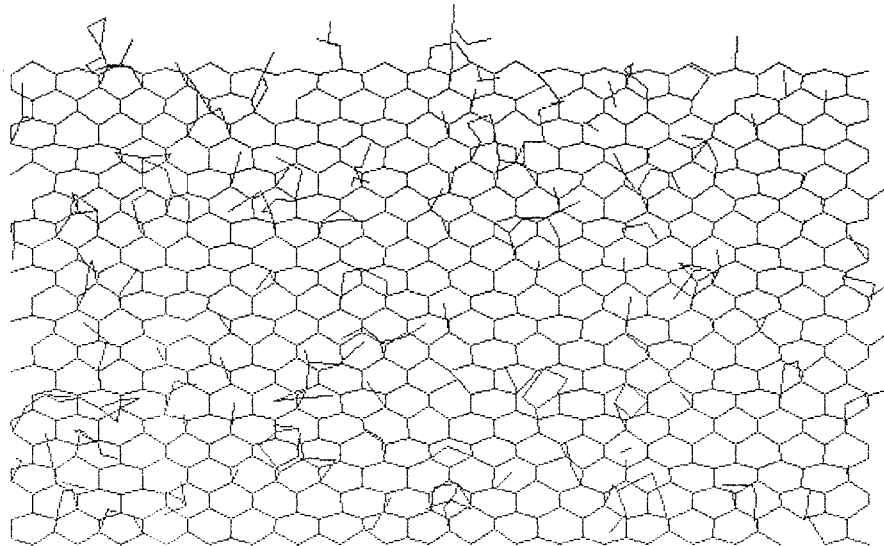


Figure 9.3: Surface at $t = 19.9$ ms. Only four-coordinated or substrate carbon is shown in this snapshot. Three distinct small clusters with partial diamond $\{111\}$ symmetry have formed.

After sufficient coverage of the bare surface is attained, pair bonds form rapidly. The earliest pair bonds are simple attachments between adjacent chemisorbed methyl radicals, with strained surface bonds which allow the methyls to approach close enough to bond. Later, 3-carbon ‘bridges’ form, in which a third carbon bridges the gap between two carbons chemisorbed to the original surface. These structures are required for the formation of a second diamond $\{111\}$ layer. After a longer time interval, the 3-carbon clusters and two-carbon clusters begin to link into larger, linear clusters. In many cases, parts of these larger clusters close off to form rings of 4–7 carbon atoms. In the time scale of this simulations, most rings were unstable, breaking up via desorption or surface diffusion shortly after formation.

The simulation procedure described in the previous chapter was tailored specifi-

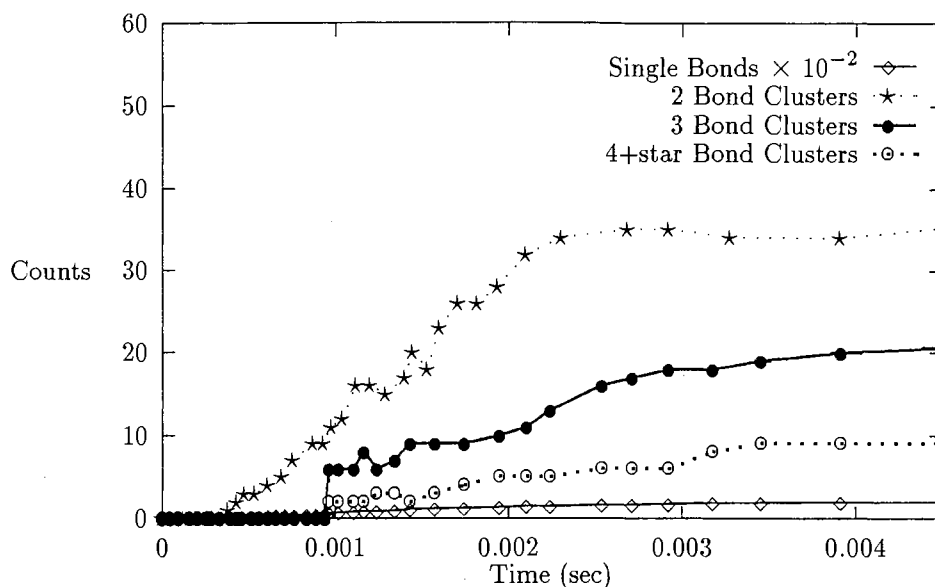


Figure 9.4: Plot of growth of surface clusters consisting of pairs, triplets and larger clusters of chemisorbed C-C bonds versus time.

cally to simulate CVD diamond film growth using the Brenner [148] potential energy function. Many previous trials were utilized to determine the most efficient method for carrying out the hybrid simulation method. The critical aspect of the simulation which controls the morphology of the growing surface is the surface equilibration procedure. The procedure used both allows for C-C bonds to form and for the surface to properly relax between bond formation and CH_3 chemisorption steps.

For further improvement of the quality and size of simulated films, more equilibration steps should be included, although this would slow the simulations considerably. Alternatively, new efficient methods to relax the surface could be developed. Probably the single most important computational problem which must be overcome for this method to produce crystalline film is relaxation. The relaxation of amorphous structures into systems with crystalline symmetry requires time scales which are too long to observe in all but the simplest of models. Final stages of relaxation may also involve complex many-particle cooperative moves which are beyond the scope of any current simulation methodology. This is especially true for carbon systems.

Carbon has a very rich potential energy surface as can be seen from the various stable structures that can form such as diamond, graphite, nanotubes, buckyballs, *etc.*. The competition between these structures makes any numerical method of relaxing carbon structures very difficult.

The results presented describe the evolution of surface morphology as a function of time for the first 20 ms of CVD diamond film growth. We have found that surface growth primarily consists of the formation of linear bonded chains, which may close off into rings for short time intervals. At this early stage of growth, stable ledges of tetrahedral carbon have only begun to form. It may be that a substantial overlayer must form over the substrate before large scale relaxation into a crystalline phase can begin. This should occur on a time scale of seconds since an experimental rate of $0.5 \mu\text{m}/\text{h}$ corresponds to about 1.4 \AA of vertical growth, or roughly one layer per second. Times required for the formation of a fraction of a layer have not yet been achieved. However, the times achieved in this study are very long compared to most off-lattice atomic resolution simulations of complex systems, which are commonly at most a few tens of nanoseconds.

In all simulations the calculated results are highly dependent on the model assumptions. One additional assumption not discussed above is the use of the phenomenological potential of Brenner [148]. This function has been extensively tested, and is highly parameterized to accurately reproduce the energetics of many carbon-hydrogen structures. Nevertheless its use in the formation of diamond film represents an extrapolation of the potential to the untested area of amorphous structures and their relaxation into crystalline potential wells.

Bibliography

- [1] D. Ritchie. *The Computer Pioneers*. Simon & Schuster, Inc., New York, 1986.
- [2] N. Metropolis, A. W. Rosenbluth, M. N. Rosenbluth, A. H. Teller, and E. Teller. Equation of state calculations by fast computing machines. *Journal of Chemical Physics*, 21(6):1087–1092, June 1953.
- [3] G. Ciccotti, D. Frenkel, and I. R. McDonald, editors. *Simulation of Liquids and Solids: Molecular Dynamics and Monte Carlo Methods in Statistical Mechanics*. North-Holland, Amsterdam, 1987.
- [4] S.-W. Chiu, M. Clark, V. Balaji, S. Subramaniam, H. L. Scott, and E. Jakobs-son. Incorporation of surface tension into molecular dynamics simulation of an interface: A fluid phase lipid bilayer membrane. *Biophysical Journal*, 69:1230–1245, October 1995.
- [5] M. M. Clark, L. M. Raff, and H. L. Scott. Kinetic Monte Carlo studies of early surface morphology in diamond film growth by chemical vapor deposition of methyl radical. *Physical Review B*, 54(18):5914–5919, 1996.
- [6] M. M. Clark, L. M. Raff, and H. L. Scott. A hybrid Monte Carlo method for off-lattice simulation of processes involving steps with widely varying rates. *Computers in Physics*, (in press), 1996.
- [7] R. B. Gennis. *Biomembranes: Molecular Structure and Function*. Springer Advanced Texts in Chemistry. Spinger-Verlag, New York, 1989.
- [8] S. J. Singer and G. L. Nicholson. The fluid mosaic model of the structure of cell membranes. *Science*, 175:720–731, 1972.
- [9] M. N. Jones and D. Chapman. *Micelles, Monolayers, and Biomembranes*. Wiley-Liss, New York, 1987.
- [10] G. Cevc and D. Marsh. *Phospholipid Bilayers*. John Wiley & Sons, New York, 1995.
- [11] J.-P. Ryckaert and A. Bellemans. Molecular dynamics of liquid *n*-butane near its boiling point. *Chemical Physics Letters*, 30(1):123–125, 1975.

- [12] J. Seelig. Deuterium magnetic resonance: Theory and application to lipid membranes. *Quarterly Reviews of Biophysics*, 10(3):353–418, 1977.
- [13] J. H. Davis. The description of membrane lipid conformation, order and dynamics by ^2H -NMR. *Biochimica et Biophysica Acta*, 737:117–171, 1983.
- [14] M. Bloom, E. Evans, and O. G. Mouritsen. Physical properties of the fluid lipid-bilayer component of cell membranes: A perspective. *Quarterly Reviews of Biophysics*, 24(3):293–397, 1991.
- [15] E. Oldfield, M. Meadows, D. Rice, and R. Jacobs. Spectroscopic studies of specifically deuterium labeled membrane systems. Nuclear magnetic resonance investigation of the effects of cholesterol in model systems. *Biochemistry*, 17(14):2727–2740, 1978.
- [16] J. J. de Vries and H. J. C. Berendsen. Nuclear magnetic resonance measurements on a macroscopically ordered smectic liquid crystalline phase. *Nature*, 221:1139–1140, 1969.
- [17] R. Mendelsohn and R. G. Snyder. Infrared spectroscopic determination of conformational disorder and microphase separation in phospholipid acyl chains. In K. M. Mertz, Jr. and B. Roux, editors, *Biological Membranes*, chapter 6, pages 145–174. Birkhäuser, Boston, 1996.
- [18] R. Mendelsohn, M. A. Davies, J. W. Brauner, H. F. Schuster, and R. A. Dluhy. Quantitative determination of conformational disorder in the acyl chains of phospholipid bilayers by infrared spectroscopy. *Biochemistry*, 28(22):8934–8939, 1989.
- [19] R. G. Snyder and M. W. Poore. Conformational structure of polyethylene chains from the infrared spectrum of the partially deuterated polymer. *Macromolecules*, 6(5):708–715, 1973.
- [20] R. Mendelsohn and L. Senak. Quantitative determination of conformational disorder in biological membranes by FTIR spectroscopy. In R. J. H. Clark and R. E. Hester, editors, *Biomolecular Spectroscopy: Part A*, volume 20 of *Advances in Spectroscopy*, chapter 8, pages 339–380. John Wiley & Sons, New York, 1993.
- [21] M. Maroncelli, H. L. Strauss, and R. G. Snyder. On the CD_2 probe infrared method for determining polymethylene chain conformation. *Journal of Physical Chemistry*, 89(20):4390–4395, 1985.
- [22] P. J. Flory. *Statistical Mechanics of Chain Molecules*. John Wiley & Sons, New York, 1969.

- [23] H. L. Casal and R. N. McElhaney. Quantitative determination of hydrocarbon chain conformational order in bilayers of saturated phosphatidylcholines of various chain lengths by Fourier transform infrared spectroscopy. *Biochemistry*, 29(23):5423–5427, 1990.
- [24] T. J. McIntosh. X-ray diffraction analysis of membrane lipids. In R. Brasseur, editor, *Molecular Description of Biological Membranes by Computer Aided Conformational Analysis*, volume I, chapter 1.B.1, pages 247–265. CRC Press, Inc., Boca Raton, 1990.
- [25] J. F. Nagle, R. Zhang, S. Tristram-Nagle, W. Sun, H. I. Petrache, and R. M. Suter. X-ray structure determination of fully hydrated L_α phase dipalmitoylphosphatidylcholine bilayers. *Biophysical Journal*, 70:1419–1431, 1996.
- [26] J. F. Nagle. Theory of the main lipid bilayer phase transition. *Annual Reviews of Physical Chemistry*, 31:157–195, 1980.
- [27] J. F. Nagle and H. L. Scott. Biomembrane phase transitions. *Physics Today*, 31(2):38–47, 1978.
- [28] A. Caillé, D. Pink, F. de Verteuil, and M. J. Zuckermann. Theoretical models for quasi-two-dimensional mesomorphic monolayers and membrane bilayers. *Canadian Journal of Physics*, 58(5):581–611, 1980.
- [29] H. L. Scott, Jr. Phase transitions in lipid bilayers: A theoretical model for phosphatidylethanolamine and phosphatidic acid bilayers. *Biochimica et Biophysica Acta*, 648:129–136, 1981.
- [30] J. F. Nagle. Theory of biomembrane phase transitions. *Journal of Chemical Physics*, 58(1):252–264, 1973.
- [31] S. Marčelja. Chain ordering in liquid crystals. I. Even-odd effect. *Journal of Chemical Physics*, 60(9):3599–3604, 1974.
- [32] S. Marčelja. Chain ordering in liquid crystals II. Structure of bilayer membranes. *Biochimica et Biophysica Acta*, 367:165–176, 1974.
- [33] H. L. Scott, Jr. Some models for lipid bilayer and biomembrane phase transitions. *Journal of Chemical Physics*, 62(4):1347–1353, 1975.
- [34] H. L. Scott, Jr. Phosphatidylcholine bilayers: A theoretical model which describes the main and the lower transitions. *Biochimica et Biophysica Acta*, 643:161–167, 1981.
- [35] H. L. Scott. Lipid-cholesterol interactions: Monte Carlo simulations and theory. *Biophysical Journal*, 59:445–455, 1991.
- [36] R. W. Pastor. Molecular dynamics and Monte Carlo simulations of lipid bilayers. *Current Opinion in Structural Biology*, 4:486–492, 1994.

- [37] K. V. Damodaran and K. M. Mertz, Jr. Computer simulation of lipid systems. In K. B. Lipkowitz and D. B. Boyd, editors, *Reviews in Computational Chemistry*, volume 5, chapter 5, pages 269–298. VCH Publishers, Inc., New York, 1994.
- [38] P. van der Ploeg and H. J. C. Berendsen. Molecular dynamics simulation of a bilayer membrane. *Journal of Chemical Physics*, 76(6):3271–3276, 1982.
- [39] P. van der Ploeg and H. J. C. Berendsen. Molecular dynamics of a bilayer membrane. *Molecular Physics*, 49(1):233–248, 1983.
- [40] E. Egberts and H. J. C. Berendsen. Molecular dynamics simulation of a smectic liquid crystal with atomic detail. *Journal of Chemical Physics*, 89(6):3718–3732, 1988.
- [41] M. L. Berkowitz and K. Raghavan. Computer simulation of a water/membrane interface. *Langmuir*, 7:1042–1044, 1991.
- [42] K. Raghavan, M. R. Reddy, and M. L. Berkowitz. A molecular dynamics study of the structure and dynamics of water between dilauroylphosphatidylethanolamine bilayers. *Langmuir*, 8:233–240, 1991.
- [43] H. De Loof, S. C. Harvey, J. P. Segrest, and R. W. Pastor. Mean field stochastic boundary molecular dynamics simulation of a phospholipid in a membrane. *Biochemistry*, 30:2099–2113, 1991.
- [44] K. V. Damodaran, K. M. Mertz, Jr., and B. P. Gaber. Structure and dynamics of the dilauroylphosphatidylethanolamine lipid bilayer. *Biochemistry*, 31:7656–7664, 1992.
- [45] H. Heller, M. Schaefer, and K. Schulten. Molecular dynamics simulation of a bilayer of 200 lipids in the gel and in the liquid-crystal phases. *Journal of Physical Chemistry*, 97:8343–8360, 1993.
- [46] S.-J. Marrink, M. Berkowitz, and H. J. C. Berendsen. Molecular dynamics simulation of a membrane/water interface: The ordering of water and its relation to the hydration force. *Langmuir*, 9:3122–3131, 1993.
- [47] T. R. Stouch. Lipid membrane structure and dynamics studied by all-atom molecular dynamics simulations of hydrated phospholipid bilayers. *Molecular Simulation*, 10:335–362, 1993.
- [48] R. M. Venable, Y. Zhang, B. J. Hardy, and R. W. Pastor. Molecular dynamics simulations of a lipid bilayer and of hexadecane: An investigation of membrane fluidity. *Science*, 262:223–226, 1993.
- [49] E. Egberts, S.-J. Marrink, and H. J. C. Berendsen. Molecular dynamics simulation of a phospholipid membrane. *European Biophysics Journal*, 22:423–436, 1994.

- [50] P. Huang, J. J. Perez, and G. H. Loew. Molecular dynamics simulations of phospholipid bilayers. *Journal of Biomolecular Structure & Dynamics*, 11(5):927–956, 1994.
- [51] A. J. Robinson, W. G. Richards, P. J. Thomas, and M. M. Hann. Head group and chain behavior in biological membranes: A molecular dynamics computer simulation. *Biophysical Journal*, 67:2345–2354, December 1994.
- [52] S. E. Feller, Y. Zhang, and R. W. Pastor. Computer simulation of liquid/liquid interfaces. II. Surface tension-area dependence of a bilayer and monolayer. *Journal of Chemical Physics*, 103(23):10267–10276, 1995.
- [53] W. Shinoda, T. Fukada, S. Okazaki, and I. Okada. Molecular dynamics simulation of the dipalmitoylphosphatidylcholine (DPPC) lipid bilayer in the fluid phase using the Nosé-Parrinello-Rahman NPT ensemble. *Chemical Physics Letters*, 232:308–322, January 13 1995.
- [54] K. Tu, D. J. Tobias, and M. L. Klein. Constant pressure and temperature molecular dynamics simulation of a fully hydrated liquid crystal phase dipalmitoylphosphatidylcholine bilayer. *Biophysical Journal*, 69:2558–2562, December 1995.
- [55] F. Zhou and K. Schulten. Molecular dynamics study of a membrane-water interface. *Journal of Physical Chemistry*, 99:2194–2207, 1995.
- [56] Y. Zhang, S. E. Feller, B. R. Brooks, and R. W. Pastor. Computer simulation of liquid/liquid interfaces. I. Theory and application to octane/water. *Journal of Chemical Physics*, 103:10252–10266, 1995.
- [57] J. F. Nagle. Area/lipid of bilayers from NMR. *Biophysical Journal*, 64:1476–1481, 1993.
- [58] S. G. Whittington and D. Chapman. Effect of density on configurational properties of long-chain molecules using a Monte Carlo method. *Transactions of the Faraday Society*, 62:3319–3324, 1966.
- [59] A. J. Kox, J. P. J. Michels, and F. W. Wiegel. Simulation of a lipid monolayer using molecular dynamics. *Nature (London)*, 287:317–319, 1980.
- [60] H. L. Scott. Monte Carlo studies of the hydrocarbon region of lipid bilayers. *Biochimica et Biophysica Acta*, 469:264–271, 1977.
- [61] H. L. Scott and S.-L. Cherng. Monte Carlo studies of phospholipid lamellae: Effects of proteins, cholesterol, bilayer curvature, and lateral mobility on order parameters. *Biochimica et Biophysica Acta*, 510:209–215, 1978.
- [62] B. Owenson and L. R. Pratt. Monte Carlo calculation of the molecular structure of surfactant bilayers. *Journal of Physical Chemistry*, 88:6048–6052, 1984.

- [63] J. Harris and S. A. Rice. A lattice model of a supported monolayer of amphiphile molecules: Monte Carlo simulations. *Journal of Chemical Physics*, 88(2):1289–1306, 1988.
- [64] H. L. Scott. Computer aided methods for the study of lipid chain packing in model biomembranes and micelles. In R. Brasseur, editor, *Molecular Description of Biological Membranes by Computer Aided Conformational Analysis*, volume I, chapter 1.A.3, pages 123–149. CRC Press, Inc., Boca Raton, 1990.
- [65] M. Milik, J. Skolnick, and A. Kolinski. Monte Carlo studies of an idealized model of a lipid-water system. *Journal of Physical Chemistry*, 96:4015–4022, 1992.
- [66] Y. K. Levine, A. Kolinski, and J. Skolnick. A lattice dynamics study of a langmuir monolayer of monounsaturated fatty acids. *Journal of Chemical Physics*, 98(9):7581–7587, 1993.
- [67] Y. K. Levine. Monte Carlo dynamics study of *cis* and *trans* unsaturated hydrocarbon chains. *Molecular Physics*, 78(3):619–623, 1993.
- [68] T. Taga and K. Masuda. Monte Carlo study of lipid membranes: Simulation of diparmitoylphosphatidylcholine [*sic*] bilayers in gel and liquid-crystalline phases. *Journal of Computational Chemistry*, 16(2):235–242, 1995.
- [69] H. L. Scott. Monte Carlo calculations of order parameter profiles in models of lipid-protein interactions in bilayers. *Biochemistry*, 25:6122–6126, 1986.
- [70] J. Xing and H. L. Scott. Monte Carlo studies of a model for lipid-gramicidin A bilayers. *Biochemical and Biophysical Research Communications*, 165(1):1–6, 1989.
- [71] J. Xing and H. L. Scott. Monte Carlo studies of a model for lipid-gramicidin A bilayers. *Biochimica et Biophysica Acta*, 1106:227–232, 1992.
- [72] H. Larry Scott. Statistical mechanics and Monte Carlo studies of lipid membranes. In K. M. Mertz, Jr. and B. Roux, editors, *Biological Membranes*, chapter 3, pages 83–104. Birkhäuser, Boston, 1996.
- [73] J. I. Siepmann and D. Frenkel. Configurational bias Monte Carlo: A new sampling scheme for flexible chains. *Molecular Physics*, 75(1):59–70, 1992.
- [74] J. I. Siepmann. A method for the direct calculaton of chemical potentials for dense chain systems. *Molecular Physics*, 70(6):1145–1158, 1990.
- [75] D. Frenkel, G. C. A. M. Mooij, and B. Smit. Novel scheme to study structural and thermal properties of continuously deformable molecules. *Journal of Physics: Condensed Matter*, 4:3053–3076, 1992.

- [76] D. Frenkel. Advanced Monte Carlo techniques. In M. P. Allen and D. J. Tildesley, editors, *Computer Simulation in Chemical Physics*, volume 397 of *NATO ASI Series C: Mathematical and Physical Sciences*, chapter 4, pages 93–152. Kluwer Academic Publishers, Dordrecht, 1993.
- [77] K. Esselink, P. A. J. Hilbers, S. Karaborni, J. I. Siepmann, and B. Smit. Simulating complex fluids. *Molecular Simulation*, 14:259–274, 1995.
- [78] B. Smit and J. I. Siepmann. Simulating the adsorption of alkanes in zeolites. *Science*, 264:1118–1120, 1994.
- [79] B. Smit. Molecular simulations of fluid phase equilibria. *Fluid Phase Equilibria*, 116:249–256, 1996.
- [80] M. W. Deem and J. S. Bader. A configurational bias Monte Carlo method of linear and cyclic peptides. *Molecular Physics*, 87(6):1245–1260, 1996.
- [81] M. P. Allen and D. J. Tildesley. *Computer Simulation of Liquids*. Oxford University Press, New York, 1987.
- [82] R. W. Pastor. Determination of chain conformations in the membrane interior by brownian dynamics simulations. In R. Brasseur, editor, *Molecular Description of Biological Membranes by Computer Aided Conformational Analysis*, volume I, chapter 1.A.3, pages 171–201. CRC Press, Inc., Boca Raton, 1990.
- [83] R. W. Pastor. Techniques and applications of Langevin dynamics simulations. In G. R. Luckhurst and C. A. Veracini, editors, *The Molecular Dynamics of Liquid Crystals*, chapter 5, pages 85–138. Kluwer Academic Publishers, Dordrecht, 1994.
- [84] D. C. Rapaport. *The Art of Molecular Dynamics Simulation*. Cambridge University Press, Cambridge, 1995.
- [85] L. Verlet. Computer “experiments” on classical fluids. I. Thermodynamical properties of Lennard-Jones molecules. *Physical Review*, 159(1):98–103, 1967.
- [86] D. J. Tildesley. The molecular dynamics method. In M. P. Allen and D. J. Tildesley, editors, *Computer Simulation in Chemical Physics*, volume 397 of *NATO ASI Series C: Mathematical and Physical Sciences*, chapter 2, pages 23–47. Kluwer Academic Publishers, Dordrecht, 1993.
- [87] S. Oualline. *Practical C Programming*. O’Reilly & Associates, Inc., Sebastopol, 1993.
- [88] H. Goldstein. *Classical Mechanics*. Addison-Wesley Publishing Company, Reading, 2nd edition, 1980.

- [89] J.-P. Ryckaert, G. Ciccotti, and H. J. C. Berendsen. Numerical integration of the cartesian equations of motion of a system with constraints: Molecular dynamics of n -alkanes. *Journal of Computational Physics*, 23:327–341, 1977.
- [90] H. J. C. Berendsen, J. P. M. Postma, W. F. van Gunsteren, A. DiNola, and J. R. Haak. Molecular dynamics with coupling to an external bath. *Journal of Chemical Physics*, 81(8):3684–3690, 1984.
- [91] E. Jakobsson, S. Subramaniam, and H. L. Scott. Strategic issues in molecular dynamics simulations of membranes. In K. M. Mertz, Jr. and B. Roux, editors, *Biological Membranes*, chapter 4, pages 105–123. Birkhäuser, Boston, 1996.
- [92] S. H. White. Small phospholipid vesicles: Internal pressure, surface tension, and surface free energy. *Proceedings of the National Academy of Sciences of the United States of America*, 77(7):4048–4050, 1980.
- [93] S. E. Feller and R. W. Pastor. On simulating lipid bilayers with an applied surface tension: Periodic boundary conditions and undulations. *Biophysical Journal*, (in press), 1996.
- [94] W. F. van Gunsteren and H. J. C. Berendsen. *Groningen Molecular Simulation (GROMOS) Library Manual*. Biomos, Groningen, 1987.
- [95] H. Hauser, I. Pascher, R. H. Pearson, and S. Sundell. Preferred conformation and molecular packing of phosphatidylethanolamine and phosphatidylcholine. *Biochimica et Biophysica Acta*, 650:21–51, 1981.
- [96] H. J. C. Berendsen, J. R. Grigera, and T. P. Straatsma. The missing term in effective pair potentials. *Journal of Physical Chemistry*, 91:6269–6271, 1987.
- [97] E. Egberts. *Molecular Dynamics Simulations of Multibilayer Membranes*. PhD thesis, University of Groningen, Groningen, The Netherlands, 1988.
- [98] S. W. Dodd. *Deuterium Nuclear Magnetic Resonance Studies of Saturated Phospholipid Bilayers*. PhD thesis, University of Virginia, August 1987.
- [99] J. T. Woodward, IV and J. A. Zasadzinski. Amplitude, wave form, and temperature dependence of bilayer ripples in the $P_{\beta'}$ phase. *Physical Review E*, 53(4):R3044–R3047, 1996.
- [100] D. C. Wack and W. W. Webb. Measurements of modulated lamellar $P_{\beta'}$ phases of interacting lipid membranes. *Physical Review Letters*, 61(10):1210–1213, 1988.
- [101] D. C. Wack and W. W. Webb. Synchrotron x-ray study of the modulated lamellar phase $P_{\beta'}$ in the lecithin-water system. *Physical Review A*, 40(5):2712–2730, 1989.

- [102] S.-J. Sun, S. Tristram-Nagle, R. M. Suter, and J. F. Nagle. Structure of the ripple phase in lecithin bilayers. *Proceedings of the National Academy of Sciences of the United States of America*, 93:7008–7012, 1996.
- [103] J. A. N. Zasadzinski, J. Schneir, J. Gurley, V. Elings, and P. K. Hansma. Scanning tunneling microscopy of freeze-fracture replicas of biomembranes. *Science*, 239:1013–1015, 1988.
- [104] H. L. Scott and W. S. McCullough. Theories of the modulated ‘ripple’ phase of lipid bilayers. *International Journal of Modern Physics B*, 5:2479–2497, 1991.
- [105] L. D. Landau and E. M. Lifshitz. *Statistical Physics*, volume 5 of *Landau and Lifshitz Course of Theoretical Physics*, chapter XIV. Pergamon Press, Oxford, 3rd edition, 1980.
- [106] P. A. Pearce and H. L. Scott, Jr. Statistical mechanics of the ripple phase in lipid bilayers. *Journal of Chemical Physics*, 77(2):951–958, 1982.
- [107] H. L. Scott. The ripple phase in lipid bilayers: Theory and computer simulation. *Comments in Molecular Cellular Biophysics*, 2(3 & 4):197–217, 1984.
- [108] H. L. Scott and P. A. Pearce. Calculation of intermolecular interaction strengths in the $P_{\beta'}$ phase. *Biophysical Journal*, 55:339–345, 1989.
- [109] H. L. Scott and W. S. McCullough. Lipid-cholesterol interactions in the $P_{\beta'}$ phase: Application of a statistical mechanical model. *Biophysical Journal*, 64:1398–1404, 1993.
- [110] W. Scott McCullough, J. H. H. Perk, and H. L. Scott. Analysis of a model for the ripple phase of lipid bilayers. *Journal of Chemical Physics*, 93(8):6070–6080, 1990.
- [111] M. N. Rosenbluth and A. W. Rosenbluth. Monte Carlo calculation of the average extension of molecular chains. *Journal of Chemical Physics*, 23(2):356–359, 1955.
- [112] K. Binder, editor. *Monte Carlo Methods in Statistical Physics*, volume 7 of *Topics in Current Physics*. Springer-Verlag, New York, 2nd edition, 1986.
- [113] K. Binder and D. W. Heermann. *Monte Carlo Simulation in Statistical Physics: An Introduction*, volume 80 of *Springer Series in Solid-State Sciences*. Springer-Verlag, Berlin, 2nd edition, 1992.
- [114] H. C. Kang and W. H. Weinberg. Dynamic Monte Carlo with a proper energy barrier: Surface diffusion and two-dimensional domain ordering. *Journal of Chemical Physics*, 90(5):2824–2830, March 1989.
- [115] K. A. Fichtorn and W. H. Weinberg. Theoretical foundations of dynamical Monte Carlo simulations. *Journal of Chemical Physics*, 95(2):1090–1096, July 1991.

- [116] J. G. Amar and F. Family. Critical cluster size: Island morphology and size distribution in submonolayer epitaxial growth. *Physical Review Letters*, 74(11):2066–2069, 1995.
- [117] E. J. Dawnkaski, D. Strivastava, and B. J. Garrison. Growth of diamond films on a diamond{001}(2×1):H surface by time dependent Monte Carlo simulations. *Journal of Chemical Physics*, 104(15):5997–6008, 1995.
- [118] M. E. Tuckerman, G. J. Martyna, and B. J. Berne. Molecular dynamics algorithm for condensed systems with multiple time scales. *Journal of Chemical Physics*, 93(2):1287–1291, 1990.
- [119] K. Kawasaki. Diffusion constants near the critical point for time-dependent Ising models. I. *Physical Review*, 145:224, 1966.
- [120] K. Kawasaki. Diffusion constants near the critical point for time-dependent Ising models. II. *Physical Review*, 148:375, 1966.
- [121] K. Kawasaki. Diffusion constants near the critical point for time-dependent Ising models. III. Self-diffusion constant. *Physical Review*, 150:285, 1966.
- [122] K. Binder, editor. *Applications of the Monte Carlo Method in Statistical Physics*, volume 36 of *Topics in Current Physics*. Springer-Verlag, New York, 2nd edition, 1987.
- [123] R. J. Larsen and M. L. Marx. *An Introduction to Mathematical Statistics and Its Applications*. Prentice Hall, Englewood Cliffs, New Jersey, 2nd edition, 1986.
- [124] R. C. DeVries. Synthesis of diamond under metastable conditions. *Annual Review of Materials Science*, 17:161–187, 1987.
- [125] J. C. Angus and C. C. Hayman. Low-pressure, metastable growth of diamond and “diamondlike” phases. *Science*, 241:913, 1988.
- [126] F. G. Celii and J. E. Butler. Diamond chemical vapor deposition. *Annual Review of Physical Chemistry*, 42:643, 1991.
- [127] W. A. Yarbrough, M. A. Stewart, and J. A. Cooper, Jr. Combustion synthesis of diamond. *Surface Coatings and Technology*, 39/40:241–252, 1989.
- [128] K. E. Spear. Diamond—ceramic coating of the future. *Journal of the American Ceramic Society*, 72(2):171–191, 1989.
- [129] R. Messier, A. R. Badzian, T. Badzian, K. E. Spear, P. Bachmann, and R. Roy. From diamond-like carbon to diamond coatings. *Thin Solid Films*, 153:1–9, 1987.
- [130] Y. Tzeng, E. Cutshaw, R. Phillips, T. Srinigunon, A. Ibrahim, and B. H. Loo. Growth of diamond films on silicon from an oxygen-acetylene flame. *Applied Physics Letters*, 56:134, 1990.

- [131] S. S. Lee, D. W. Minsek, D. J. Vestyck, and P. Chen. Growth of diamond from atomic hydrogen and a supersonic free jet of methyl radicals. *Science*, 263:1596–1598, 1994.
- [132] M. Pruski, D. P. Lang, and Son-Jong Hwang. Structure of thin diamond films: A ^1H and ^{13}C nuclear-magnetic-resonance study. *Physical Review B*, 49(15):10635–10642, 1994.
- [133] M. Fanciulli and T. D. Moustakas. Defects in diamond thin films. *Physical Review B*, 48(20):14982–14988, 1993.
- [134] J. C. Angus, M. Sunkara, S. R. Sahaida, and J. T. Glass. Twinning and faceting in early stages of diamond growth by chemical vapor deposition. *Journal of Materials Research*, 7(11):3001–3009, 1992.
- [135] M. P. Everson and M. A. Tamor. Studies of nucleation and growth morphology of boron-doped diamond microcrystals by scanning tunneling microscopy. *The Journal of Vacuum Science and Technology*, A9:1570–1576, 1991.
- [136] V. Baranauskas, M. Fukui, C. R. Rodrigues, N. Parizotto, and V. J. Tarava-Airoldi. Direct observation of chemical vapor deposited diamond films by atomic force microscopy. *Applied Physics Letters*, 60(13):1567–1569, 1992.
- [137] D. Huang, M. Frenklach, and M. Maroncelli. Energetics of acetylene-addition mechanism of diamond growth. *Journal of Physical Chemistry*, 92:6379–6381, 1988.
- [138] M. Frenklach and K. E. Spear. Growth mechanism of vapor-deposited diamond. *Journal of Materials Research*, 3(1):133–140, 1988.
- [139] X. Y. Zhu and J. M. White. Interaction of ethylene and acetylene with Ni(111): A SSIMS study. *Surface Science*, 214:240–256, 1989.
- [140] M. Tsuda, M. Nakajima, and S. Oikawa. Epitaxial growth mechanism of diamond crystal in $\text{CH}_4\text{-N}_2$ plasma. *Journal of the American Chemical Society*, 108:5780–5783, 1986.
- [141] M. Tsuda, M. Nakajima, and S. Oikawa. The importance of the positively charged surface for the epitaxial growth of diamonds at low pressure. *Japanese Journal of Applied Physics*, 26(5):L527–L529, 1987.
- [142] S. J. Harris and D. N. Belton. Thermochemical kinetics of a proposed mechanism for diamond growth from acetylene. *Japanese Journal of Applied Physics*, 30(10):2615–2618, 1991.
- [143] M. Frenklach. Monte Carlo simulation of diamond growth by methyl and acetylene reactions. *Journal of Chemical Physics*, 97(8):5794–5802, 1992.

- [144] S. J. Harris. Mechanism for diamond growth from methyl radicals. *Applied Physics Letters*, 56(23):2298–2300, 1991.
- [145] D. G. Goodwin. Simulations of high-rate diamond syntheses: Methyl as growth species. *Applied Physics Letters*, 59:277, 1991.
- [146] S. J. Harris and A. M. Weiner. Diamond growth rates vs. acetylene concentrations. *Thin Solid Films*, 212:201–205, 1991.
- [147] S. J. Harris and D. G. Goodwin. Growth on the reconstructed diamond (100) surface. *Journal of Physical Chemistry*, 97:23–28, 1993.
- [148] D. W. Brenner. Empirical potential for hydrocarbons for use in simulating the chemical vapor deposition of diamond films. *Physical Review B*, 42(15):9458, November 1990.
- [149] J. Tersoff. Empirical interatomic potential for carbon, with applications to amorphous carbon. *Physical Review Letters*, 61(25):2879, 1988.
- [150] R. C. Mowrey, D. W. Brenner, and B. I. Dunlap. Simulations of C₆₀ collisions with a hydrogen-terminated diamond {111} surface. *Journal of Physical Chemistry*, 95:7138–7142, 1991.
- [151] D. W. Brenner and J. A. Harrison. Atomistic simulations of diamond film. *American Ceramic Society Bulletin*, 71(12):1821–1828, December 1992.
- [152] J. A. Harrison and D. W. Brenner. Simulated tribochemistry: An atomic-scale view of the wear of diamond. *Journal of the American Chemical Society*, 116:10399–10402, 1994.
- [153] B. J. Garrison, E. J. Dawnkaski, D. Srivastava, and D. W. Brenner. Molecular dynamics simulations of dimer opening on a diamond{001}(2×1) surface. *Science*, 255:835–838, 1992.
- [154] J. Peploski, D. L. Thompson, and L. M. Raff. Molecular dynamics studies of elementary surface reactions of C₂H₂ and C₂H in low-pressure diamond-film formation. *Journal of Physical Chemistry*, 96:8538, 1992.
- [155] X. Y. Chang, D. L. Thompson, and L. M. Raff. Minimum-energy paths for elementary reactions in low-pressure diamond-film formation. *Journal of Physical Chemistry*, 97:10112, 1993.
- [156] J. Xing and H. L. Scott. Diamond film growth by chemical vapor deposition: A molecular simulation. *Physical Review B*, 48:4806–4810, 1993.
- [157] X. Y. Chang, M. Perry, J. Peploski, D. L. Thompson, and L. M. Raff. Theoretical studies of hydrogen-abstraction reactions from diamond and diamond-like surfaces. *Journal of Chemical Physics*, 99(6):4748, 1993.

- [158] M. Perry and L. M. Raff. Theoretical studies of elementary chemisorption reactions on an activated diamond ledge surface. *Journal of Physical Chemistry*, 98:4375, 1994.
- [159] M. Page and D. W. Brenner. Hydrogen abstraction from a diamond surface. Ab initio quantum chemical study with constrained isobutane as a model. *Journal of the American Chemical Society.*, 113:3270–3274, 1991.

2

VITA

Michael Mohr Clark

Candidate for the Degree of

Doctor of Philosophy

Thesis: COMPUTATIONAL STUDIES OF COMPLEX SYSTEMS IN CONDENSED MATTER PHYSICS

Major Field: Physics

Biographical:

Personal Data: Born in Conway, Arkansas, on February 8, 1968, the son of Robert L. Clark and Mary Sue Clark.

Education: Received Bachelor of Arts degree in Physics from Hendrix College, Conway, Arkansas in June 1990. Completed the requirements for the Doctor of Philosophy degree in Physics at Oklahoma State University in December 1996.

Professional Experience: Undergraduate researcher at the Oak Ridge National Laboratory and at Oklahoma State University Department of Physics during the Summers of 1988 and 1989, respectively; Teaching Assistant from August 1990 to May 1994; Research Assistant from May 1994 to the present.

Professional Memberships: American Physical Society, Biophysical Society.